ROLE OF SILICA IN THE SELF-ASSEMBLY OF SALT-SURFACTANT MESOPHASES AND SYNTHESIS OF MESOPOROUS METAL OXIDES

A THESIS SUBMITTED TO
THE GRADUATE SCHOOL OF ENGINEERING AND SCIENCE
OF BILKENT UNIVERSITY
IN PARTIAL FULFILLMENT OF THE REQUIREMENTS FOR
THE DEGREE OF
MASTER OF SCIENCE
IN CHEMISTRY

By
Najeeb Ullah
July 2023

ROLE OF SILICA IN THE SELF-ASSEMBLY OF
SALT-SURFACTANT MESOPHASES AND SYNTHESIS
OF MESOPOROUS METAL OXIDES

By Najeeb Ullah
July 2023

We certify that we have read this thesis and that in our opinion it is fully adequate, in scope and in quality, as a thesis for the degree of Master of Science.

Ömer Dağ (Advisor)

Emre Büküşoğlu

Halil İbrahim Okur

Approved for the Graduate School of Engineering and Science:

Orhan Arıkan

Director of the Graduate School

ABSTRACT

Role of Silica in the Self-Assembly of Salt-Surfactant Mesophases and Synthesis of Mesoporous Metal Oxides

Najeeb Ullah

M.Sc. in Chemistry

Advisor: Ömer Dağ

July, 2023

In recent years, mesoporous metal oxides have attracted great attraction due to their unique optical, electrochemical, and catalytic properties. Mesoporous nickel oxide (m-NiO) is a p-type semiconductor, versatile in its application due to its high surface area, and has been investigated towards electrochromic devices, electrodes, supercapacitors, and catalysts. The electrochemical properties of NiO depend on its morphology, surface area, and particle size. In this thesis, mesoporous nickel oxide has been synthesized by combining soft templating (molten salt-assisted self-assembly method) and hard templating methods to attain a high surface area. Homogeneous aqueous solutions of nickel(II) nitrate hexahydrate ($[Ni(H_2O)_6](NO_3)_2$), TMOS (as silica source), and two surfactants, CTAB (charged surfactant) and $C_{12}E_{10}$ (nonionic surfactant) are stable only if a concentrated nitric acid is added before the TMOS addition. In the absence of nitric acid, TMOS hydrolyzes and condenses quickly, resulting in silica precipitation. The silica precipitation also occurs by using other salts, such as nickel(II) chloride hexahydrate, nickel(II) sulfate hexahydrate, cobalt(II) nitrate hexahydrate, and manganese(II) nitrate tetrahydrate. The silica precipitate is characterized by ATR-FTIR, small-angle, and wide-angle XRD and N_2 adsorption-desorption measurements. The diffraction lines at 1.7 and 23°, 2θ, indicate the formation of mesostructured amorphous silica, in which the surfactant species fill the

pores. . The silica precipitate is calcined at 450 ^{o}C for two hours to remove the surfactant completely, and characterized by ATR-FTIR, small-angle and wide-angle XRD measurements, N_2- adsorption-desorption analysis and SEM-EDX techniques. The maximum surface area (1395 m^2/g) is obtained from the cobalt(II) nitrate hexahydrate salt, and the EDX analysis confirms that there is no element other than silicon and oxygen in its elemental detection limit.

The homogeneous, stable aqueous solutions of the nickel(II) nitrate hexahydrate ($[Ni(H_2O)_6](NO_3)_2$), HNO_3, TMOS (as silica source), and two surfactants, CTAB (charged surfactant) and $C_{12}E_{10}$ (nonionic surfactant) solution is drop-casted on a glass slide to form a mesophase and analyzed by small-angle XRD, ATR-FTIR and POM techniques. The diffraction lines at 1.5 and 1.6^{o}, 2θ, show the formation of ordered lyotropic liquid crystalline mesophases. The mesophases are then calcined at different temperatures (from 250 to 500 °C), to obtain m-NiO/SiO_2 powders and characterized by ATR-FTIR, XRD measurements, N_2- adsorption-desorption analysis, and SEM-EDX techniques. The XRD patterns show broad lines at small- and wide-angles, indicating the formation of m-NiO/SiO_2 at 300 °C, where the pore-walls are made up 2.6 nm crystalline NiO coated amorphous silica . The NiO particle size (on the pore wall) grows with increasing annealing temperature, and at 500 °C, the particle size reaches 7.9 nm. This is also supported by the BET surface area that decreases at higher temperatures. At 300 °C, the BET surface area is 305 m^2/g, which drops to 174 m^2/g at 500 °C. However, the pore size of m-NiO/SiO_2 does not responds to annealing temperature. It means that the pore walls grow in 2D space rather than 3D due to the presence of silica as a hard template. Therefore, combining the hard- and soft-templating methods can efficiently synthesize the crystalline materials with a high surface area.

The m-NiO/SiO_2 films can be coated over the FTO glass and calcined at different temperatures to fabricate the electrodes for oxygen evolution reaction (OER). During CV measurement, the NiO pore-walls get oxidized to NiOOH and reduced to $Ni(OH)_2$ in the back cycle. Moreover, overpotential that is determined for the OER improves with the usage of the electrode, independent of the electrode thickness.

Keywords: hard template, soft template, molten salt-assisted self-assembly, lyotropic liquid crystal, mesoporous nickel oxide, mesoporous silica

Özet

Tuz-Yüzey Aktif Arafazlarının Kendiliğinden Oluşumunda Silika'nın Rolü ve Mezogözenekli Metal Oksitlerin Sentezi

Najeeb Ullah

Kimya, Yüksek Lisans

Tez Danışmanı: Ömer Dağ

Temmuz, 2023

Son yıllarda, mezogözenekli metal oksitler benzersiz optik, elektrokimyasal ve katalitik özellikleri nedeniyle büyük ilgi çekmektedir. Mezogözenekli nikel oksit (m-NiO), yüksek yüzey alanına sahip olması ve p-tipi bir yarı iletken olması nedeniyle uygulama alanları çok yönlüdür. Bu nedenle, mezogözenekli nikel oksit elektrokromik cihaz, elektrot, süperkapasitör ve katalizör alanları için yoğun çalışılmıştır. Nikel oksitin elektrokimyasal özellikleri morfolojisine, yüzey alanına ve partikül boyutuna bağlıdır. Bu tezde, yüksek yüzey alanına ulaşmak için yumuşak kalıplama (eriyik tuz yardımlı kendiliğinden oluşma yöntemi) ve sert kalıplama yöntemleri birlikte kullanılarak mezogözenekli nikel oksit ince filmleri sentezlenmiştir. Homojen sulu çözeltilerde nikel(II) nitrat hekzahidrat ($[Ni(H_2O)_6](NO_3)_2$), TMOS (tetrametilortosilikat, silika kaynağı) ve iki yüzey aktif madde CTAB (yüklü yüzey aktif madde) ve $C_{12}E_{10}$ (iyonik olmayan yüzey aktif madde) çözeltileri, yalnızca TMOS eklenmeden önce nitrik asit eklenirse karalıdır. Nitrik asit olmadığında, TMOS hızla hidrolize olup polimerleşerek, silika olarak çöker. Silika ayrıca nikel(II) klorür hekzahidrat, nikel(II) sülfat hekzahidrat, kobalt(II) nitrat hekzahidrat ve mangan(II) nitrat tetrahidrat gibi diğer tuzlar kullanılarak da oluşur. Bu silika çökeltileri çözeltiden ayrıldıktan sonra ATR-FTIR, küçük-açı ve geniş-açı XRD ve N_2 adsorpsiyon-desorpsiyon ölçümleri ile karakterize edilmiştir. 1.7 ve 23° derecedeki difraksiyon kırınımları, numunin mesoyapılı ve yüzeyaktif bölümler arasında yer alan amorf silika olduğunugöstermektedir. Silika çökeltileri 2 saat boyunca 450 °C'de kalsine edilerek

yüzey aktif madde tamamen uzaklaştırılmış ve oluşan malzeme ATR-FTIR, küçük-açı ve geniş-açı XRD ölçümleri, N_2 adsorpsiyon-desorpsiyon analizi ve SEM-EDX ile karakterize edilmiştir. Maksimum yüzey alanı (1395 m^2/g) kobalt(II) nitrat hekzahidrat tuzu ile elde edilmiştir ve EDX analizi, elementel analizinde silikon ve oksijenden başka bir element olmadığını doğrulanmıştır.

Nikel(II) nitrat hekzahidrat ($[Ni(H_2O)_6](NO_3)_2$), HNO_3, TMOS ve iki yüzey aktif madde (CTAB ve$C_{12}E_{10}$) homojen kararlı sulu çözeltileri, arafazları oluşturmak amacı ile, cam bir alttaş üzerine damlatılarak küçük-açı XRD, ATR-FTIR ve POM teknikleri ile analiz edilmiştir. 1.5 ve 1.6 derecedeki difraksiyon kırınımları düzenli liyotropik sıvı kristal arafazların oluşumunu gösterir. Bu arafazlar daha sonra farklı sıcaklıklarda (250 ila 500 ^oC) kalsine edilmiş ve elde edilen mezogözenekli NiO/SiO_2 tozları ATR-FTIR, XRD, N_2 adsorpsiyon-desorpsiyon ve SEM-EDX teknikleri ile karakterize edilmiştir. 300 °C'de yakılan malzemelerden elde edilen XRD desenleri, mezogözenekli 2.6 nm kristalin NiO kaplı silika (m-NiO/SiO_2) ince filmlerin oluşumunu gösterir. Gözenek duvarlarında kaplı nickel oksit parçacık boyutu, sıcaklık arttıkça büyür ve 500 °C'de parçacık boyutu yaklaşık 7.9 nm olur. XRD verisi, yüksek sıcaklıklarda azalan BET yüzey alanı analizi tarafından da desteklenmektedir. 300 °C'de BET yüzey alanı 305 m^2/g iken, 500 °C'de bu değer 174 m^2/g'ye düşer. Bununla birlikte, m-NiO/SiO_2'nin gözenek boyutu değişmez, bu da gözenek duvarlarının silika sert şablonun varlığından dolayı üç boyutlu alanda değil, iki boyutlu alanda büyüdüğünü gösterir. Dolayısıyla, sert ve yumuşak kalıplama yöntemlerinin birleştirilmesi yöntemi, yüksek yüzey alanına sahip kristalin malzemelerin sentezinde verimli bir şekilde kullanılabilir.

m-NiO/SiO_2 filmleri FTO alttaş üzerine kaplanıp farklı sıcaklıklarda kalsine edilerek elektrokimyasal oksijen üretme tepkimesi (OER) için elektrotlar üretildi. Döngüsel voltametri sırasında, m-NiO/SiO_2 gözenek duvarı NiOOH'a oksitlenir ve geri dönğüde ise $Ni(OH)_2$'ye indirgenir. Ayrıca, bu elektrotların OER overpotansiyel ölçümleri, zamanla ve kullandıkça azaldığı ve elektrot kalınlığına bağlı olmadığı belirlendi.

Anahtar kelimeler: sert kalıplama, yumuşak kalıplama, eriyik tuz yardımlı kendiliğinden oluşma yöntemi, liyotropik sıvı kristal, mezogözenekli nikel oksit, mezogözenekli silika.

Acknowledgment

I would like to extend my sincere gratitude to my outstanding supervisor, Ömer Dağ, for his helpful advice, constant support, and exceptional mentorship throughout this research endeavor. This thesis and my overall academic development greatly benefited from his experience, critical analysis, and dedication. I consider myself fortunate to have had the chance to work for him.

My profound gratitude goes out to my lab mates, Işil Ulu, Assel Amirzhanova, Irmak Karakaya, and Hamid Ali Raza, whose contributions, teamwork, and friendship have enhanced my research experience. Işil and Assel have been a great help throughout this journey. Whenever I needed them, they were available. My understanding of the subject has significantly increased due to their knowledge exchange, stimulating conversations, and cooperative efforts. I am also thankful to our undergraduate senior year students, Arda, Gözde, Pamir and Muratcan, I appreciate the lively atmosphere they fostered in our study group.

I would want to express my sincere gratitude to my close friends, Badar Munir, Rashid Mahmood and Sobia Farooq, whose unflagging support, inspiration, and understanding have been a source of strength during this trip. I've maintained a healthy work-life balance thanks to your company and wonderful support. You've also given me the much-needed break I needed when things were tough.

I must thank my parents for their consistent encouragement and faith in my academic goals. My accomplishments have been built on the support, love, and sacrifices of my family. They gave me advice and instilled in me the virtues of tenacity and grit, and I will always be grateful for that. I don’t think ever in my life I’ll be able to pay back them.

Table of Contents

List of Figures

List of Tables

Abbreviations:

LC: Liquid Crystal

LLC: Lyotropic Liquid Crystal

LLCM: Lyotropic Liquid Crystalline Mesophases

TLC: Thermotropic Liquid Crystal

MASA: Molten Salt-Assisted Self-Assembly

EISA: Evaporation Induced Self-Assembly

CMC: Critical Micelle Concentration

CTAB: Cetyltrimethylammonium Bromide

TMOS: Tetramethyl Orthosilicate

SDS: Sodium Dodecyl Sulphate

XRD: X-Ray Diffraction

POM: Polarized Optical Microscopy

SEM: Scanning Electron Microscopy

EDX: Energy Dispersive X-Ray Spectroscopy

ATR-FTIR: Attenuated Total Reflection Fourier- Transform Infrared

BET: Brunauer, Emmett and Teller

BJH: Barrett-Joyner-Halenda

FWHM: Full Width Half Maximum

FTO: Fluorine Doped Tin Oxide

CV: Cyclic Voltammetry

NHE: Normal Hydrogen Electrode

CP: Chronopotentiometry

RE: Reference Electrode

WE: Working Electrode

CE: Counter Electrode

Chapter 1

1. Introduction

During the past couple of decades, scientists have devoted great attention to synthesizing new inorganic materials for various applications. The fact that most of the chemical reactions involving charge transfer occur on the surface of solid materials, leads them to bring innovation and improvement in the methods used for the synthesis of such materials. Therefore, materials with a high surface area are of extreme importance for such applications. One main approach to attain high surface area is to make porous materials. These porous materials, based on their pore size, are categorized as microporous ($\leq$ 2nm), mesoporous (2-50 nm), and macroporous materials ($\geq$ 50nm)[1].

Zeolites are typical examples of microporous materials that consist of a tetrahedral crystalline framework of SiO_4 and AlO_4^- units, also known as aluminosilicates[2], [3].. This crystalline framework is built by repeating tetrahedra, which forms a complex network ensuring uniform cavities with small channels connecting each other[4], [5]..

These cavities in zeolites are the active sites for chemical reactions. Although zeolites are useful for many applications like catalysis[6], gas-separating membranes[7], etc., they also have some limitations[8]. One of these limitations is their inaccessible pores for large molecules. Additionally, the resulting products during the catalytic applications can obstruct zeolites' pores, further reducing their competence for such activities. Therefore, there was a need to synthesize the materials with larger pores to get rid of these problems.

1.1. Mesoporous Materials and Metal Oxides

Mesoporous materials with a pore size between 2 nm and 50 nm have proved to be ideal materials for achieving large surface area and eliminating the limitations of microporous materials[9], [10]. In 1992, the synthesis of mesoporous solids was first reported by Kresge et al. by calcining the aluminosilicate gels using a surfactant[11], [12]. They successfully proposed the liquid crystal templating approach for synthesizing mesoporous materials, where inorganic micelle walls were formed by silica materials. Also, Beck et al. proposed the mechanistic formation of the M41S family in detail where they designated MCM-41 as a hexagonal phase with a uniform channels and pore distribution with a high surface area of more than 700 m^2/g[11], [13]. They also proposed that the MCM-41 can be prepared with controlled pore size distribution ranging from 15 Å to greater than 100 Å depending on the chain length of the cationic surfactant used in the synthesis[13]. Over the last three decades, a lot of work has been devoted in these materials' synthesis, characterization, and mechanistic studies[12].

Furthermore, in 1995, Bagshaw et al. proposed another method for the synthesis of spherical and hexagonal mesoporous silica using block copolymers as templating agents and tetraethylorthosilicate (TEOS) as silica source[14], [15]. However, mesoporous silica has limited applications due to its chemical inertness and amorphous pore walls[16], [17]. Also, the synthesis of mesoporous non-siliceous materials is difficult due to the uncontrolled fast hydrolysis & condensation reactions of metal alkoxide precursors. It was observed that rapid crystallization occurs at high-temperature calcination, which results in collapsing pores of the material[18]. As a result, the synthetic methods of the

mesoporous silica materials are modified to synthesize non-silica mesoporous materials[19].

In 1998, Yang et al. reported the use of the soft templating method for the synthesis of mesoporous metal oxides and mixed metal oxides, such as Al_2O_3, Nb_2O_5, Ta_2O_5, SnO_2, Al_2TiO_5, ZrW_2O_8, and $SiTiO_4$ etc.[20]. The inorganic salts have been used as metal precursors and poly (alkylene oxide) block-copolymers as the soft templates in a non-aqueous medium[21].

Moreover, Guo et al. reported another method for the synthesis of mesoporous metal oxides by thermal decomposition of transition metal oxalates. They reported a successful synthesis method for various mesoporous metal oxides, such as $CoFe_2O_4$, $NiFe_2O_4$, Co_3O_4, and NiO etc.[22]. They also claimed that calcination temperature is an important factor for determining the final mesoporous structure of the materials. This method is more beneficial as it is more cost effective, versatile, and environmentally friendly. However, this method has a major limitation as production of non-uniform porous materials[22].

Transition metal oxides have gained a lot of attention among all the non-siliceous materials due to their emerging applications. In the following chapters, two main methods for the synthesis of ordered mesoporous materials using surfactant templates will be discussed in detail[18].

1.1.1. Synthesis of mesoporous metal oxides using soft templates

The soft templating approach was first used by Kresge et al. to synthesize mesoporous silica[11]. This approach is effectively used in the synthesis of mesoporous metal oxides as well[23]. However, one of the major limitations of this approach is the instability of the structure of materials during calcination. In the soft templating method, amphiphilic molecules known as surfactants are used as templates. These molecules have polar as well as non-polar ends, which arrange themselves into micelles by interacting with the solvent (polar or non-polar) used[21], [22], [24]. The first mesoporous transitional metal that involves sol-gel chemistry in its synthesis is titanium dioxide. $Ti(OC_3H_7)_4$ (hydrolyzed in

the presence of $C_5H_8O_2$) and phosphate-surfactants were used[19], [25], [26] in the assembly process and later categorized as a ligand-assisted method and has been successfully employed in the synthesis of mesoporous metal oxides[25], [26].

Later Brinker et al. introduced another method soft-templating method for synthesis of mesoporous metal oxides named as evaporation-induced self-assembly (EISA) method[27]. The mechanism EISA method involves certain steps: (i) preparation of a solution of inorganic salt precursor, surfactant (amphiphilic template), and the solvent simultaneously, (ii) evaporation of solvent after coating the material on the substrate, (iii) hydrolysis and condensation of precursors, and (iv) template removal upon calcination[28]. The concentration of micelles is an important factor in the preparation of ordered material using this method. Shape of the micelle is the factor of micelle concentration. Above a critical concentration (known as critical micelle concentration, CMC), micelles form different shapes such as spheres and cylinders. Moreover, after the solvent evaporation (by spin-coating, dip-coating, drop-casting, or spray-coating), the micelles form hexagonal, cubic or lamellar mesophases or mesostructures[27] . One specific type of mesophase can be obtained by adjusting the concentration of metal salt and non-ionic surfactant[29], [30]. A large range of mesoporous metal oxides was synthesized through the EISA method by using block-copolymer templates[20], [21].

However, the EISA method is also limited due to high reactivity of some precursors, such as uncontrolled rate of condensation. This leads to a formation of non-porous material. Slow hydrolysis and condensation of most of the transition metal salts also renders the use of the EISA method. Moreover, the surface area of the materials fabricated by using this method is not sufficient for many applications[31], [32].

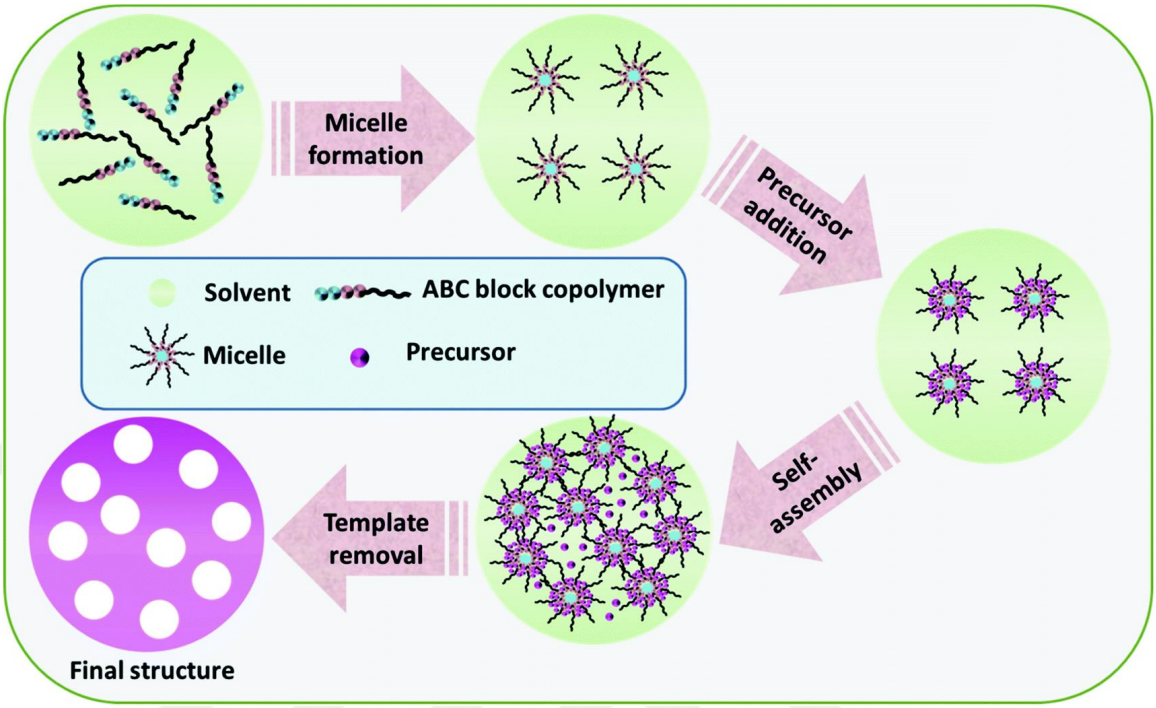

Figure 1.1. General schematic representation of soft templating method.

1.1.2. Synthesis of mesoporous metal oxides by hard templates

Hard-templating method also called the nano-casting method, has also been employed to synthesize a wide range of mesoporous materials[33], [34]. Where the soft-templating method involves the use of surfactant molecules for controlling the morphology of ordered mesoporous materials, the hard-templating method involves the use of a mesoporous material as a template for controlling the morphology of the target material. This method can be illustrated in 4 steps; (i) synthesis of a hard template (usually mesoporous silica or carbon), (ii) infiltration of the metal precursors into the porous template, (iii) heat treatment of the precursors for transforming into a product, (iv) removal of the template by chemical etching or calcination. The hard-templating method is favored over the soft-templating method as it allows to fabricate ordered materials that cannot be fabricated by the other method[18], [35], [36].

A schematic representation of the hard-templating method is illustrated in Figure.1.2[37].

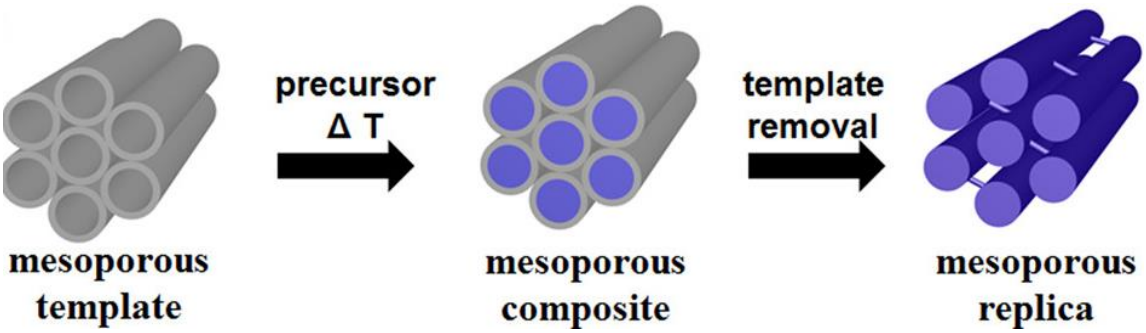

Figure 1.2. Schematic of hard-templating method to produce porous materials.

The first hard template employed in the synthesis of mesoporous material was a porous Al_2O_3 that was synthesized by an anodic oxidation method[38]. The synthesis of nanotubes, nanowires, and nanorods of metals by this template results in the synthesis of nanomaterials as well[38]. In 1999, Ryoo et al. for the first time synthesized mesoporous carbon, CMK-1 with a uniform pore size distribution by using a mesoporous silica hard template[35], [39]. For the removal of the silica template, the material was dispersed into concentrated NaOH or hydrofluoric acid solutions[19]. The synthesized material is stabilized by the presence of disordered pores in the hard template, which are interconnected the synthesized material through these channels[39], [40].

Later, Che et al. reported the synthesis of mesoporous carbon, CMK-5, by using the mesoporous silica template[41]. They also reported the synthesis of the first mesoporous transition metal oxide, Cr_2O_3, by using mesoporous silica template (SBA-15), which is produced using large surfactants such as pluronics[42]. Potassium dichromate was used as a precursor and the hard template was removed by washing with the HF solution[43]. They also employed the same method to synthesize the single-crystal 3-dimensional WO_3 with a hexagonal morphology. It was observed that the morphology of the resulting material is in relation to the pore size of the template and precursor size[44].

Li et al, in 2004, introduced a new hard template, carbon aerogel, for the synthesis of mesoporous metal oxides. They synthesized mesoporous MgO by using a suitable metal precursor. The resulting 3-dimensional porous MgO had a spherical morphology with a

surface area of approximately 150 m^2/g. The template was removed by heat-treating the material at 600 ^oC[42]. This method was extensively used for synthesizing a large range of mesoporous metal oxides[45], [46]. Mesoporous tin (IV) oxide nanowires with a surface area of 160 m^2/g, for lithium-ion batteries, were also synthesized by using different hard templates (KIT-6, a member of mesoporous silica family with cylindrical pores and SBA-15, also a member of mesoporous silica family with hexagonal pores)[47]. A highly ordered mesoporous Co_3O_4 was also fabricated by the aforementioned method[45]. Subsequently, the method became widespread and opened up many opportunities for the fabrication of other mesoporous metal oxides by using the hard template[48].

A new class of mesoporous materials having a chiral porous structure was introduced by Shopsowitz et al. using a lyotropic liquid crystalline phase of a nanocrystalline cellulose. The silica surrounds the nanocrystalline cellulose in a chiral arrangement, which on the removal of the cellulose template was used to synthesize titania. However, by playing with the chiral composites, the porosity of porous silica can be changed, which later defines the porosity of the mesoporous metal oxide[49].

The hard templating method allows controlling the structure of mesoporous materials as it involves the use of hard templates like silica. These templates are robust and on treatment at high temperatures retain their porous structure resulting in a high surface area product. However, this method also has some limitations as it involves the use of NaOH or HF solutions for the removal of the template. These species are reactive toward some of the transition metal oxides and may cause contaminations. Moreover, the high-temperature treatment can also be disadvantageous as silica might incorporate into the crystal structure of transition metal oxides. It also has a high cost as it involves multiple steps for the synthesis[50]. Therefore, a new approach to synthesizing the mesoporous transition metal oxides was needed[40].

1.2. Lyotropic Liquid Crystalline Mesophases

Liquid crystals (LC)-a fascinating class of materials that exhibit the properties of both the liquid as well as solid phases. A schematic of liquid crystals in comparison to solids and liquids is shown in Figure.1.3. LC phase is able to flow like liquids but maintains some degree of orientational order like solids[51]. The two different forms of liquid crystals are known; (i) thermotropic liquid crystals (TLC) and (ii) lyotropic liquid crystals (LLC)[52]. Thermotropic liquid crystals are usually display temperature dependent mesophases and their transition between liquid and solid can be initiated by varying the temperature[53].

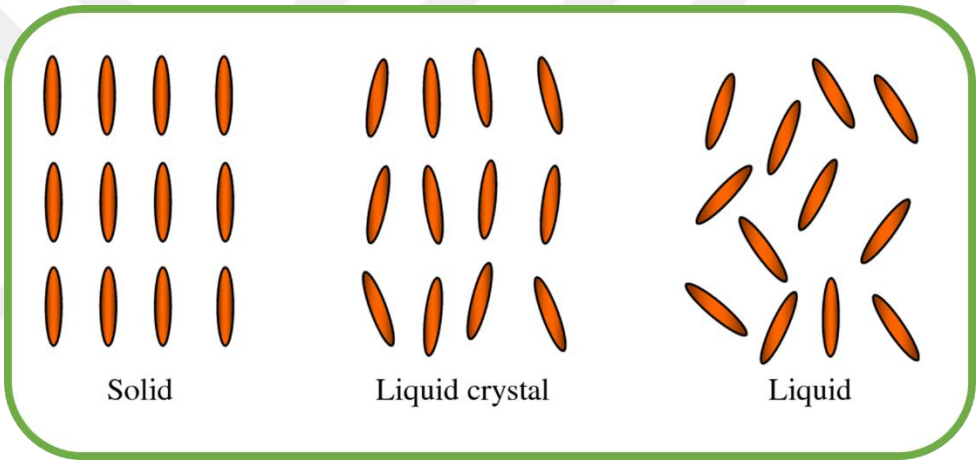

Figure 1.3. A schematic comparison of liquid crystal with liquid and solid.

Lyotropic liquid crystals mesophases usually exist in the form of mixtures. Their formation depends on specific amphiphilic molecules, classified as surfactants and a solvent. The surfactant molecules have two different ends; one hydrophobic and the other hydrophilic[54]. These molecules undergo self-assembly in the presence of a solvent to form micelles (core-shell structure). Depending on the polarity of the solvent, different arrangements of micelles may exist. The concentration of micelles and the solvent are critical factors in the formation of LLC mesophases[55]. On reaching a critical micelle concentration (CMC), these surfactant molecules aggregate together to form micelles that at higher concentration assemble into different types of mesophases. However, below critical micelle concentration, these molecules generally exist in solution as solvated and

distinct molecules. The structure of LLCs is highly affected by the surfactant concentration and temperature[56]. Moreover, a variation in the composition of LLC mesophases can impact the morphology of the resulting material. Such as various mesoporous materials like rod-shaped silica and hollow-titania were fabricated by using the solution-phase micelles as well as mesophases[57]–[59].

The materials with different mesophase structures (two-dimensional (2D) hexagonal, lamellar, three-dimensional cubic, etc.) can be synthesized by using LLC medium as it enables easy control over the morphology of resulting materials. The different mesophase structures are shown in Figure.1.4.

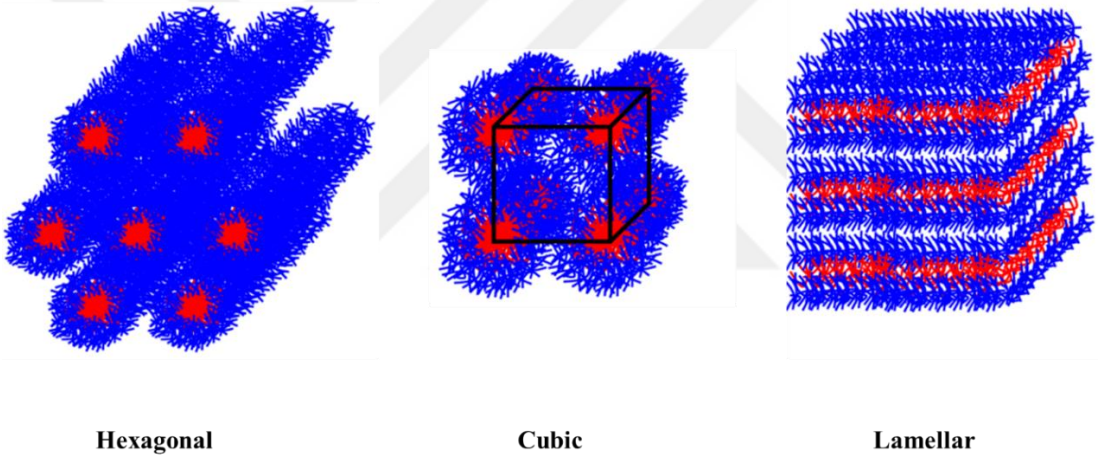

Figure 1.4. A schematic representation of hexagonal, cubic and lamellar mesophases.

These different mesophase structures can be detected by polarized optical microscopy (POM) imaging. The hexagonal mesophase exhibits a fan texture under POM, because it is a birefringent anisotropic phase with two different refractive indices. However, the cubic mesophase due to its isotropic nature can't be detected under POM. Moreover, the formation of these mesophases can also be characterized by the XRD technique. These mesophases diffract at small angles (usually 1-5°, 2θ) as the unit cells are much larger with larger d-spacings. The diffraction patterns can be analyzed by using Bragg's law as given by equation 1.1.

$$n\lambda = 2dSin\theta \quad \text{(Eq. 1.1.)}$$

Where θ is half of the measured angle, d is the spacing (in Å), λ is the wavelength of x-rays (1.5405 Å), and n is an integer.

The LLC templating method was first introduced by Attard *et al.* in 1995 for the synthesis of the mesoporous silica by using TMOS as a silica source and octaethylene glycol mono-dodecyl ether ($C_{12}EO_8$) as a template[15]. This was the first instance, where the LLC mesostructure was solidified and later this method was named as the true liquid crystalline templating (TLCT) process[15]. They also introduced a high surfactant ratio in this method whereas, previously a low surfactant ratio was used in the synthesis of M41S. Later in 1997, they employed the TLCT process to synthesize the mesoporous metals and other metal sulfides[60]–[64].

LLC templating method involves the use of a low concentration of transition metal salt and a surplus amount of water, which restricts the fabrication of materials by this method as a low concentration of salt is present in LLC mesophase.

In 2001, Dag et al. introduced a novel lyotropic liquid crystal mesophase that allows the high salt concentration in the presence of oligo ethylene oxides (C_nEO_m) nonionic surfactant[65]. They discovered that by using the different mole ratios of transition metal salts like $[Ni(H_2O)_6](NO_3)_2$, $[Co(H_2O)_6](NO_3)_2$, and $[Zn(H_2O)_6](NO_3)_2$ and nonionic surfactant, the LLC mesophases can be formed. Latter, they demonstrated that the transition metal salts exist in their molten state in LLC mesophase[65]. The different nonionic surfactants have been used to form the transition metal salt LLC mesophases[66]. Effect of counter-ion of transition metal salt precursor have been studied and reported that anions have important roles in the mesophase formation[67]. They claimed that the presence of different transition metal salt with different anions in the system affects the solubility of surfactants in aqueous medium[68] and also their extend of water capture is critical for the mesophase formation and stability[66], [69].

However, in the presence of only non-ionic surfactant LLC mesophases have limited salt uptake in the mesophase domains. Therefore, a charged surfactant, cethyltrimethyl ammonium bromide (CTAB) or sodium dodecylsulphoxide (SDS), was utilized to

overcome this limitation[70]. The new two-surfactant system, a nonionic and an ionic, ensures a high concentration of salts in the LLC mesophases. The mesophase can be stabilized by playing with the concentration of charged surfactant. By using zinc nitrate hexahydrate salt and the two-surfactant system, they loaded up to 8 salt/surfactant mole ratio into a lyotropic liquid crystalline mesophase (LLCM)[71]. Moreover, they synthesized mesoporous zinc oxide-silica as well as cadmium oxide-silica thin films by using the new LLCMs, where salt remains in the molten state. They introduced this method by name of the molten salt-assisted self-assembly (MASA) method[72].

1.3. Molten salt-Assisted Self-Assembly (MASA) Method

The MASA method was introduced by the Dag group in 2012 for the fabrication of mesoporous materials. This method involves the use of transition metal salts as inorganic metal precursors, two solvents (salt in its molten phase and water), and two surfactants (a nonionic and an ionic surfactant). In this assembly process, the salt behaves as a solvent upon melting in a constricted nano-spaces, the salt species are confined in the micelle domains and behaves as a solvent and hence helps in stimulating the self-assembly of surfactants and other precursors into LLC mesophases[73]. The melting point of the salt reduces in the constricted nano-space, this happens in accordance with the soft confinement effect (SCE)[73]. Therefore, this effect inhibits the crystallization of salt even in the presence of its high concentrations. Moreover, due to the nano-spaces, the seed formation for crystal growth is inhibited, which also makes the LLC mesophases stable.

The MASA technique has been used to synthesize a range of mesoporous metal-titanates such as $Li_4Ti_5O_{12}$, $MnTiO_3$, $CoTiO_3$, $CdTiO_3$, Zn_2TiO_4, etc.[74]. In this synthesis, titanium (IV) butoxide was used as a titanium source. It hydrolyses and condenses within the LLC mesophase at low temperatures and later forms the mesopores on calcination[75], [76]. The mesoporous $LiCoO_2$ and $LiMn_2O_4$ were also synthesized through the MASA method[77]. For this synthesis, the method was modified by replacing the charged surfactant, CTAB with CTAN (cetyltrimethylammonium nitrate) as with CTAB some metal bromide impurities were observed[77]. This modification prevents the formation of low surface area species during the process and produces mesoporous bimetallic oxides.

However, in the formation of mesoporous nickel oxide, these impurities were not observed. Therefore, CTAB can be used for the synthesis of mesoporous NiO material[78].

The MASA method is advantageous for the synthesis of mesoporous metal oxides over the EISA method. In the EISA method, during the evaporation process, the precursors are converted into mesostructured material straightaway. Therefore, the method is limited to the precursors that can undergo hydrolysis and condensation during the evaporation process. However, the MASA method can be used for the synthesis of other metal oxides as well. The MASA method was later extended for the synthesis of metal lithiates[77], [79], metal cobaltites[80], and many other mesoporous metal oxides. In this work, we will discuss the synthesis of mesoporous SiO_2-NiO thin films from 10-lauryl ether-CTAB-$[Ni(H_2O)_6](NO_3)_2$ and the effect of silica in this synthesis.

1.4. Mesoporous Nickel Oxide – Synthesis and Applications

In recent years, there has been a growing interest in mesoporous metal oxides because of their unique optical, catalytic, and electrochemical properties. These materials find various applications in fields such as supercapacitors, electrochromic devices, gas sensors, batteries, and more[81], [82]. Nickel oxide, a p-type semiconductor, is versatile in its application due to its high surface area and can be utilized as an electrochromic device, electrode, supercapacitor, and catalyst depending on the synthesis method employed[83], [84]. As previously stated, the MASA method was used in this thesis study to produce mesoporous nickel oxide. However, NiO thin films can also be synthesized by some other methods. One of the most commonly used techniques is the sol-gel method. NiO nanoparticles with spherical morphology were fabricated by utilizing a solution of nickel nitrate hexahydrate as the precursor[85]. The sol-gel method yielded nickel oxide with a surface area of 322 m^2/g[86]. A wet-chemical method can also be used in synthesizing the NiO nanoparticles by using $[Ni(H_2O)_6]Cl_2$ and a precipitating agent – NaOH[87]. This method results in the formation of NiO-nanosheet with a thickness of 2 nm, resulting in a remarkably high surface area of 377 m^2/g[86]. The hydrothermal approach can also be utilized in the synthesis of NiO particles with varying morphologies, including nanorods,

nanosheets, and spherical nanoparticles[88], [89]. The morphology of NiO can be controlled by varying the temperature and pressure during the process[90]. Mehr et al. also prepare porous nickel oxide particles with spherical morphology by using the microwave heating method. This method was faster and more efficient in comparison to other methods stated[91].

In summary, the morphology of NiO can be varied by using different synthetic methods and resulting NiO particles hence have varying properties for various applications. For supercapacitor applications, the dielectric surface depends on the surface area of the material, and NiO due to its good surface area can be used for this application[92]. The particle size of nickel oxide also influences its electrical as well as optical properties[93], [94]. The band gap of nickel oxide is dependent on calcination temperature and generally, can be reduced by the elevation in the calcination temperature[95].

Here, in this thesis, we combine and take advantage of both soft (MASA) and hard templating methods to fabricate electrodes with high surface area. Therefore, it is an extension of a previous work that used a high silica concentration to produce metal oxide coated mesoporous silica [75]. Here, we test the limitations of the silica uptake of the salt-surfactant mesophase to produce highly porous materials. This work can be further expanded to produce other transition metal oxide coated silica thin films for various purposes.

Chapter 2

2. Experimental Part

2.1. Chemicals

In this study, the solutions were prepared by using nickel nitrate hexahydrate ($[Ni(H_2O)_6](NO_3)_2$) as the metal salt precursor in an aqueous solvent. The two surfactants were used, cetyltrimethylammonium bromide ($[(C_{16}H_{33})N(CH_3)_3]Br$, also known as CTAB) as charged surfactant to assist the high concentration of salt and as structure directing agent with another nonionic surfactant 10 lauryl ether ($CH_3(CH_2)_{11}(OCH_2CH_2)_{10}OH$, represented as $C_{12}E_{10}$). Tetramethyl orthosilicate ($Si(OCH_3)_4$, represented as TMOS) and concentrated nitric acid (65%) were also used in the synthesis. All the chemicals were purchased from Sigma-Aldrich and used without any further purification.

2.2. Preparation of Ni(II) Solutions

The different solutions were prepared with respect to varying metal-to-surfactant mole ratios (from 2 to 10 ($[Ni(H_2O)_6](NO_3)_2$)/$C_{12}E_{10}$ mole ratio) and TMOS to surfactant mole ratios (from 2 to 6 ($Si(OCH_3)_4$/$C_{12}E_{10}$ mole ratio). The amounts of CTAB and $C_{12}E_{10}$ were kept constant (1:1 in all the solutions) by only changing the $[Ni(H_2O)_6](NO_3)_2$/$C_{12}E_{10}$ and ($Si(OCH_3)_4$/$C_{12}E_{10}$ mole ratios. All the compositions of the solutions are given in Table 2.1.

All the solutions were prepared in 20 mL vials. The solutions were typically prepared by first dissolving the metal salt precursor in 5 mL water along with CTAB and stirring on a magnetic stirrer for 15 minutes. Then, 0.500 g of non-ionic surfactant ($C_{12}E_{10}$) was added to obtain a clear solution and stirred for another 15 minutes. A few drops of concentrated nitric acid were added then followed by the addition of the desired concentration of TMOS as a silica source. All the sample compositions are represented as Ni-*n*-S-*x*, where *n* is the salt/$C_{12}E_{10}$ ratio, *x* is the TMOS/ $C_{12}E_{10}$ ratio and S represents silica.

Sample	$[Ni(H_2O)_6](NO_3)_2$ (g)	TMOS (g)	Conc.HNO_3 (drop)	CTAB (g)	$C_{12}E_{10}$ (g)	Water (g)
Ni-6-S-0.1	1.392	0.012	3	0.291	0.500	5
Ni-6-S-0.2	1.392	0.024	3	0.291	0.500	5
Ni-6-S-0.6	1.392	0.072	3	0.291	0.500	5
Ni-6-S-0.7	1.392	0.084	3	0.291	0.500	5
Ni-6-S-0.8	1.392	0.096	3	0.291	0.500	5
Ni-6-S-1	1.392	0.12	3	0.291	0.500	5
Ni-6-S-2	1.392	0.24	3	0.291	0.500	5
Ni-6-S-4	1.392	0.48	3	0.291	0.500	5
Ni-6-S-6	1.392	0.72	3	0.291	0.500	5
Ni-10-S-3	2.29	0.36	3	0.291	0.500	5
Ni-10-S-4	2.29	0.48	3	0.291	0.500	5

Table 2. 1. Compositions of all the aqueous solutions of $[Ni(H_2O)_6](NO_3)_2$-$C_{12}E_{10}$-CTAB– TMOS.

2.3. Preparation of Mesoporous NiO Films

NiO films were prepared by coating the above-freshly prepared clear homogenous solutions on glass slides either by spin coating or drop-casting followed by calcination. In both methods, the thickness of the film differs as spin coating produces thin films and drop-casting produces thicker films. The thickness of the film can further be adjusted by playing with the spinning rate of the spin coater instrument. However, all the samples were spin-coated at 2000 rpm for 10 seconds in which the solvent immediately evaporates resulting in gelation. In drop-casting, a few drops of the clear solution were spread on the glass slide and then kept at room temperature for 4-5 minutes to evaporate the solvent. In the final step, films were calcined at different temperatures (300, 350, 400, 450, and 500 ^{o}C) to produce mesoporous nickel oxide (m-NiO) films. At each temperature, the films were calcined for one hour. The mesoporous nickel oxide (m-NiO) films were later used for analysis via XRD, ATR-FTIR, N_2-adsorption-desorption, and SEM-EDX techniques.

2.4. Preparation of the electrodes

To study the electrochemical properties of the m-NiO, the Ni(II) solution was spread on fluorine doped tin oxide (FTO) glass by spin-coating at a rate of 2000 rpm for 10 seconds. These samples were then calcined at different temperatures (250, 300, 350, 400, 450, and 500 ^{o}C) for one hour. The calcined electrodes were then used for the electrochemical characterization of the material. Another set of electrodes was prepared by spin-coating the FTOs at a rate of 3000, 4000, 5000, and 6000 rpm. These electrodes were calcined at 300 ^{o}C for one hour and used for the thickness-dependent electrochemical measurements.

2.5. Instrumentation

2.5.1. Powder x-ray diffraction (XRD) measurements

Small-angle and wide-angle x-rays patterns were recorded on a Rigaku Miniflex diffractometer equipped with a Cu K_α (λ=1.5405 Å) x-ray source and operated at 30 kV and 15 mA. The instrument contains a scintillator NaI (TI) detector with a Beryllium (Be) window. The small-angle XRD patterns (from 1^o to 5^o) of clear solutions were recorded at the scan speed of 1^o/min and step size of 0.01. For this purpose, the Ni (II) solution was drop-casted on the glass slide and then it was placed on the sample holder. For recording the wide-angle XRD patterns (from 10^o to 80^o), the calcined NiO powder was scratched from the glass slides and then uniformly packed in the XRD powder holder. The scan speed was kept at 0.5^o/min for recording the wide-angle XRD patterns with a step size of 0.01.

2.5.2. Attenuated Total Reflection Fourier–Transform Infrared (ATR-FTIR) Spectroscopy

ATR-FTIR spectra were recorded by using a Bruker Alpha Platinum spectrometer. The time-dependent spectra were recorded by putting a drop of clear Ni(II) solution on the ATR Diamond crystal. All spectra were measured by recording 32 scans in the 400 cm^{-1} to 4000 cm^{-1} range, with a resolution of 4 cm^{-1}. The instrument was also used to record the spectra of calcined m-NiO powders. A small amount of powder was placed onto the diamond crystal and gently pressed to ensure proper contact with the crystal.

2.5.3. Polarized Optical Microscopy (POM) Imaging

A ZEISS Axio Scope A1 polarized optical microscope was used for recording the formation of the hexagonal or cubic LLC mesophases. The POM was also coupled with a temperature-controlled Linkman LTS-350 stage for studying the effect of temperature change on the LLC mesophase. For controlling the temperature, Linkman T-95

temperature controller was used and it was also coupled with LNP95 liquid nitrogen pump cooling system.

2.5.4. N_2 Adsorption-Desorption Analysis

To measure the N_2 adsorption-desorption isotherms for analyzing the porosity, pore size, and surface area, a Micrometerics Tristar 3000 automated gas analyzer in the relative pressure range (P/P_o) of 0.01 to 0.99 was used. The calcined samples at different temperatures were scratched from the glass slides, and ground to powders by using mortar & pestle. The samples were dehydrated by keeping under a vacuum (at around 35-40 mTorr) in sample holders (washed with aqua regia and water) for almost 2 hours at 200 ^oC. To evaluate the surface area of each sample, the first five points ranging from 0.05 to 0.3 atm were used with the help of the Brunauer-Emmett-Teller (BET) theory, and the average pore size was determined by using Barret-Joyner-Halenda (BJH) method.

2.5.5. Scanning Electron Microscope (SEM)–Energy Dispersive X-Ray (EDX) Spectroscopy

The SEM images were captured by using FEI Quanta 200 FEG scanning electron microscope. The NiO powders were obtained by calcining and then scratching the calcined films at different temperatures. A very small amount of sample was dispersed on the carbon tape placed on the aluminum stub. All the images were recorded at an operating voltage of 15 kV. To determine the elemental percentage of the powders, the same samples were used for EDX analysis.

2.5.6. Electrochemical Measurements and Analysis

A three-electrode electrochemical cell was used for the electrochemical characterization. The cell consists of a NiO coated FTO – as a working electrode, Ag/AgCl (3.5 M KCl) electrode – as a reference electrode, and a platinum wire – as a counter electrode. A schematic representation of this electrochemical cell is shown in Figure 2.1. Cyclic voltammetry measurements were carried out at -0.4 V to 1.4 V and 50 mV/s scan rate by using a Gammry 750 (PCI4G750-49046) electrochemical workstation. The electrolyte

used for all the electrochemical studies is 1 M KOH solution. The current densities recorded by using a Ag/AgCl (3.5 M KCl) reference electrode, were later corrected in terms of a normal hydrogen electrode (NHE).

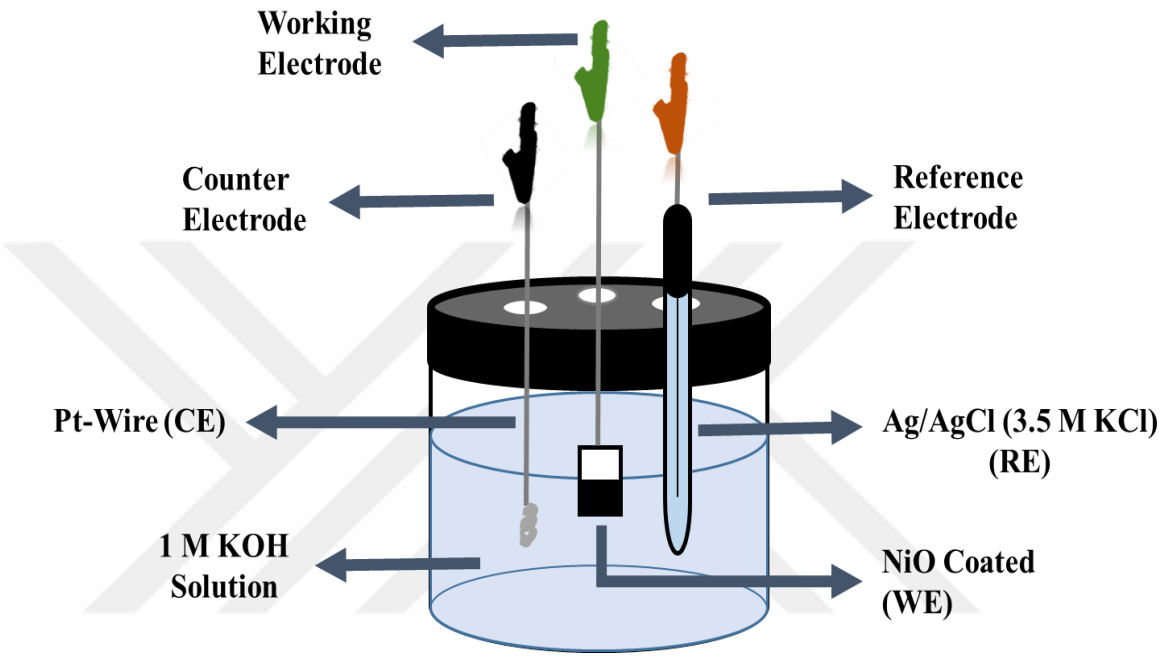

Figure 2.1. Schematic representation of three-electrode system – electrochemical cell.

Chapter 3

3. Results and Discussion

3.1. Characterization of Lyotropic liquid crystal mesophases

3.1.1. Stability of solutions

The solutions of Ni-n-Si-x were prepared to investigate the effect of silica on LLC mesophases in the first step of this synthesis. All the solutions were prepared as explained in the experimental part by keeping the concentration of Ni(II), a charged surfactant CTAB, a non-ionic surfactant $C_{12}E_{10}$, water as a solvent, and HNO_3 the same but varying the concentration of TMOS as the silica source. These solutions were stable up to approximately 6 hours to months depending on the concentration of TMOS. The solution with the highest concentration of TMOS was stable up to 6 hours. However, if the nitric acid is not added to the solution prior to TMOS then the solution is highly unstable and it precipitates very quickly. To investigate the instability in the absence of nitric acid, different solutions were prepared with different compositions. In the first place, the amount of solvent was increased from 5 mL to 50 mL. The 50 mL solution also gives precipitates in almost similar period. Then the concentration of Ni(II) salt was decreased from 6-mole ratio of Ni(II)/$C_{12}E_{10}$ to 1-mole ratio. The solution with this composition precipitates after 1-day aging. However, the solution with 1.5 mole ratio of Ni(II)/$C_{12}E_{10}$ precipitates in 3 hours, and the precipitates were suspended in the solution making it

cloudy. These precipitates were also obtained by using ($[Co(H_2O)_6](NO_3)_2$) salt in Co(II)/ $C_{12}E_{10}$ mole ratio.

These precipitates were separated from the solution through filtration, washed with ethanol, and dried in air for a few hours. Once dried, the powder samples were ground into fine white powder by using a mortar pestle. The ATR-FTIR spectra and X-ray diffraction pattern of this dried fine powder were recorded.

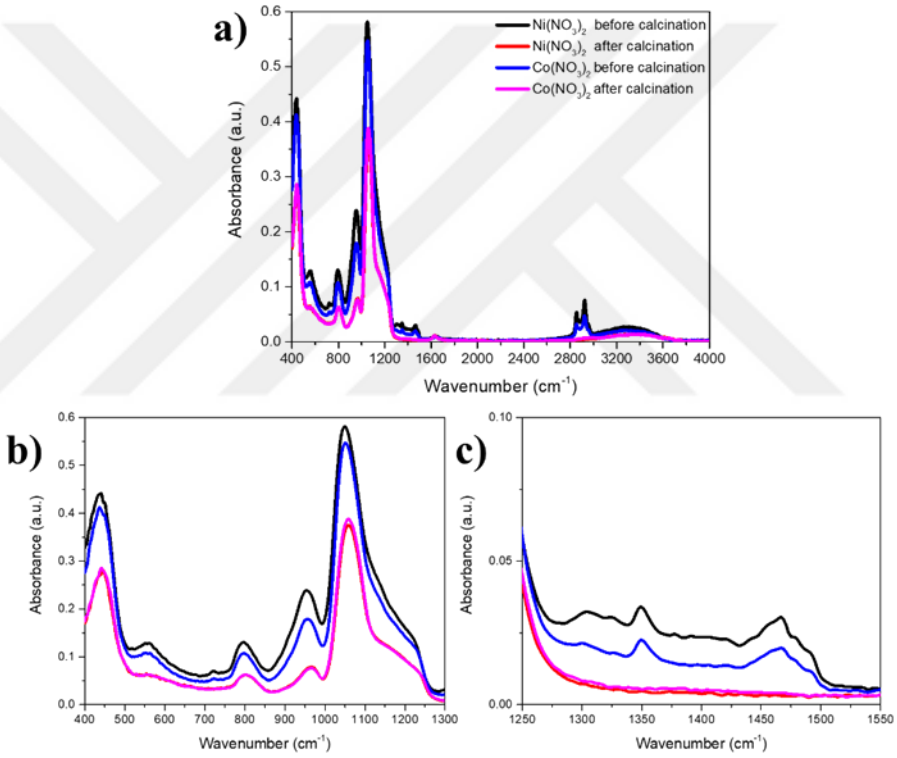

Figure 3.1. ATR-FTIR spectra of m-SiO_2 (a) before and after calcination (b) 400-1300 cm^{-1} region (c) 1250-1550 cm^{-1} region.

Figure 3.1. shows the ATR-FTIR spectra before and after calcination of m-SiO_2 synthesized by using cobalt(II) and nickel(II) salts. The spectra show the most intense peak at 1062 cm^{-1} which belongs to Si-O-Si bond-asymmetric stretching[96]. Moreover, the peaks at around 800 cm^{-1} and 400 cm^{-1} correspond to the symmetric stretching and

rocking mode of the Si-O-Si bond. The peak at around 950 cm^{-1} belongs to the silanol (Si-OH) group[96], [97] and it can be seen that the intensity of this peak sharply decreases after calcination which indicates the condensation of the silanol groups to form a silica network. The spectra also show the characteristic surfactant peaks in the 2800 - 3000cm^{-1} region and these peaks disappear after calcination which shows that the surfactant is completely removed from the sample. Also, very small nitrate peaks are also present and after calcination, these nitrates are removed completely as indicated by the absence of these peaks in the spectra after calcination.

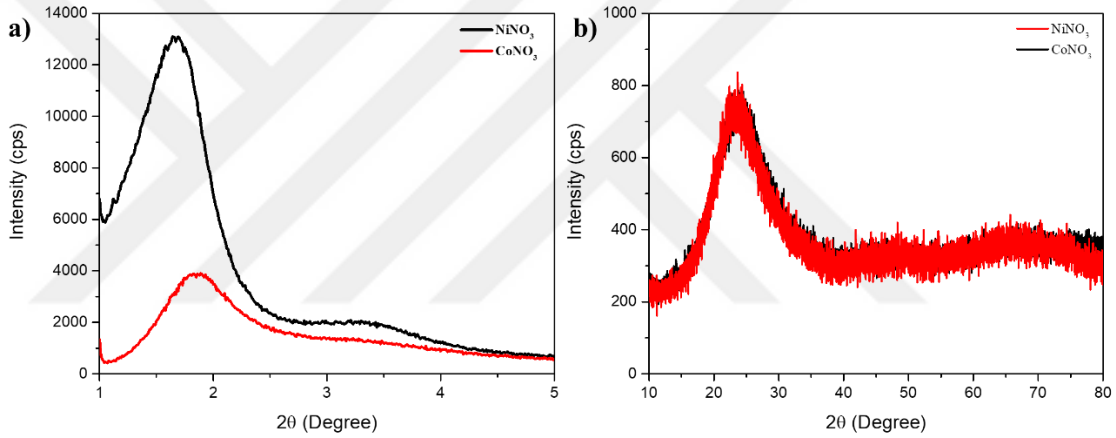

Figure 3.2. (a) small angle XRD pattern of m-SiO_2 and (b) wide angle XRD pattern of m-SiO_2 after calcination.

Figure 3.2(a) shows the small angle XRD pattern of dried powder after calcination. It shows a broad diffraction line at around 1.6 and 1.8^o, 2θ which shows that the material is ordered. The position of diffraction line shows a very minor change which indicates that the particles synthesized by cobalt(II) have larger unit cell. The wide angle XRD patterns in the Figure 3.2. (b) also shows a broad diffraction line at around 23^o, 2θ which is a characteristic of amorphous silica as present in the quartz glass. However, the absence of further peaks in the material also shows the absence of crystalline impurities.

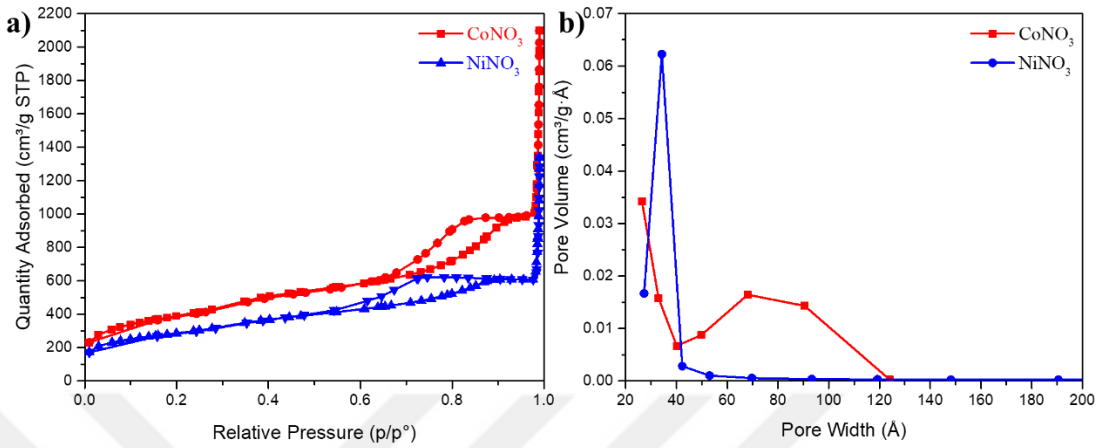

Figure 3.3. (a) N_2 adsorption-desorption isotherms of m-SiO_2 and (b) pore size distribution plot of m-SiO_2.

Figure 3.3(a) shows the N_2-adsorption-desorption isotherms of the m-SiO_2 sample calcined at 450 ^oC for two hours. As shown in Figure 3.3 (a), the isotherms are type IV, which is characteristic for the mesoporous materials. The BET surface area is 748 m^2/g for the particles synthesized by using nickel(II) with a uniform pore size of 34 Å whereas the BET surface area is 1395 m^2/g for the particles synthesized by using cobalt(II) with pore size of 68 Å, see Figure 3.3. (b).

Figure 3.4 and 3.6 show the SEM images of m-SiO_2 synthesized using Ni(II) and Cobalt(II) salts respectively and display that the m-SiO_2 has a film morphology. Moreover, Figure 3.5 shows the EDX spectrum of the same material synthesized using Ni(II). From the spectrum, it is clearly shown that the m-SiO_2 doesn't contain any nickel species. The EDX spectrum of m-SiO_2 synthesized using cobalt(II) also doesn't show any cobalt species in the sample, see Figure (3.7).These spectra only display oxygen and silicon peaks as the constituent elements which further confirms that the precipitates are pure m-SiO_2 in EDX detection limits.

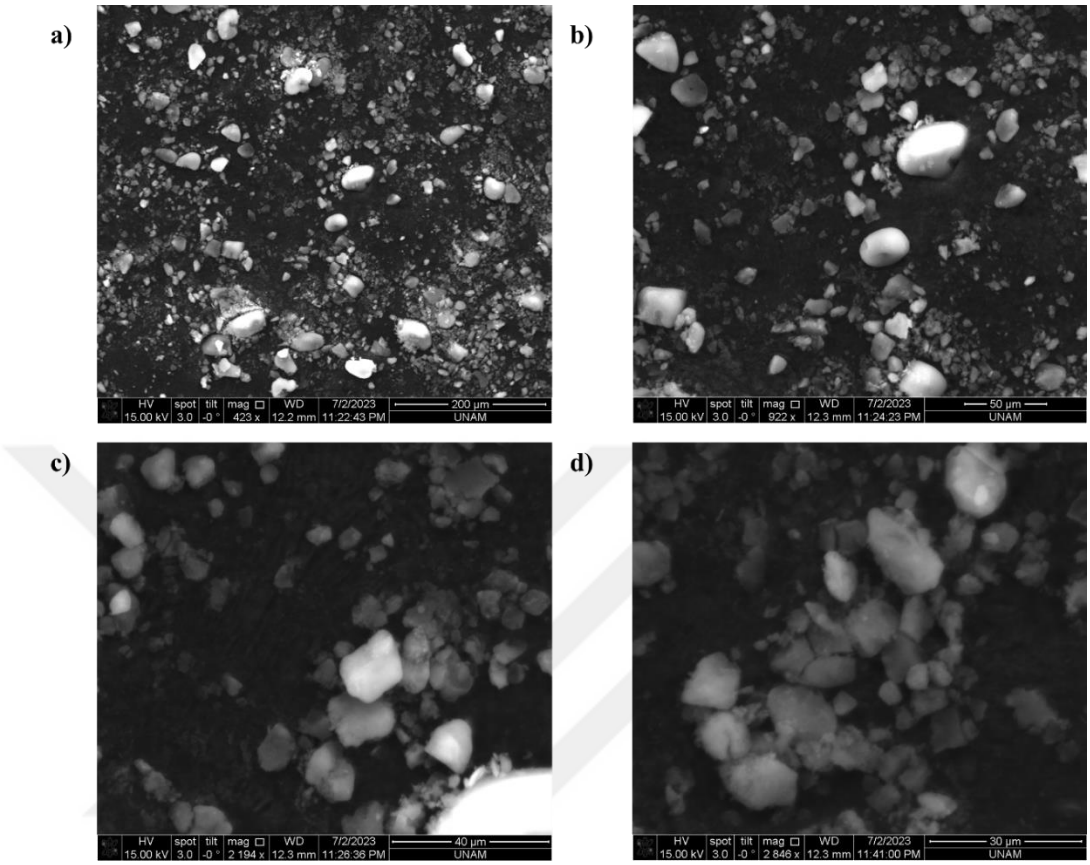

Figure 3.4. SEM images of m-SiO_2 synthesized using ($[Ni(H_20)_6](NO_3)_2$).

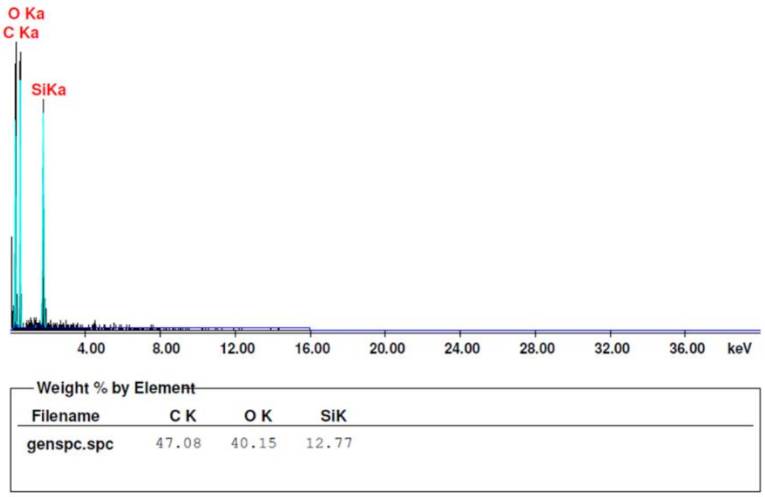

Figure 3.5. EDX spectrum of m-SiO_2 synthesized using ($[Ni(H_20)_6](NO_3)_2$).

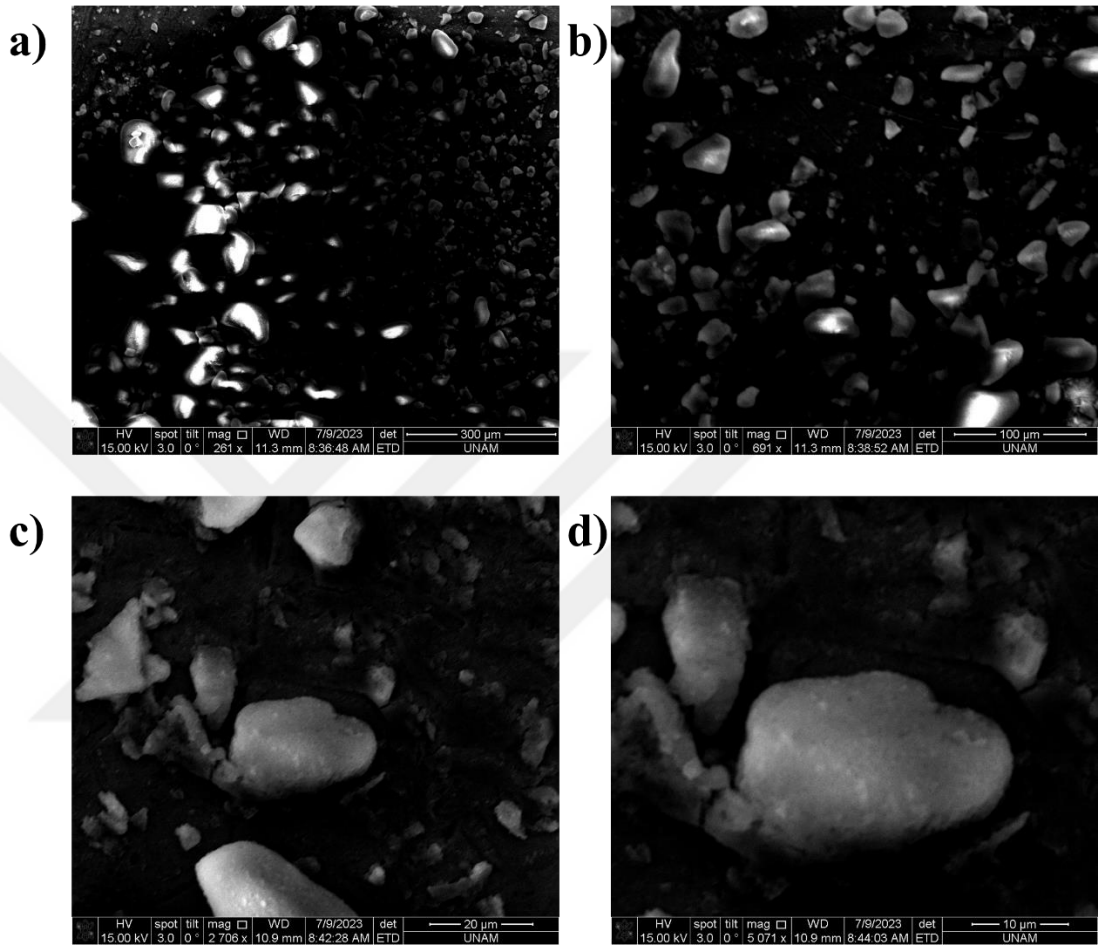

Figure 3.6. SEM images of m-SiO_2 synthesized using $[Co(H_20)_6](NO_3)_2$ salt.

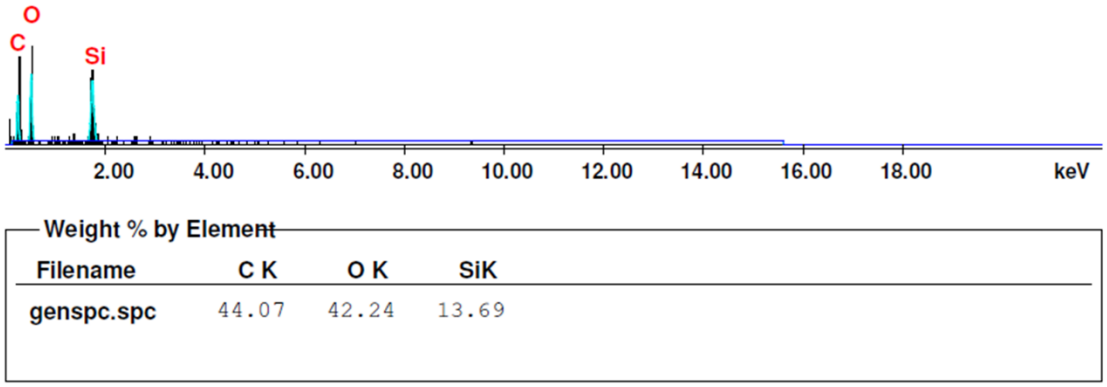

Figure 3.7. EDX spectrum of m-SiO_2 synthesized using $[Co(H_20)_6](NO_3)_2$ salt.

Another solution was prepared using 50 mL solvent by using only one surfactant ($C_{12}E_{10}$) and the same mole ratios of Ni(II)/$C_{12}E_{10}$. This solution also precipitates in almost 3 hours and precipitates were suspended in the solution. Figure 3.8 shows the ATR-FTIR spectrum of the separated precipitates and it can be seen that the spectrum is similar to the material prepared by using both surfactants. The only difference is that it doesn't show the signal due to C-H stretching in 2800-3000 cm^{-1} as $C_{12}E_{10}$ surfactant is used in the synthesis. Moreover, no nitrate species are present in the precipitates and these spectra are typical m-SiO_2 spectra.

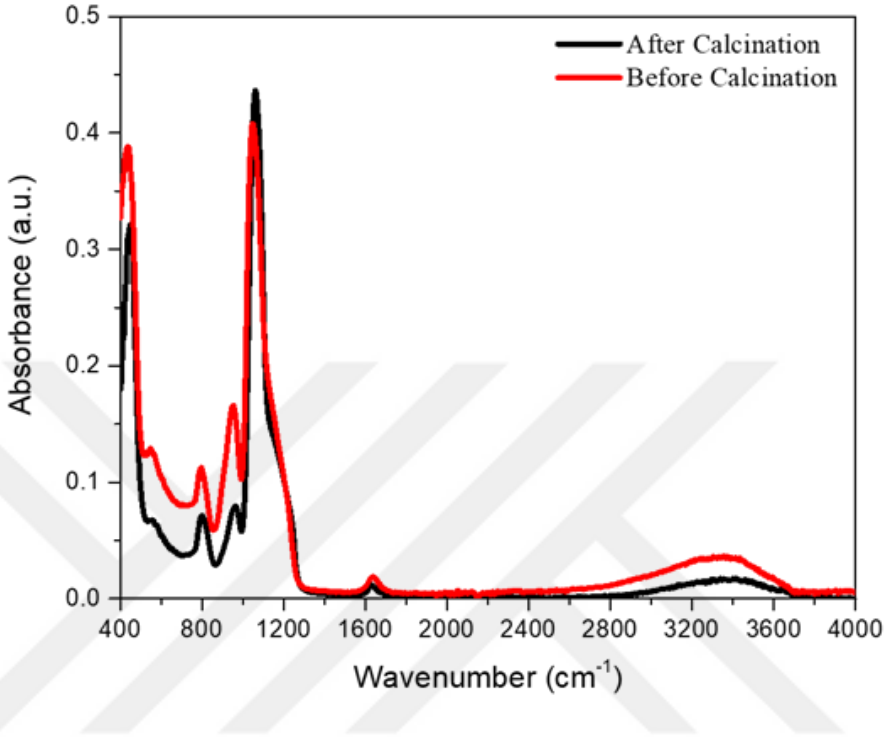

Figure 3.8. ATR-FTIR spectra of m-SiO_2 before and after calcination synthesized using $C_{12}E_{10}$ surfactant.

Figure 3.9. shows the small angle and wide angle XRD pattern of m-SiO_2 synthesized using $C_{12}E_{10}$ surfactant and it can be seen that the diffraction lines are similar to the pattern of the m-SiO_2 synthesized by using both surfactants. The broad diffraction line at 1.9°, 2θ before calcination shifts to the 2.1°, 2θ after calcination. Moreover, the wide angle XRD pattern is similar before and after calcination which shows the diffraction line at 23°, 2θ, a characteristic of amorphous silica.

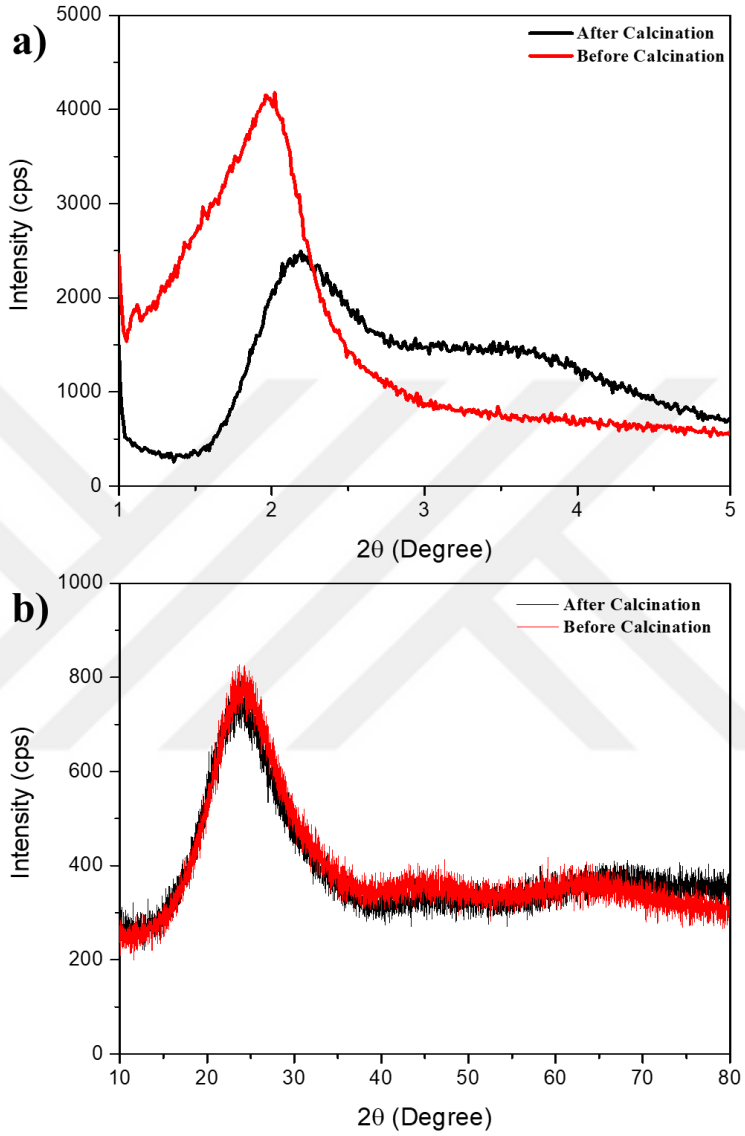

Figure 3.9. (a) small angle XRD pattern and (b) wide angle XRD pattern of m-SiO_2 synthesized using $C_{12}E_{10}$ surfactant.

Figure 3.10(a) shows the N_2-adsorption-desorption isotherm of the m-SiO_2 prepared by using only one surfactant. The isotherm can be classified as the combination of type I and type IV isotherm [98]. This means that it contains both micropores as well as mesopores in the structure with a BET surface area of 746 m^2/g. Figure 3.10(b) shows the BJH pore size distribution plot of the same material and it can be seen that the pore size is not

uniform. It ranges from 5 to 11 Å (in the microporous range). These pores are almost 3 times smaller as compared to the pores of the m-SiO_2 prepared by using both surfactants but the surface area is similar.

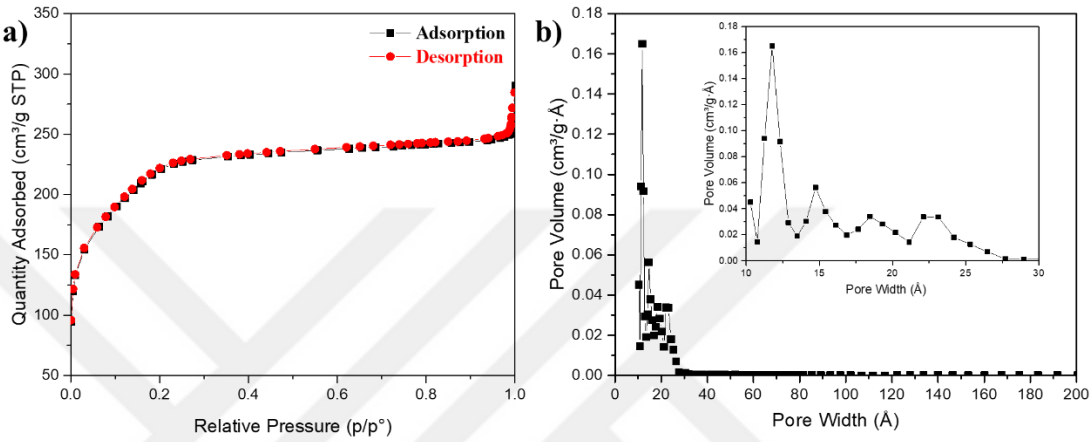

Figure 3.10. (a) N_2-adsorption-desorption isotherm and (b) pore size distribution plot of m-SiO_2 synthesized using $C_{12}E_{10}$ surfactant.

Figure 3.11 shows the SEM images of the microporous silica synthesized using $C_{12}E_{10}$ surfactant and it can be seen that their morphology is spherical which is different than the morphology of m-SiO_2 prepared using both surfactants. Figure 3.12 shows the EDX spectrum of these particles which confirms that there is no impurity in the material and it contains only silicon and oxygen. This also confirms that the material is m-SiO_2.

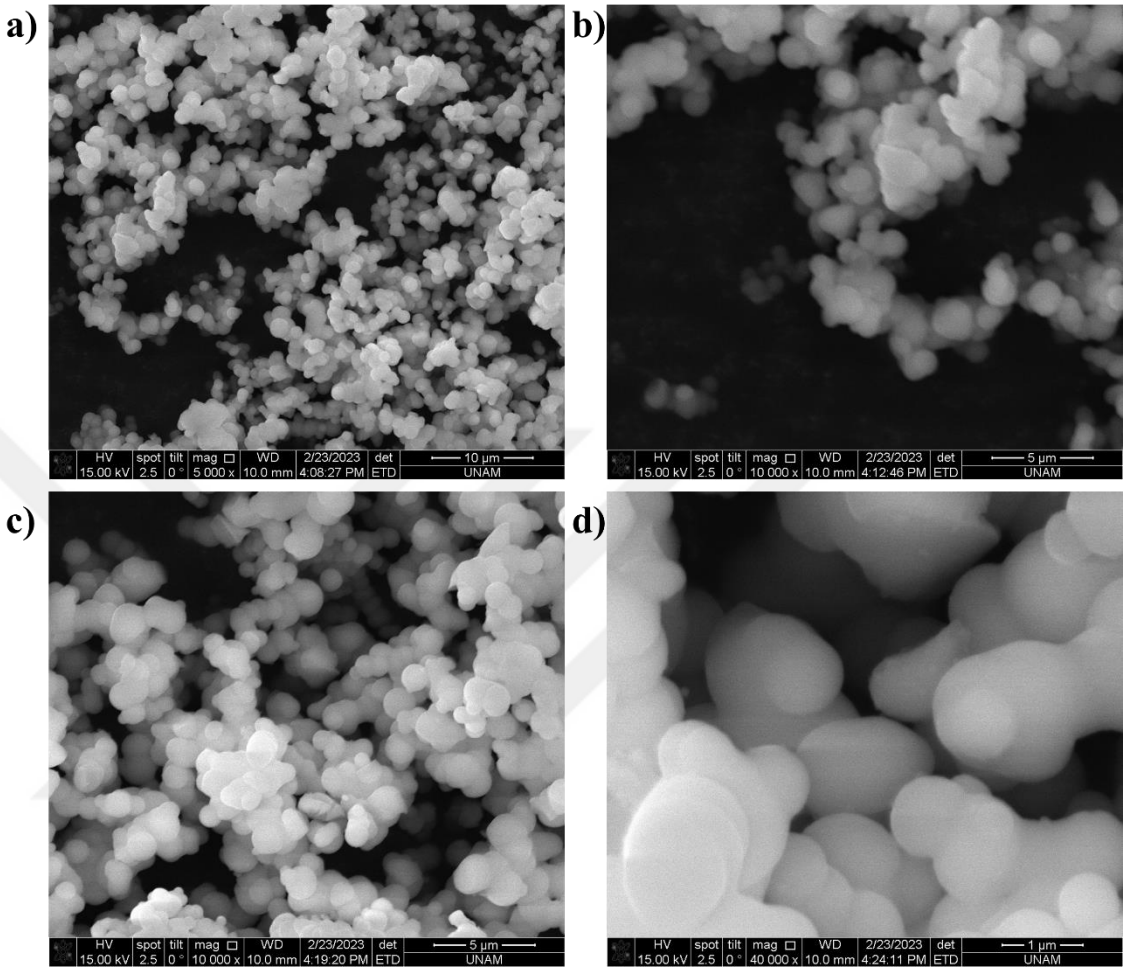

Figure 3.11. SEM images of m-SiO_2 synthesized using $C_{12}E_{10}$ surfactant at different magnifications.

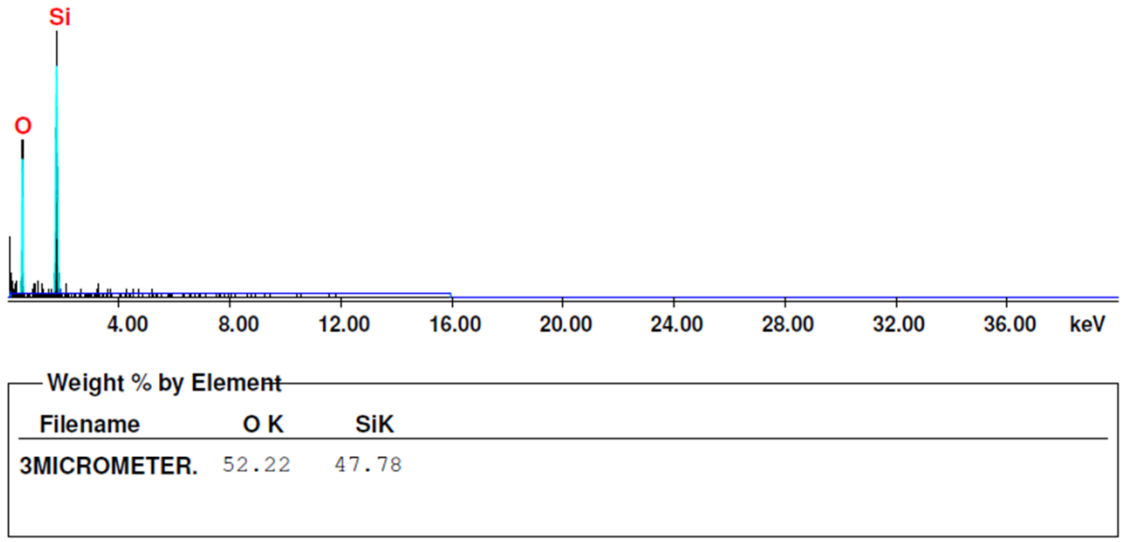

Figure 3.12. EDX spectrum of m-SiO_2 synthesized using $C_{12}E_{10}$ surfactant.

These silica particles were also prepared by using ($[Ni(H_2O)_6](Cl)_2$), ($[Ni(H_2O)_6]SO_4$) and ($[Mn(H_2O)_4](NO_3)_2$) salts. All the salts give the same precipitates. The small-angle XRD patterns are shown in Figure 3.13(a) and the diffraction lines are observed at 1.6°, 2θ, for the $[Ni(H_2O)_6](Cl)_2$) and $[Mn(H_2O)_4](NO_3)_2$ salts while in the case of $[Ni(H_2O)_6]SO_4$, the diffraction line is observed at 1.7°, 2θ, after calcination. The wide-angle XRD pattern in Figure 3.13(b) shows that the diffraction lines are exactly at the same angle 23°, 2θ, for all the salts and originated from the amorphous silica pore-walls.

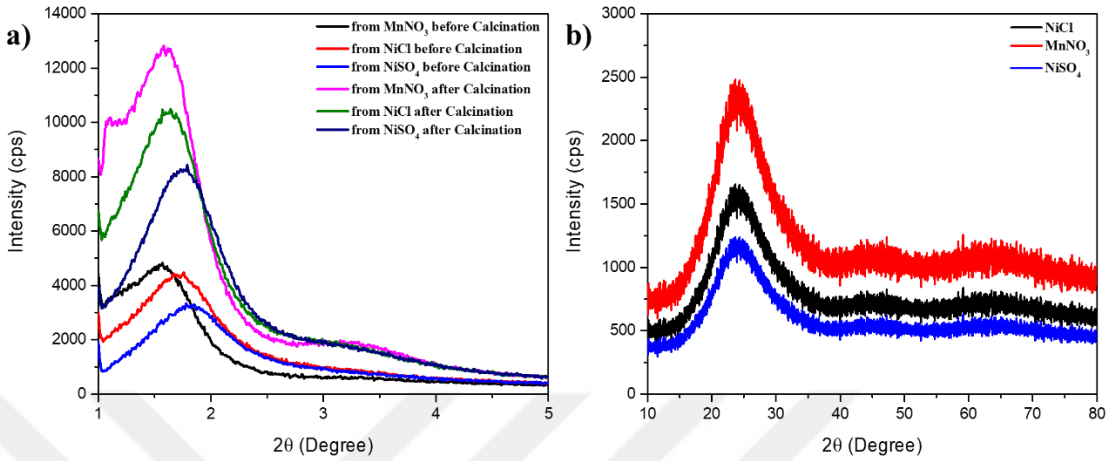

Figure 3.13. (a) The small-angle XRD pattern and (b) wide-angle XRD pattern of m-SiO_2 synthesized by using different transition metal salts.

Figure 3.14 shows the ATR-FTIR of these samples. The spectra are also prove the formation typical amorphous silica. All the peaks are similar to the peaks of the particles synthesized by using other salts. The N_2-adsorption desorption isotherms of these samples are shown in Figure 3.15(a). These samples did not display complete isotherms, due to some unknown reason. The desorption isotherm doesn't undergo completion due to which only adsorption data is shown in Figure 3.15(a). Figure 3.15(b) displays the pore size distribution plots using the adsorption isotherm and the particles synthesized form manganese(II) gives pore size of 32 Å while the others don't show peak to a value, but smaller than that manganese sample.

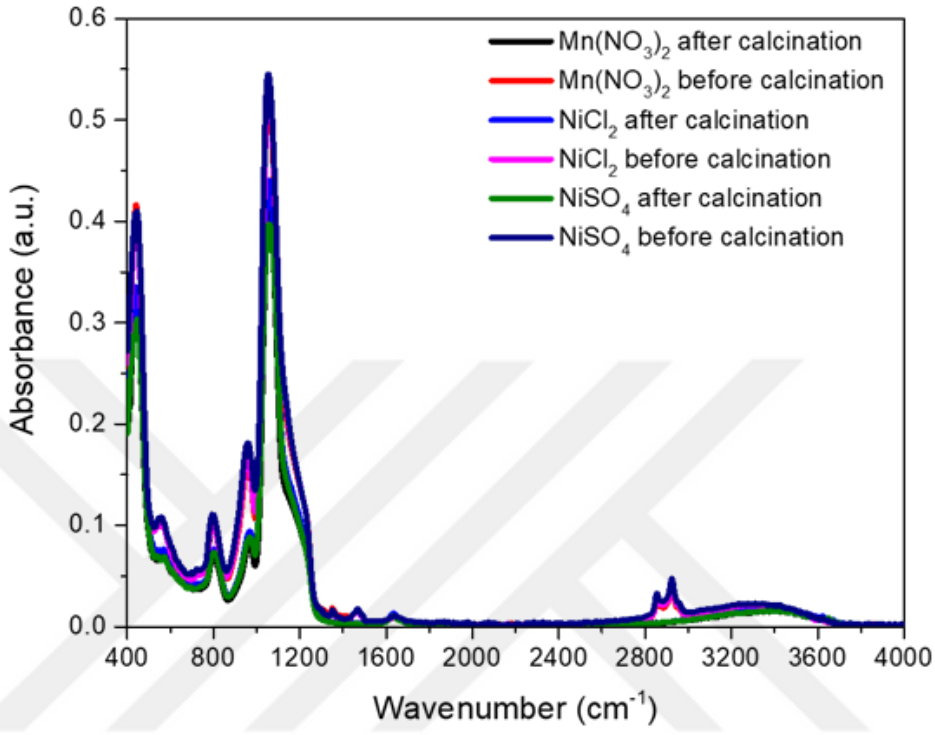

Figure 3.14. ATR-FTIR spectra of m-SiO_2 particles synthesized by using different transition metal salts

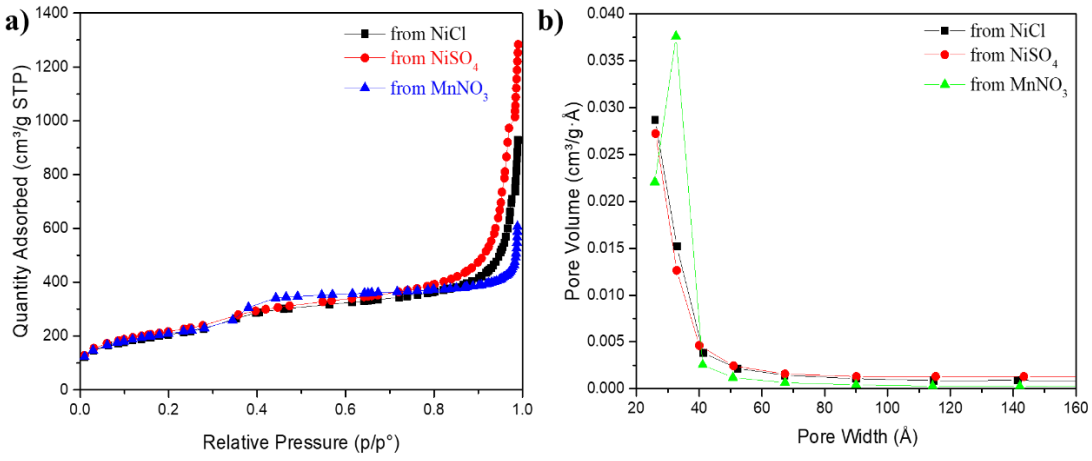

Figure 3.15. (a) The N_2 adsorption-desorption isotherms of m-SiO_2 and (b) pore size distribution plot of m-SiO_2 synthesized by using different transition metal salts.

The SEM images of these particles are also shown in Figure 3.16 and their EDX spectra are shown in Figure 3.17. The images display undefined particle shape. The EDX spectra also don’t show any metal species in its detection limit. This shows that these particles are also pure silica.

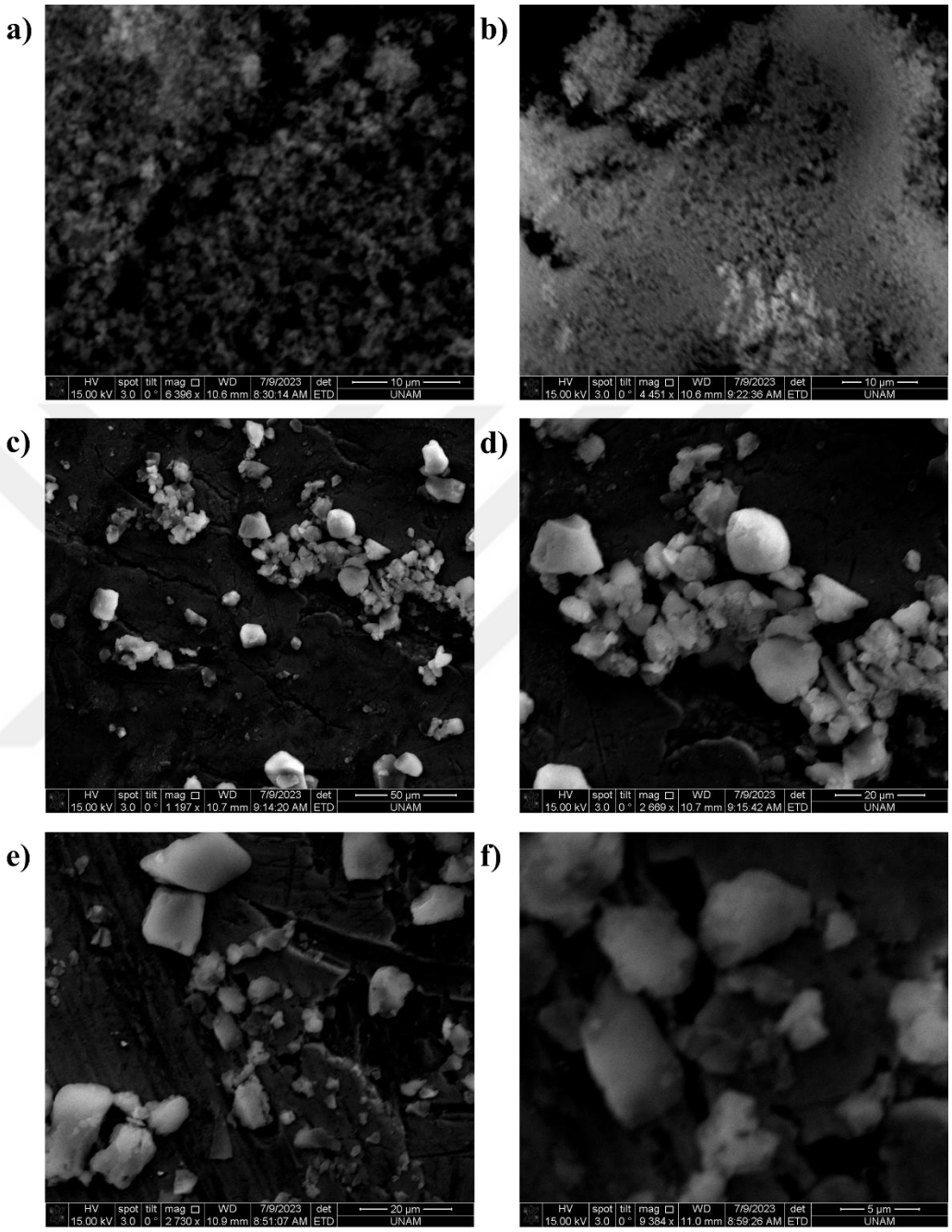

Figure 3.16. The SEM images of m-SiO_2 synthesized by using (a) and (b) $[Mn(H_2O)_4](NO_3)_2$ salt, (c) and (d) $[Ni(H_2O)_6]Cl_2$ salt, and (e) and (f) $[Ni(H_2O)_6]SO_4$ salt.

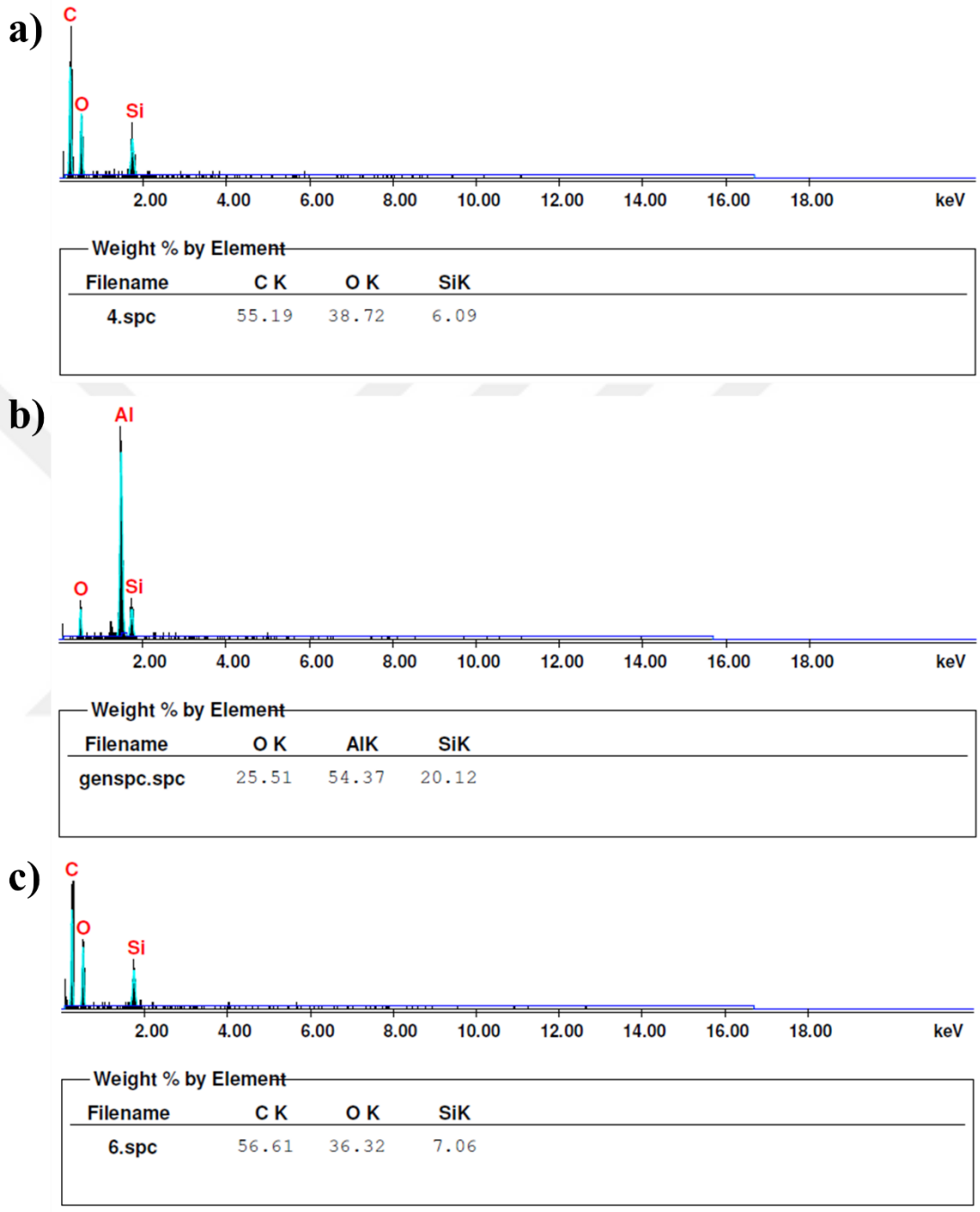

Figure 3.17. The EDX spectra of. m-SiO_2 synthesized by using (a) $[Mn(H_2O)_4](NO_3)_2$ salt, (b) $[Ni(H_2O)_6]Cl_2$ salt, (c) $[Ni(H_2O)_6]SO_4$ salt.

The precipitation of silica occurs due to presence of M(II) ions in the media. M(II) ion is acidic in nature due to which it speeds up the hydrolysis and condensation of TMOS resulting in the synthesis of m-SiO_2 since the hydrolysis occur rapidly in the acidic medium resulting in the formation of $Si(OH)_4$s. Moreover, the M(II) can interact with the –OH group of silanol species which can further activate them leading to the rapid condensation to form siloxane (Si-O-Si) linkage. A general scheme of chemical reaction showing the catalytic activity of transition metal salts is as follows and schematically shown below.

1. Hydrolysis of TMOS

$$Si(OCH_3)_4 + 4H_2O \rightarrow Si(OH)_4 + 4CH_3OH$$

2. Coordination to transition metal salt to $Si(OH)_4$ and $(CH_3O)_3SiOH$

$$[M(H_2O)_6]^{2+} + 2Si(OH)_4 \rightarrow [(HO)_3Si\text{-}O(H)\text{-}M(H_2O)_4\text{-}(H)O\text{-}Si(OH)_3]^{2+} + 2H_2O$$

$$[(HO)_3Si\text{-}O(H)\text{-}M(H_2O)_4\text{-}(H)O\text{-}Si(OH)_3]^{2+} + 2H_2O \rightarrow [M(H_2O)_6]^{2+} + (HO)_3Si\text{-}O\text{-}Si(OH)_3$$

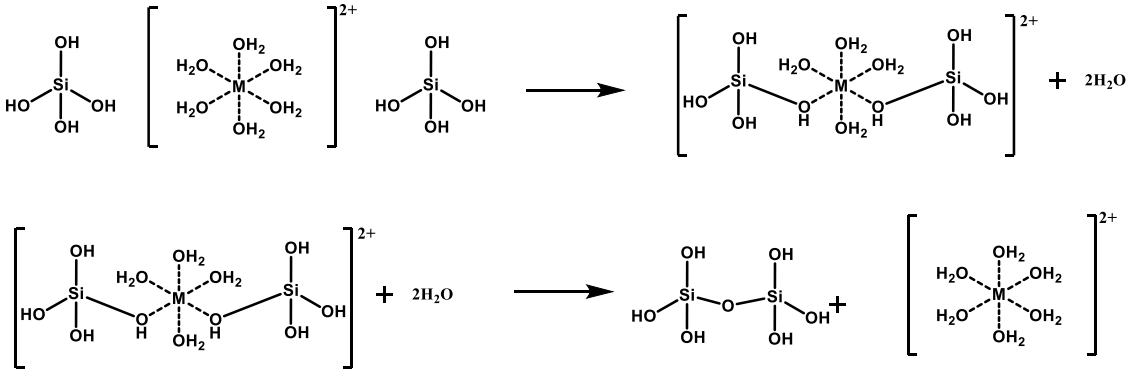

3. overall reaction

$$nSi(OCH_3)_4 + [M(H_2O)_6]^{2+} + nH_2O \rightarrow [\text{-}Si\text{-}O\text{-}Si\text{-}]_n + [M(H_2O)_6]^{2+} + nCH_3OH$$

Acid is known to be a good catalyst for the hydrolysis of TEOS or TMOS and condensation reactions. Notice in this investigation that the addition of extra acid to above media stabilize the clear solutions. It means that the hydrolysis and condensation reaction

either do not take place or slow down extensively. Therefore, M(II) ions act like much better catalysts for the hydrolysis and condensation reaction and produce mesoporous silicates. These behaviors of the transition metal ions are shown for the first time in the literature and important for the synthesis of mesoporous silicates. Moreover, the remaining silica solutions that contains only metal salt species can be used over and over again to produce silicates and are cost effective.

3.1.2. Time-dependent studies of stable solutions

The stable solutions of Ni-n-Si-x were further investigated to study the effect of silica on LLC mesophases. All the solutions were prepared as explained in the experimental part by keeping the concentration of Ni(II), a charged surfactant CTAB, a non-ionic surfactant $C_{12}E_{10}$, water as a solvent, and HNO_3 the same but varying the concentration of TMOS as the silica source. In the next step, the clear solution is drop-casted on the glass slides to obtain the gel phase of the solution. After the drop-casting, the solvent evaporates and forms the LLC mesophase as a thick film. The gel phase is characterized by using ATR-FTIR spectroscopy, POM imaging, and small angle x-ray diffraction (XRD) techniques. These films were investigated in a wide range of silica-to-salt ratios, starting from 0.1 to 6-mole ratio. The freshly prepared mesophases were described as Ni-*n*-Si-*x*, where *n* is the Ni(II)/$C_{12}E_{10}$ mole ratio and *x* is the Si/$C_{12}E_{10}$ ratio (for example a solution with the composition 6 Ni(II)/$C_{12}E_{10}$ ratio and 0.1 Si/$C_{12}E_{10}$ ratio is described as Ni-6-Si-0.1).

Figure 3.18 (a) shows the time dependent ATR-FTIR spectra of Ni-6-Si-0.1 composition. It indicates the presence of large amount of solvent initially at 0 minutes (3323 cm^{-1}) and small concentration of free nitrate ions (1340 cm^{-1}). However, with the evaporation of solvent as the solution starts forming the gel phase, after 10 minutes the concentration of free nitrates increases indicated by the increase in the intensity of nitrate peak at 1323 cm^{-1} and the concentration of water (solvent) decreases as indicated by the intensity of peak at 3323 cm^{-1}. Moreover, the emergence of shoulder after 10 minutes at 1384 cm^{-1} shows that some of the free nitrates are interacting with the Ni(II), likely as an ion-pair as observed in the molten phase of nickel nitrate hexahydrate, see Figure 3.18(c). The metal bonded nitrates appear at higher and lower wavenumbers due to the change in symmetry

of free nitrate ions and splitting of the doubly degenerate modes. The free nitrate ions are planar with a D_{3h} symmetry point group and on bonding to the metal the symmetry becomes C_{2V}. The metal bonded nitrates increase with the decrease in the amount of solvent as shown in Figure 3.18(c). The presence of acid in the solution facilitates the hydrolysis and condensation process of TMOS. However, it is difficult to observe the TMOS at the beginning as the Si-O-C (from TMOS) and C-O-C (from $C_{12}E_{10}$) lie in the same IR region at 1089 cm^{-1} as shown in Figure 3.18(c). As the silica hydrolyses and condenses over the time, new peaks appear at 942 and 816 cm^{-1}, which supports the polymerization of TMOS to form a silica network.

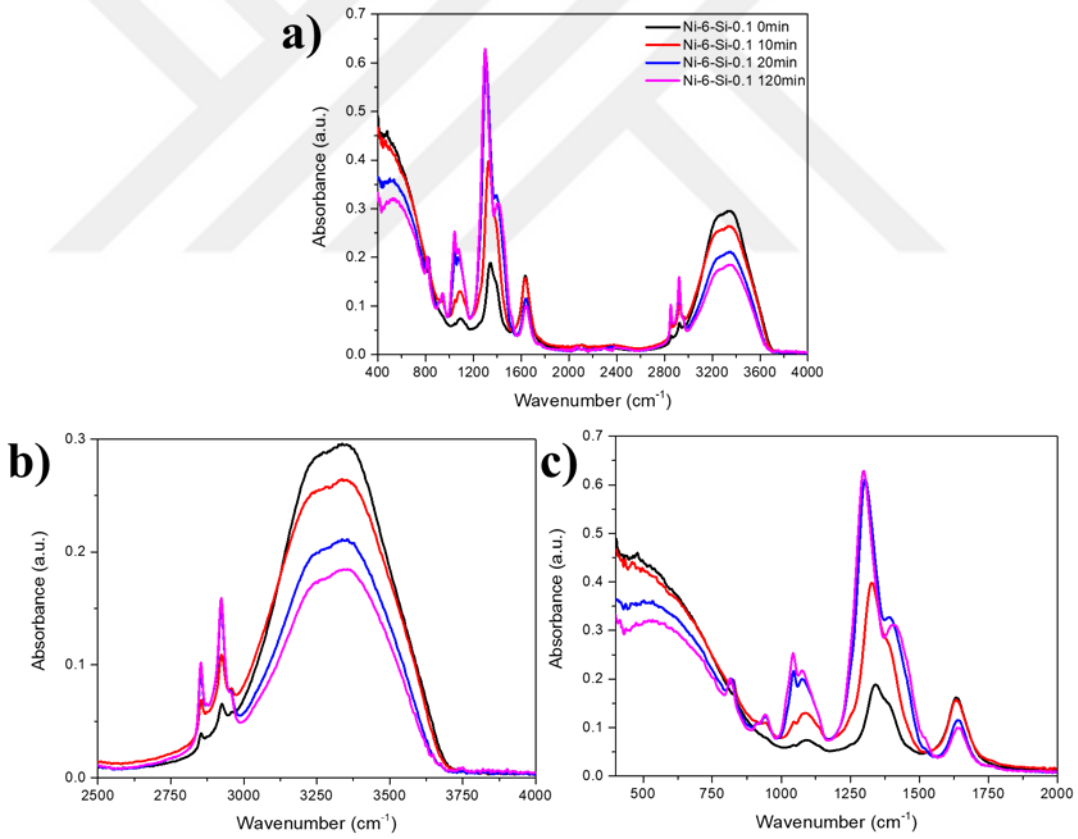

Figure 3.18. (a) Time dependent ATR-FTIR spectra of Ni-6-Si-0.1 composition (b) 2500-4000 cm^{-1} region of Time dependent ATR-FTIR spectra of Ni-6-Si-0.1 composition and (c) 400-2000 cm^{-1} region of Time dependent ATR-FTIR spectra of Ni-6-Si-0.1 composition.

The spectra are normalized using the surfactant related peaks at around 2800-3000 cm^{-1} region to be able of follow the spectral changes during aging (solvent evaporation and silica polymerization processes). Figure 3.19(a) shows the normalized spectra of the same mole ratio at 0 min and 120 min with respect to the C-H surfactant peak at 2923 cm^{-1} and it gives more accurate information in terms of composition (solvent, surfactant, nitrate, etc.). The spectra display, with the decrease in amount of solvent, the concentration of nitrate species remains nearly the same as the area under the curves in Figure 3.19(c) are nearly the same. However, after 120 min, the main nitrate peak at 1340 cm^{-1} splits into two peaks, one at 1297 cm^{-1} and the other at 1417 cm^{-1}, indicating the presence of coordinated nitrate ions to Ni^{2+} sites, see Figure 3.19(b).

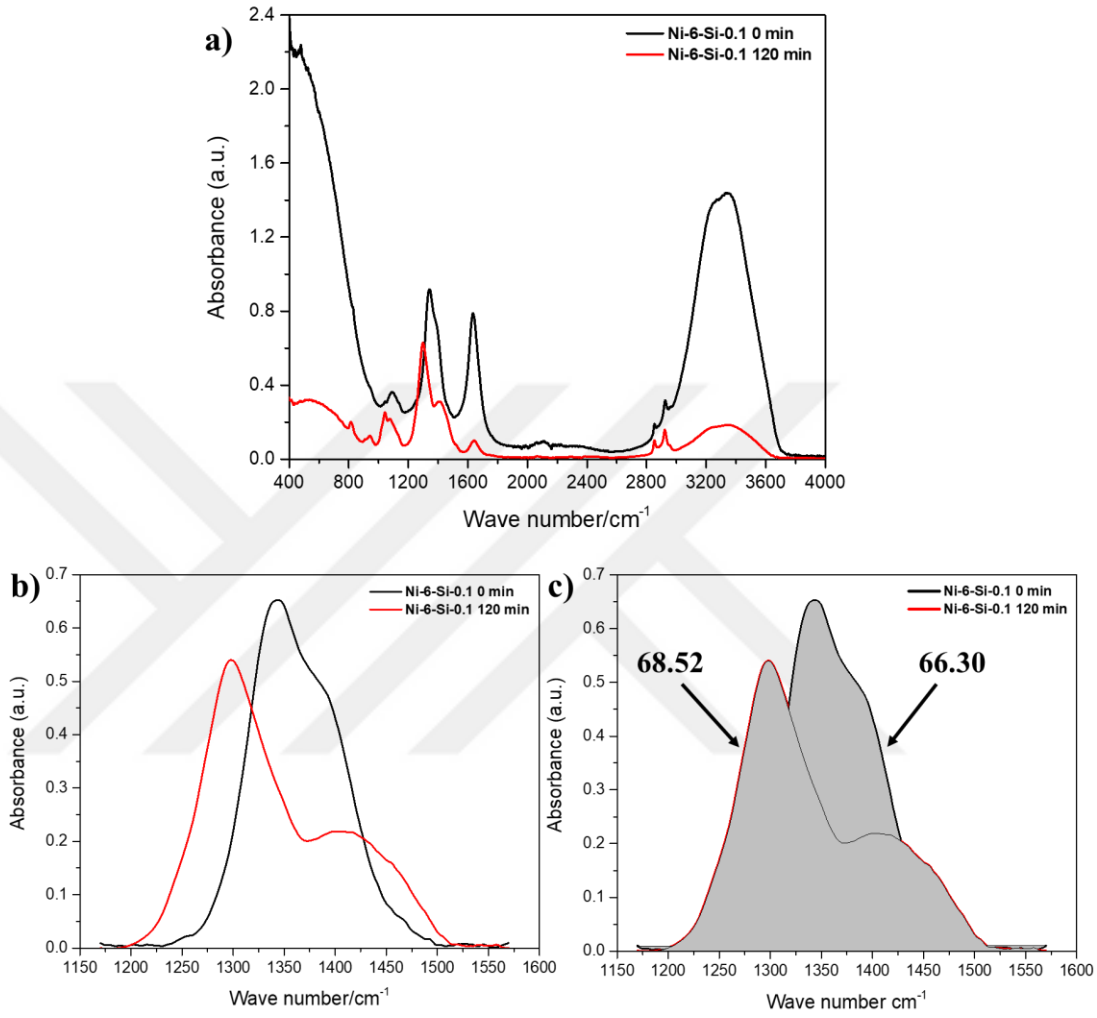

Figure 3.19. Time dependent normalized ATR-FTIR spectra of Ni-6-Si-0.1 composition a) 0 min and 120 min, b) nitrate region of 0 min and 120 min, and c) area under curve of 0 min and 120 min nitrate region.

Similarly, the spectra of all the other compositions, up to Ni-6-Si-1, are recorded that they all have very similar behaviors. However, with the increase in silica concentration, the polymerization rate increases. The time dependent normalized ATR-FTIR spectra of these compositions are shown in Figure 3.20.

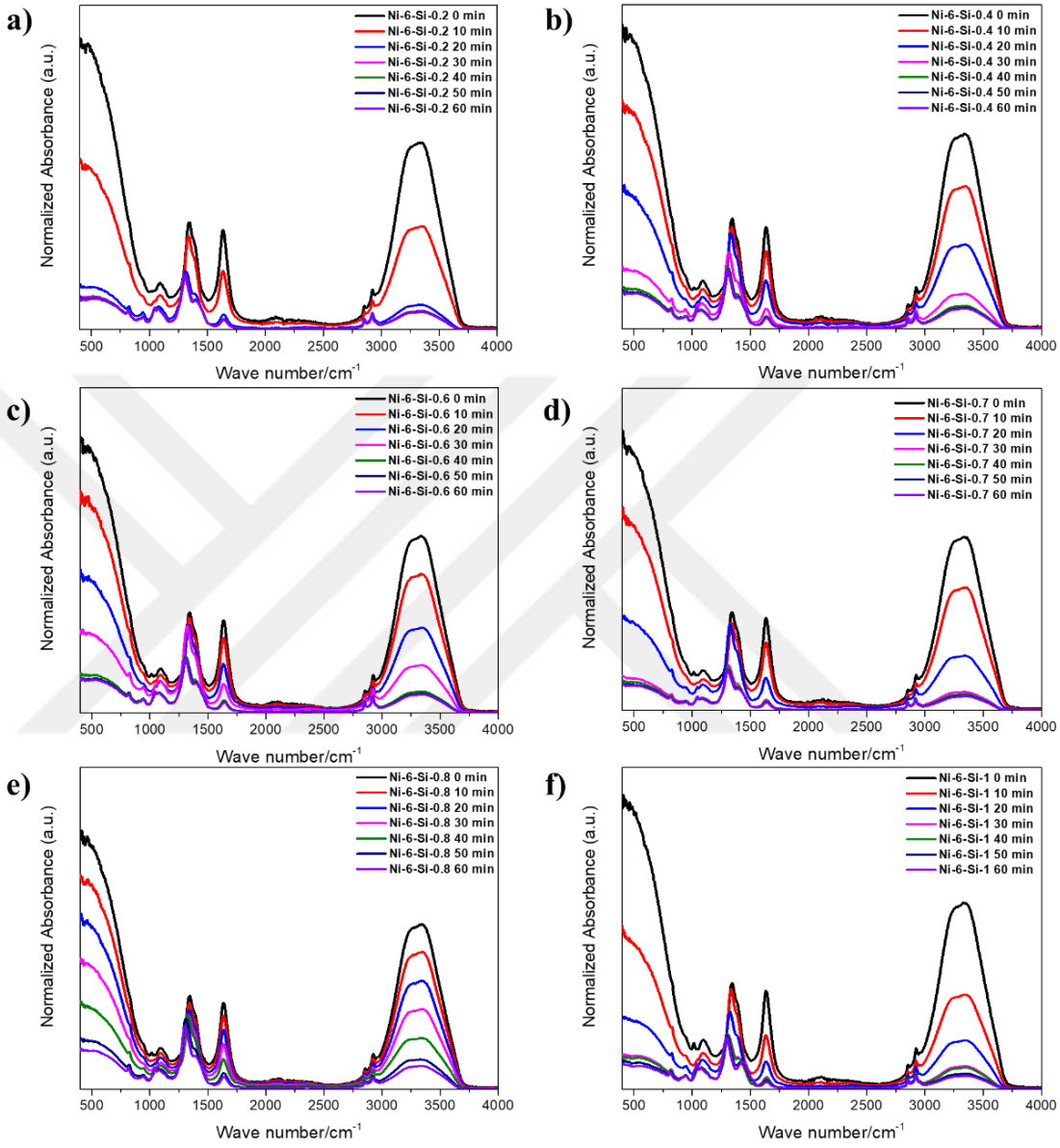

Figure 3.20. Time dependent normalized ATR-FTIR spectra of a) Ni-6-Si-0.2, b) Ni-6-Si-0.4, c) Ni-6-Si-0.6, d) Ni-6-Si-0.7, e) Ni-6-Si-0.8, and f) Ni-6-Si-1 compositions.

XRD patterns of all these compositions are also shown in Figure 3.21. As shown in the patterns, all compositions display diffraction line(s) and showing the formation of a mesophase on the glass slide.

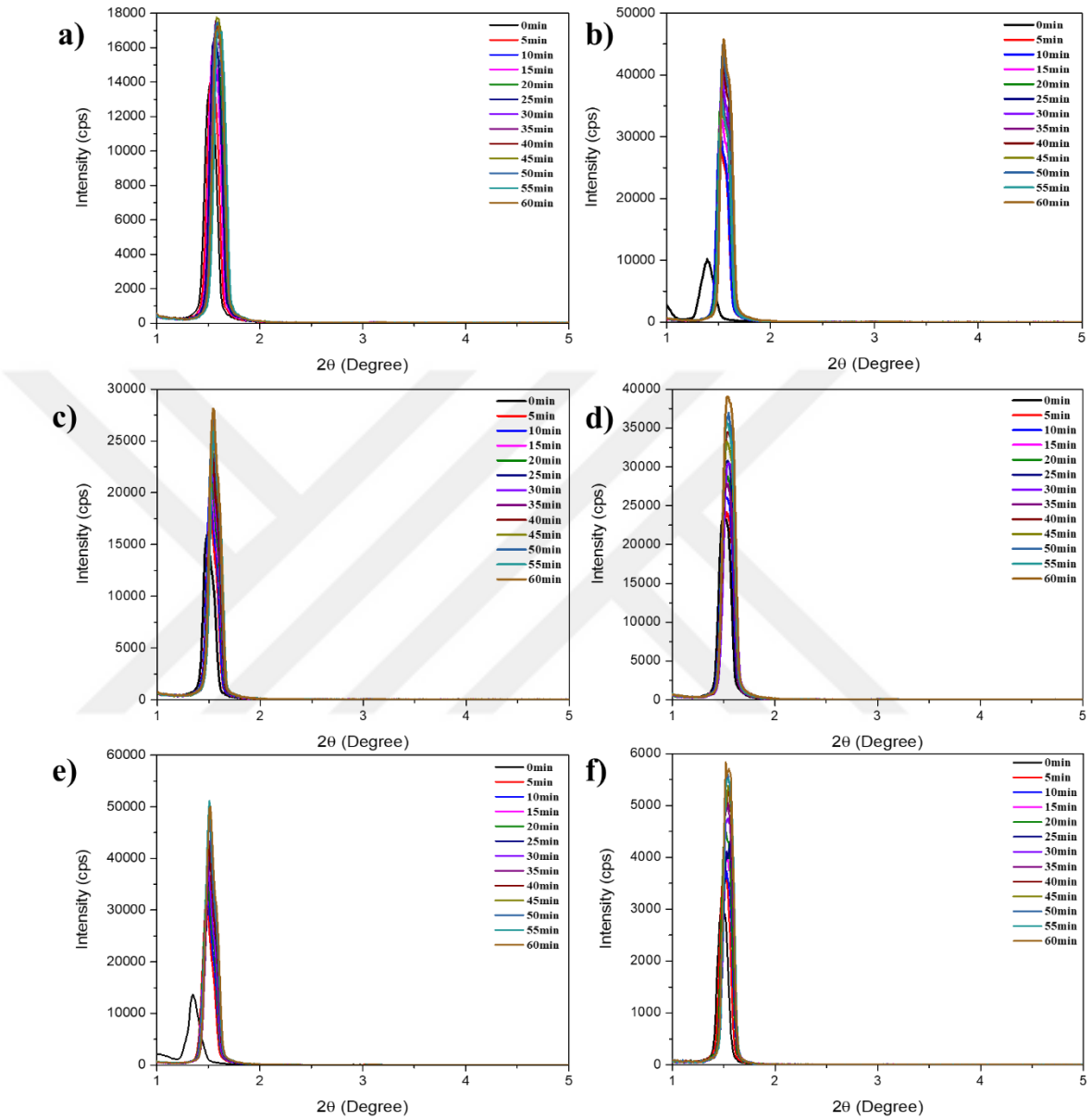

Figure 3.21. Small angle XRD patterns of a) Ni-6-Si-0.2, (b) Ni-6-Si-0.4, (c) Ni-6-Si-0.6, (d) Ni-6-Si-0.7, (e) Ni-6-Si-0.8 and (f) Ni-6-Si-1.

Figure 3.22 shows the time dependent small angle XRD patterns and POM images of the Ni-6-Si-4 and Ni-6-Si-6 samples. Both compositions show the diffraction lines at small angles, indicating the formation of the mesophases. Moreover, the POM images of both

compositions exhibit a characteristic hexagonal mesophase fan texture and also correlate that the diffraction lines at small angle in both the compositions belong to 2D hexagonal phase. However, with high silica concentration in Ni-6-Si-6, as the solvent evaporates and silica polymerizes, the salt leaches out and the intense diffraction line at 1.54°, 2θ shifts to a higher angle, observed at 1.7°, 2θ, with the aging.

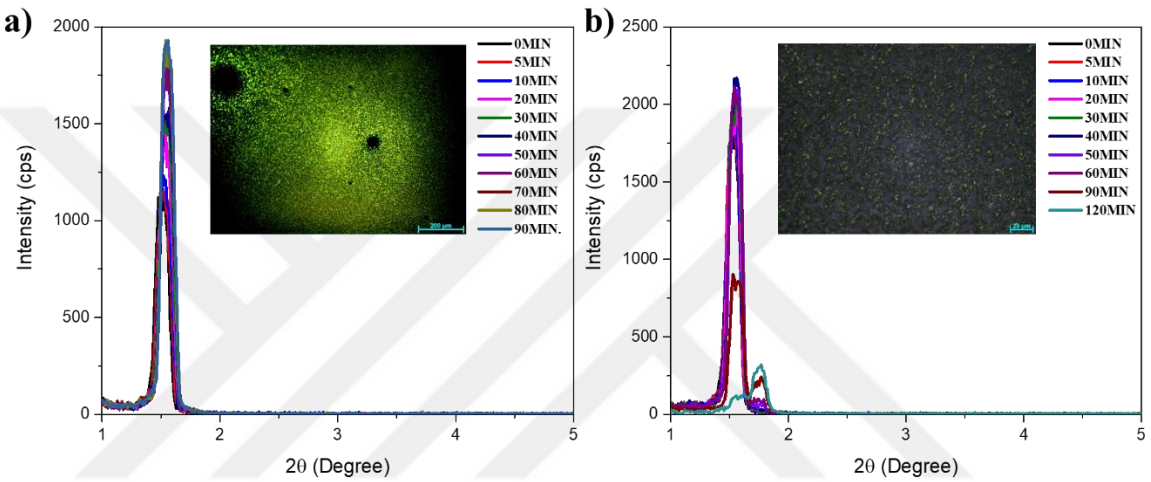

Figure 3.22. Small angle X-ray diffraction patterns and POM images of a) Ni-6-Si-4 and b) Ni-6-Si-6 compositions.

Figure 3.23. shows the effect of heating these mesophases under the POM. The hexagonal mesophase melts on heating and transforms to a cubic mesophase as its POM image appears dark at high temperature. However, on cooling to room temperature (RT) the hexagonal phase re-appears. The phase transfromation, from a hexagonal to cubic phase (or simply the mesophase melts) on heating under POM, is a cyclic process and silica species cannot retain the hexagonal structure at high temperatures. However, at RT due to the rapid formation of the mesophase and further silica polymerization, the salt spcies crystallize and leach out as salt crystals, see POM images in Figure 3.23. Figure 3.24 shows the time-dependent ATR-FTIR spectra of these compositions. The spectra display decrease in amount of free nitrate species with the evaporation of the solvent. These free nitrate species are decomposed in the form of nitric acid during heating and also some of

the nitrates are coordinated to the metal. However, with increasing silica concentration, a rapid polymerization of silica is observed as compared to the earlier compositions of lower silica concentrations.

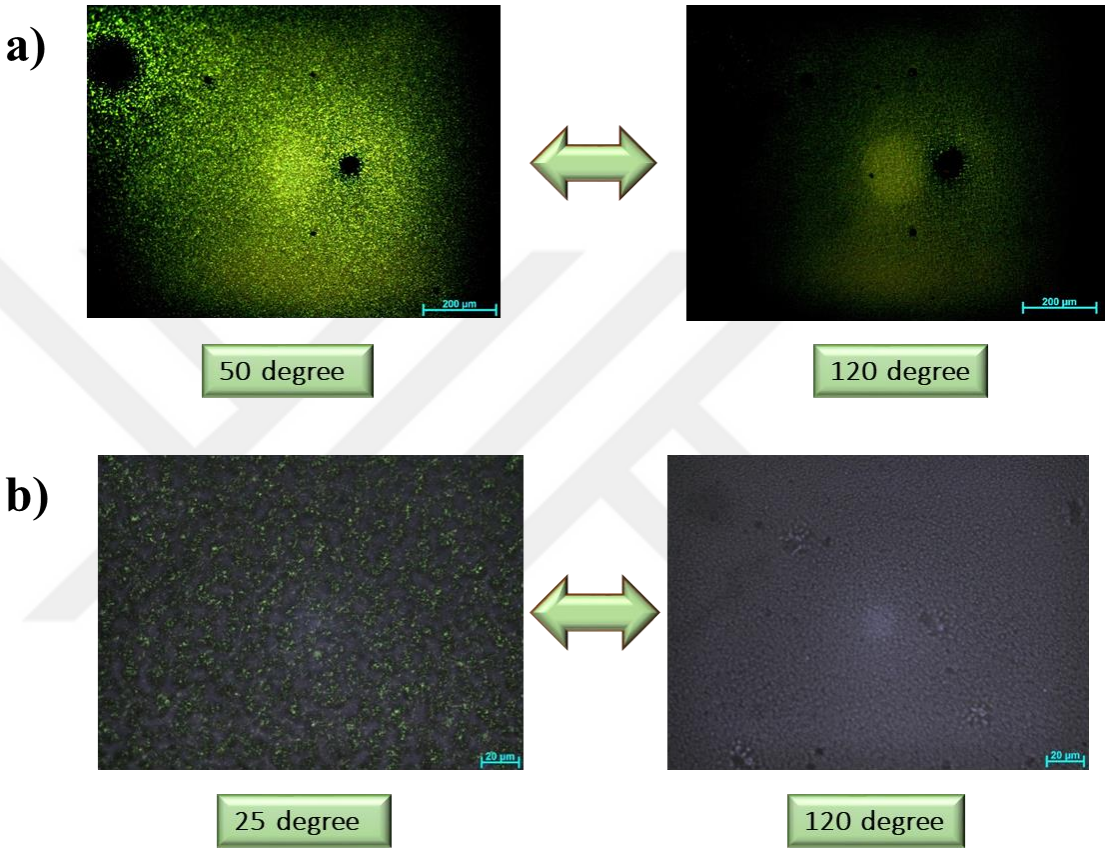

Figure 3.23. POM images showing the effect of heating on mesophases a) Ni-6-Si-4 and b) Ni-6-Si-6 compositions.

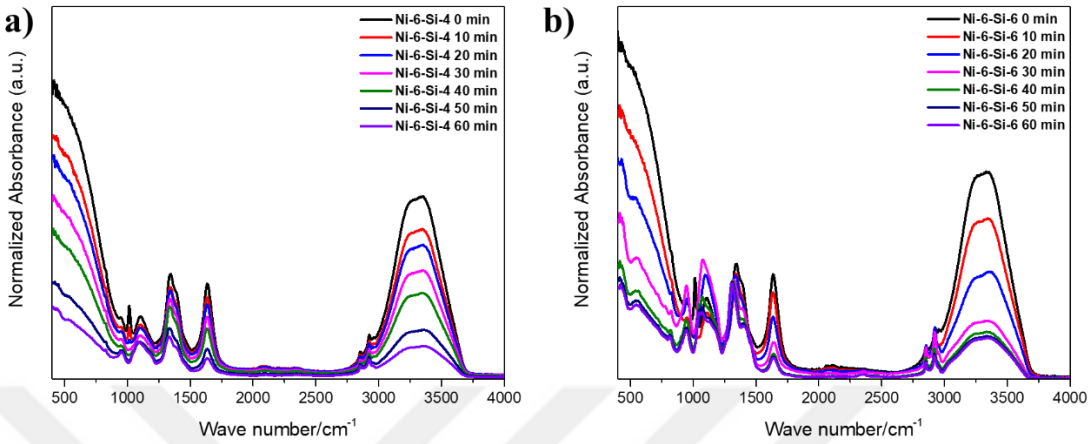

Figure 3.24. Time dependent ATR-FTIR spectra of a) Ni-6-Si-4 and b) Ni-6-Si-6 compositions.

3.2. Optimization of salt to silica ratio

For further studies, it was required to optimize the salt-to-silica ratio so that silica can retain the hexagonal fan texture of mesophase at higher temperatures. For this purpose, the salt mole ratio was increased to 10 Ni(II)/$C_{12}E_{10}$ and the silica to 4Si/$C_{12}E_{10}$. Due to high salt concentration, the salt leaches out of the mesophase very quickly at RT. Also, the solution is not stable at RT for a long time. The presence of acid in the solution enforces silica species to polymerize faster and makes it difficult for a large amount of salt to hold in the confined space after coating the solutions. Figure 3.25(a) shows the POM image of a freshly drop-casted Ni-10-Si-4 composition on a glass slide. Initially, no phase was observed between the crossed polarizers. However, Figure 3.26 shows the XRD patterns of the same composition over time and a broad diffraction line at 1.1°, 2θ, is observed, which means that the freshly coated sample has a cubic phase and appears dark under the POM.

However, on heating the coated sample in the POM heating stage, a fan texture of the hexagonal mesophase appears at 70 °C. Also in the XRD patterns, a broad diffraction line at 1.1°, 2θ, shifts to 1.7°, 2θ. It also proves that the cubic phase transforms to a hexagonal phase as the solvent evaporates leaving the salt species in the confined mesophase in a molten phase. On heating the hexagonal phase in the heating stage to 120 °C, the

hexagonal phase is retained, see Figure 3.25(c). In the hexagonal domains, a dark domain appears and grow with further increasing the temperature to 150 ^{o}C, see Figure 3.25.(d). The sample was then cooled to RT and further characterized by wide-angle XRD to analyze the newly formed dark domains. Figure 3.27(a) displays a set of time dependent XRD patterns, where the intense diffraction line at 1.7^{o}, 2θ, belongs to a 2D hexagonal phase. Also, a set of new diffraction lines appears at 10.7, 13.5, 16.5, 21.8, 25.09, and 44.7^{o}, 2θ, see Figure 3.27(b). This new set of diffraction lines belong to CTAB crystals as shown in Figure 3.27(b). Moreover, a piece of a sample from the glass slide that shows the dark grown domains was scratched and its ATR-FTIR was recorded. Figure 3.28 shows the ATR-FTIR spectrum of this scratched sample and display peaks related to hydroxide species, Which are most likely to be β-$Ni(OH)_2$ at high temperatures.

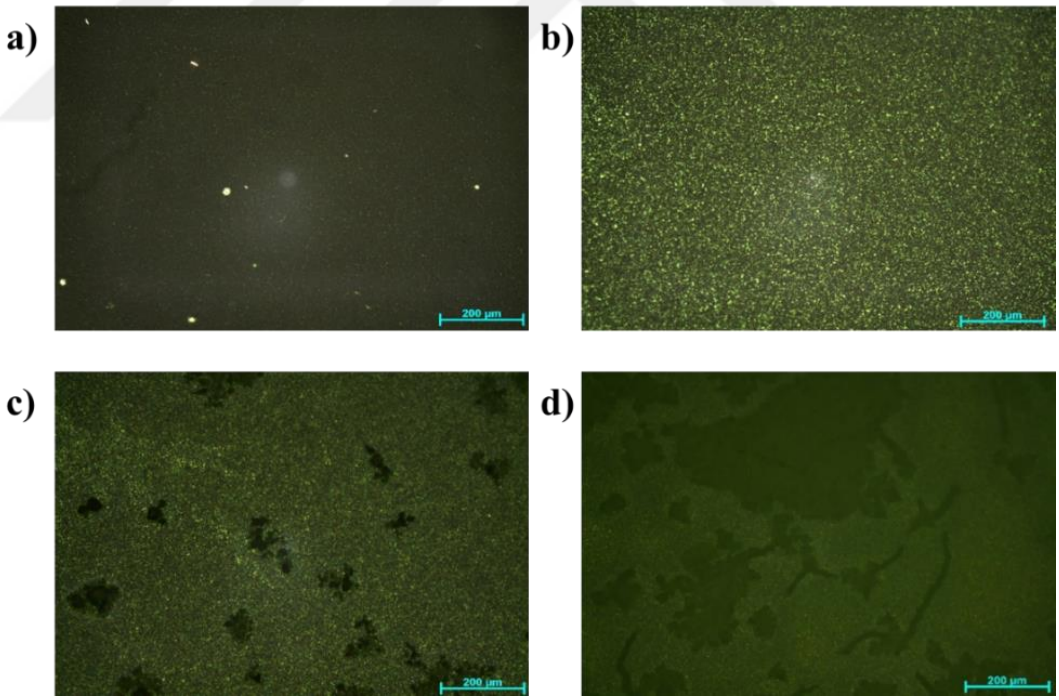

Figure 3.25. POM image of freshly drop-casted Ni-10-Si-4 composition at a) RT, b) 70 ^{o}C, c) 120 ^{o}C, and d) 150 ^{o}C.

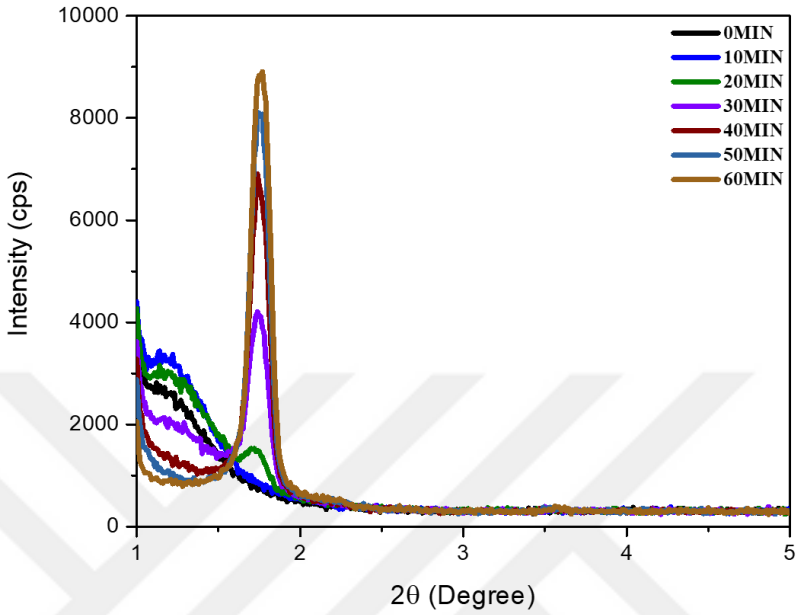

Figure 3.26. Small-angle XRD patterns of the Ni-10-Si-4 composition over the time.

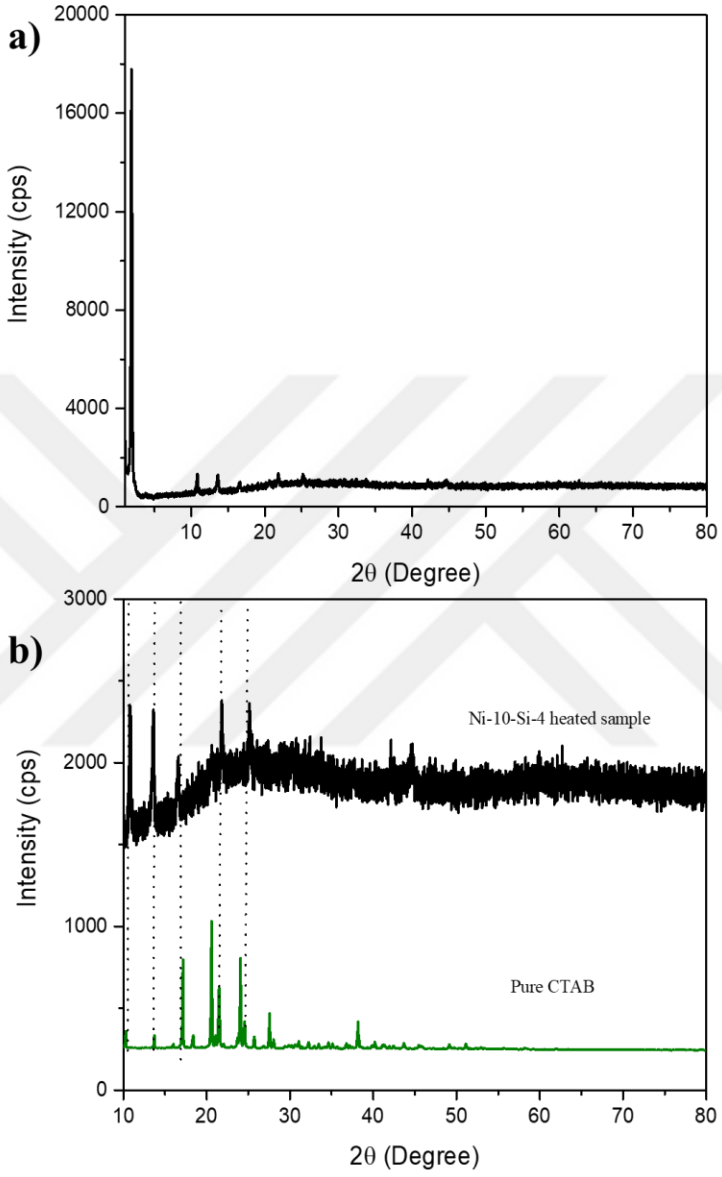

Figure 3.27. a) Wide-angle XRD pattern of the Ni-10-Si-4 composition after heating in the heating stage and b) zoom pattern of the same composition from 10 to 80º, 2θ, Ni-metal (PDF card no. 00-004-0850), Ni_2SO_4 (PDF card no. 01-074-0563), $Ni(OH)_2$ (PDF card no. 00-014-00117) and pure CTAB.

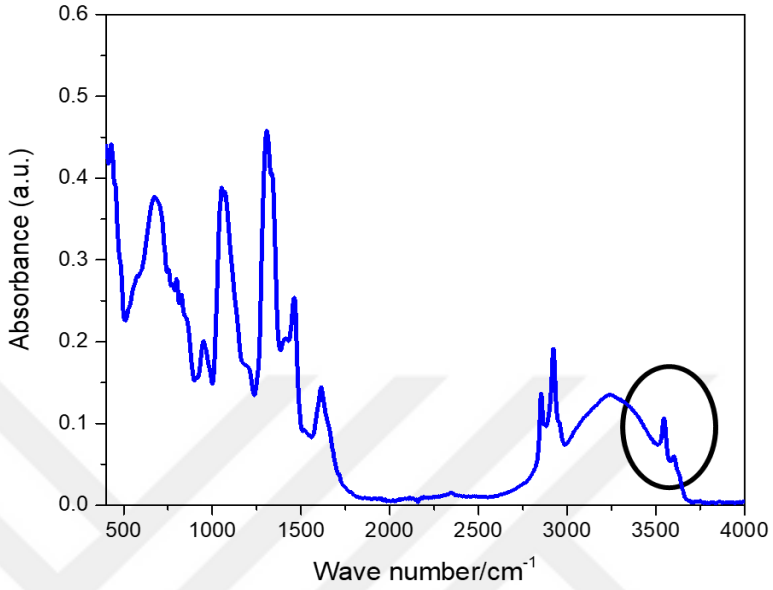

Figure 3.28. ATR-FTIR spectrum of Ni-10-Si-4, heated in the heating stage up to 150 ^{o}C.

The hexagonal fan texture remains even after one-day. However, under normal conditions at room temperature, the salt leaches out very quickly and makes this composition unstable. Therefore, it is noteworthy that heating the sample at a higher temperature makes it stable. Figure 3.29 shows the POM images of a one-day aged sample on the glass slide. The hexagonal texture is retained on one day aging and the dark domains are also stable. The ATR-FTIR spectra (Figure 3.30) of the scraped sample from the glass slide also confirm the stability of the hydroxide species.

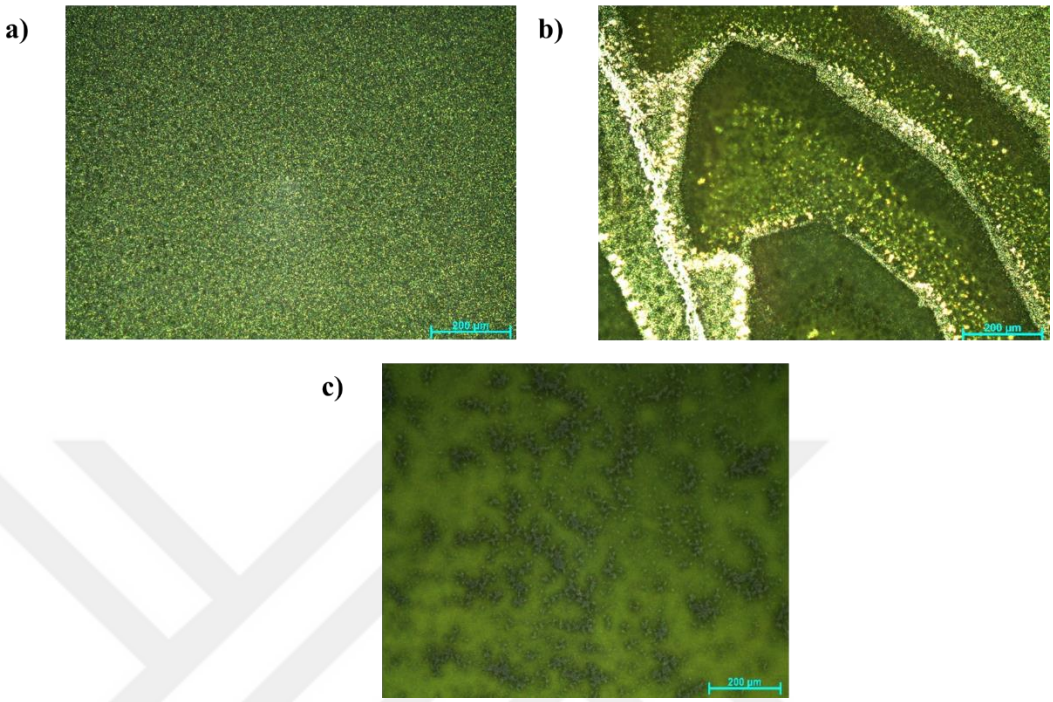

Figure 3.29. POM images of one-day aged Ni-10-Si-4 sample, heated in the heating stage.

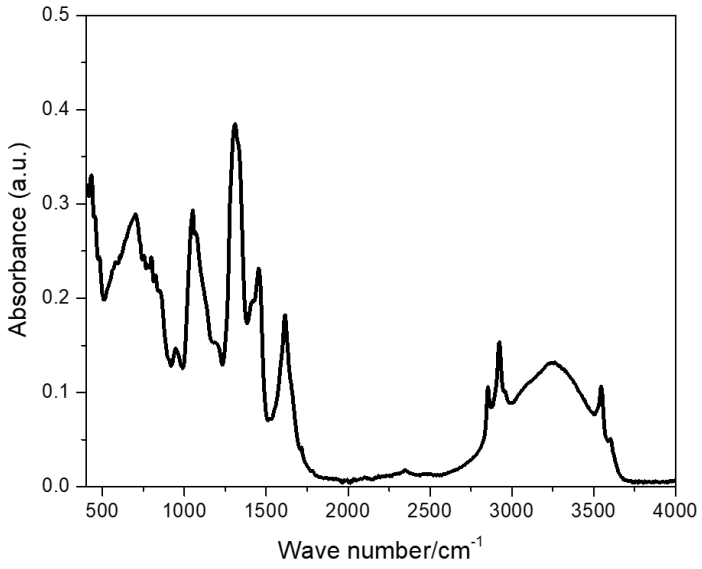

Figure 3.30. ATR-FTIR spectrum of one-day aged Ni-10-Si-4 sample.

More samples are prepared by further reducing the silica/surfactant ratio to 3 and keeping the Ni(II)/$C_{12}E_{10}$ mole ratio constant. The gel phase of Ni-10-Si-3 composition was characterized by small-angle XRD technique. The freshly drop-casted sample of this mole ratio doesn't show any diffraction line in first 10 minutes. The first diffraction line at 1.6^{o}, 2θ was observed after 15 min evaporation of the solvent, see Figure 3.31(a). Figure 3.31(b) displays the ATR-FTIR spectra over the time at 100 ^{o}C. Two drops of solution are put on the ATR-FTIR diamond crystal and covered with a cover glass. This sample shows a typical gel phase behavior on heating where on evaporation of solvent the nitrates are removed in the form of nitric acid and the free nitrate peak splits into two peaks due to coordination to Ni(II).

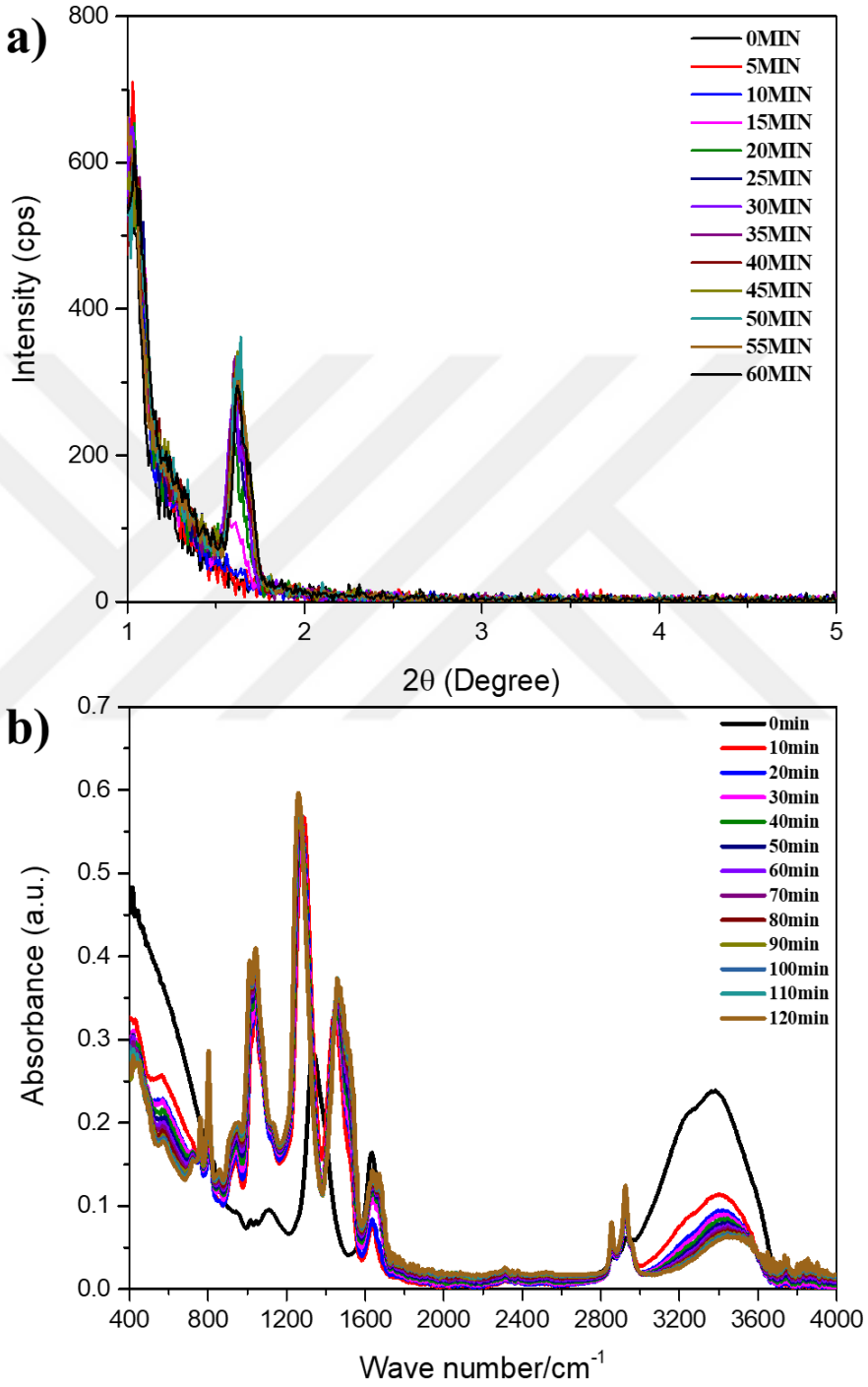

Figure 3.31. a) XRD patterns of Ni-10-Si-3 gel phase over the time and b) ATR-FTIR spectra of freshly prepared Ni-10-Si-3 composition over the time at 100 ^{o}C.

However, the normalized spectra (Figure 3.32. (a)) of this sample at 0 minutes and 120 minutes show that almost more than half of the nitrates have been removed in the form of HNO_3 during heating and the area under the curve of nitrate peaks at 0 minutes and 120 minutes confirms this loss of nitrates (Figure 3.32.(b)). It can also be noted that nearly half of the nitrates present in the sample are coordinated to Ni(II). This sample was aged for one day on the ATR-FTIR diamond crystal and spectra were recorded again at 100 ^oC after aging. The aged sample shows the formation of the hydroxide species (see Figure 3.33 (a)) as observed in the 10-Ni-Si-4 sample.

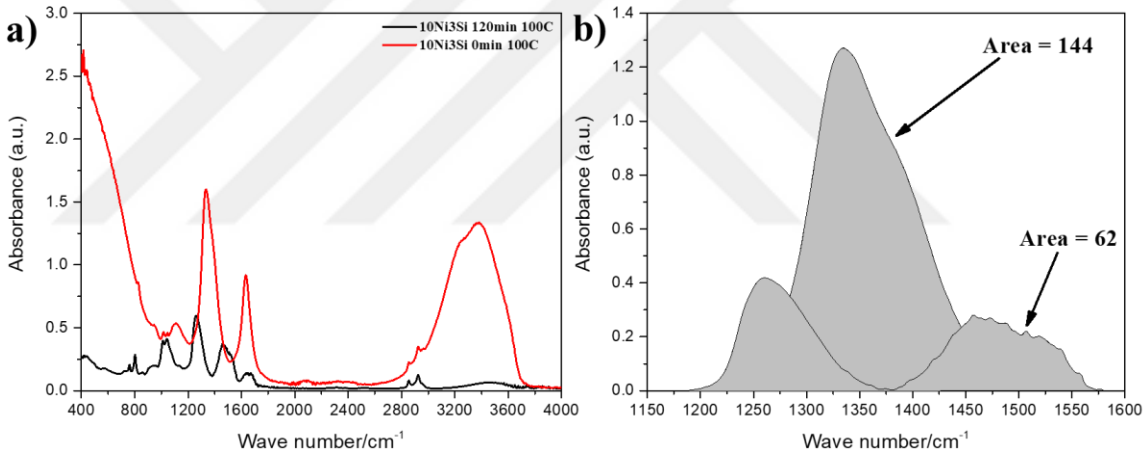

Figure 3.32. a) ATR-FTIR spectra of Ni-10-Si-3 at 100 ^oC and b) nitrate region and the area under the curve of the nitrate peaks before and after heating the sample.

Figure 3.33(a) shows the humidity-controlled ATR-FTIR spectra of the same one-day-aged sample. For this measurement, a homemade humidity chamber around the sample and sample holder was designed and the humidity of the chamber was increased to 68 % by using a saturated solution of KI salt solution inside the chamber[99]. The preformed hydroxides are wetted in high humidity and as the humidity increases, the hydroxide peaks shift to lower energy and get broader (Figure 3.33(b)). Moreover, the nitrates are also further removed with the increase in humidity (Figure 3.33(b)).

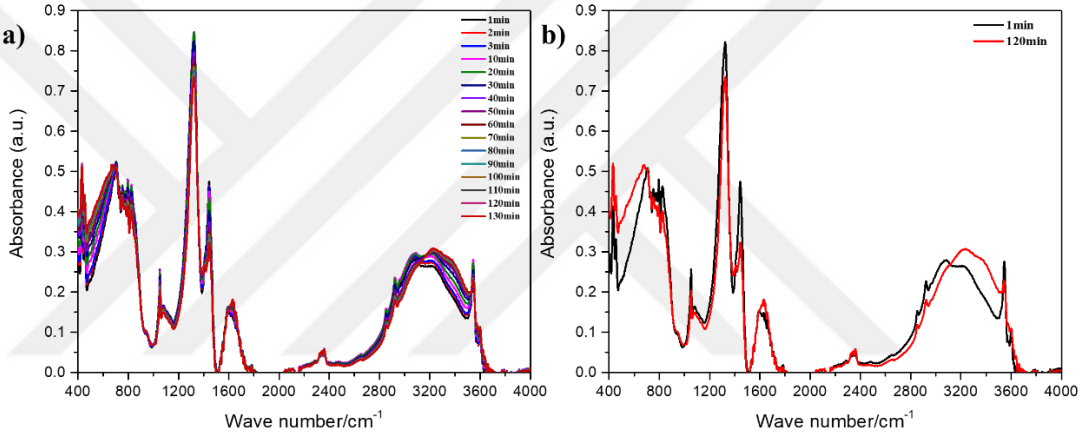

Figure 3.33. a) Humidity controlled ATR-FTIR spectra of one-day-aged Ni-10-Si-3 over the time (0 to 130 minutes) and b) the spectra of 0 minute and 120 minutes of the same composition.

Since both mole ratios (Ni-10-Si-4 and Ni-10-Si-3) display similar behavior, the samples with the low silica to salt mole ratio (Ni-10-Si-3) was chosen for the further characterization. The m-NiO/SiO_2 films were prepared by drop-casting the solution on the glass slides and then calcined at different temperatures (250 - 500 ^oC). Figure 3.34 shows the ATR-FTIR spectra of the calcined films. The surfactant peaks, at 2919 and 2849 cm^{-1} disappear, indicating that the surfactant burns out completely even at 250 ^oC. However, at around 1306 cm^{-1} a new peak appears due to formation of the surface bicarbonate species at 250 ^oC and these bicarbonate species transforms into carbonate species at higher temperatures. The carbonate species decomposes at higher annealing temperatures and their peaks almost disappear at 500 ^oC. Moreover, the peak at around 923 cm^{-1} due to Si-OH bending mode is sharper at 250 ^oC and it shows the presence of silanol sides or formation of nickel hydroxide in the sample. However, with the increase in annealing temperature this peak goes down and the Si-O-Si peak at 1026 cm^{-1} sharpens on reaching to 500 ^oC annealing temperature, indicating that the silanols are condensed into SiO_2 or nickel hydroxides crystallize into NiO.

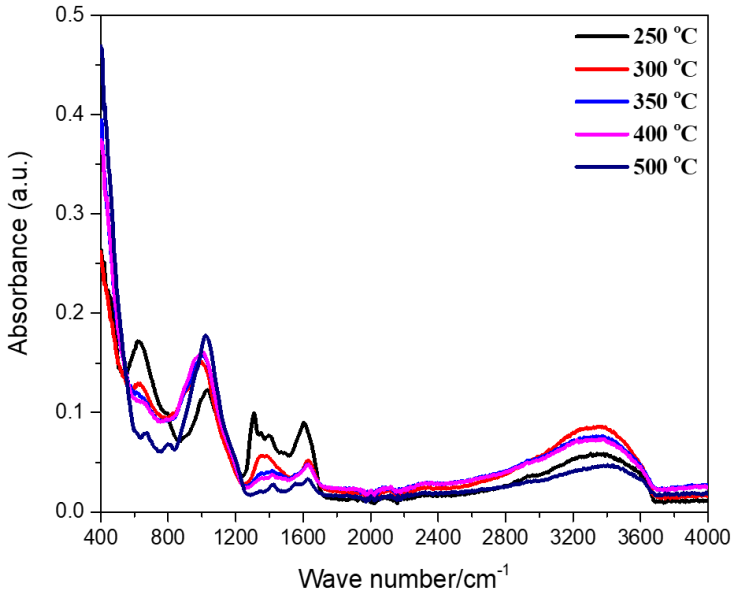

Figure 3.34. ATR-FTIR spectra of m-NiO/SiO_2 powders at different temperatures.

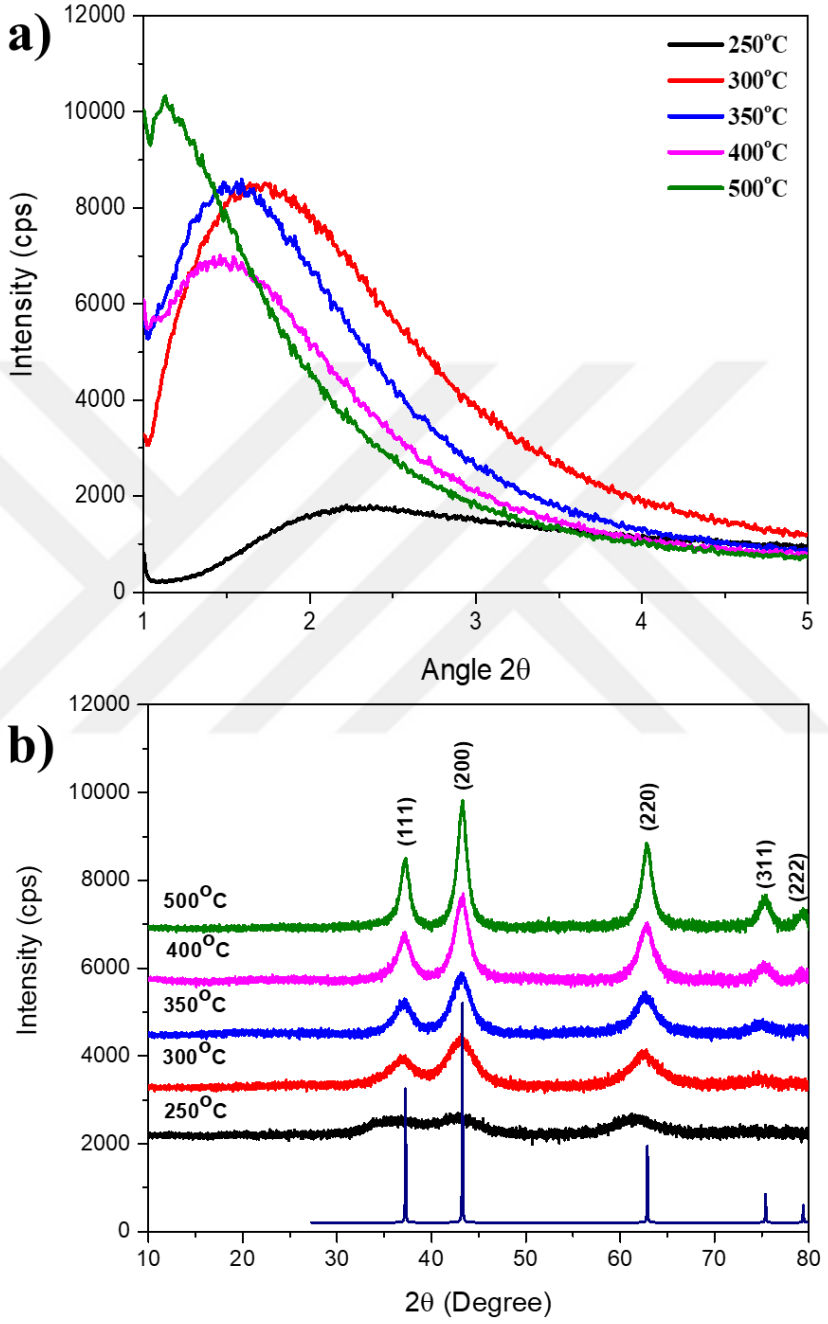

Figure 3.35. (a) The small-angle XRD patterns of m-NiO/SiO_2 at different temperatures and (b) wide-angle XRD patterns of m-NiO/SiO_2 at different temperatures.

Moreover, the small-angle XRD pattern (Figure 3.35.(a)) of the calcined films at 250 ºC shows a broad diffraction line at 2.25º, 2θ, and it does not only shift to the smaller angles by increasing the annealing temperature, it also gets narrower. The line narrowing and shifting continue by increasing the annealing temperature and it is observed at 1.12º, 2θ, at 500º C. This indicates that the particles grow (pore-walls) and cause an enlarging of the pores with increasing the annealing temperature. Also, the wide-angle XRD pattern (Figure 3.35(b)) of the calcined m-NiO/SiO_2 at 250 ºC shows five broad diffraction lines at 37, 43, 62, 75, and 79º, 2θ. These diffraction lines are indexed according to the ICDD data base (PDF card no: 00-047-1049 of face centered cubic rock-salt structure of NiO) and have been indexed to (111), (200), (220), (311), and (222) planes, respectively. However, no additional line from SiO_2 is observed and it means that the silica domains are amorphous and serves as a hard-template. The broad diffraction lines indicate that the formation of nano-crystalline material and sharpening of these diffraction lines at higher annealing temperatures shows the growth of the crystals. Size of the crystals are calculated by using the most intense diffraction line (200) at 43º, 2θ, with the help of Scherrer's equation. Table 3.1 summarizes the data for temperature dependent crystal-size. The particles, at 300 ºC, are on average 2.6 nm and increases by 3 times and becomes 7.9 nm at 500 ºC.

$D(nm) = \frac{K\lambda}{\beta cos\theta} = \frac{0.94 \times 0.154056}{FWHM\ cos\theta}$ Sample	Particle size (nm)
m-NiO/SiO_2-300	2.6
m-NiO/SiO_2-350	3.8
m-NiO/SiO_2-400	4.9
m-NiO/SiO_2-500	7.9

Table 3. 1.Particle size of m-NiO/SiO_2-XXX samples (XXX shows the calcination temperature (ºC).

The porosity of the m-NiO/SiO_2 films, at different calcination temperatures, is also determined by N_2-adsorption-desorption measurement. Figure 3.37 shows the N_2-adsorption-desorption isotherms and pore-size distribution plots of the m-NiO/SiO_2 at different annealing temperatures. All the samples display type IV isotherms at each calcination temperature, which is a characteristic of mesoporous materials. The isotherms and pore-size distribution data are summarized in Table 3.2.

Temperature (C)	BET Surface Area
250°C	**260 m^2/g**
300°C	**305 m^2/g**
350°C	**295m^2/g**
400°C	**253 m^2/g**
500°C	**174m^2/g**

Table 3. 2. Change in BET surface area with annealing temperature of m-NiO/SiO_2

As shown in the pore size distribution plots, the pore-size of the particle remains uniform at all calcination temperatures. However, the change in surface area of the sample shows that the particles are growing with increasing the annealing temperature and accord well with the XRD data. This also overrules the idea of expending the pores. Therefore, the shift in the small angles with increasing annealing temperature is due to the growth of the pore-walls (NiO) rather than pore-size. The surface area of the sample at 300 °C is 305 m^2/g and it drops only to 174 m^2/g at 500 °C. The decrease in surface is quite low as compared to the pure mesoporous NiO samples, prepared by our group without silica[78] . The pore-size distribution plots of the mesoporous NiO are also shown in Figure 3.37 for comparison purpose. However, the XRD patterns show that at higher temperatures the crystallinity of the samples increases. Therefore, it can be inferred from pore-size distribution plots and wide-angle XRD patterns of the samples that silica retards the growth of the NiO particles as well as pore-size in 3-dimensional space and allow the

particles to grow in 2-dimensional space keeping the pore size constant at all calcination temperatures; it is a lateral growth over silica pore-walls as shown in Figure 3.36.

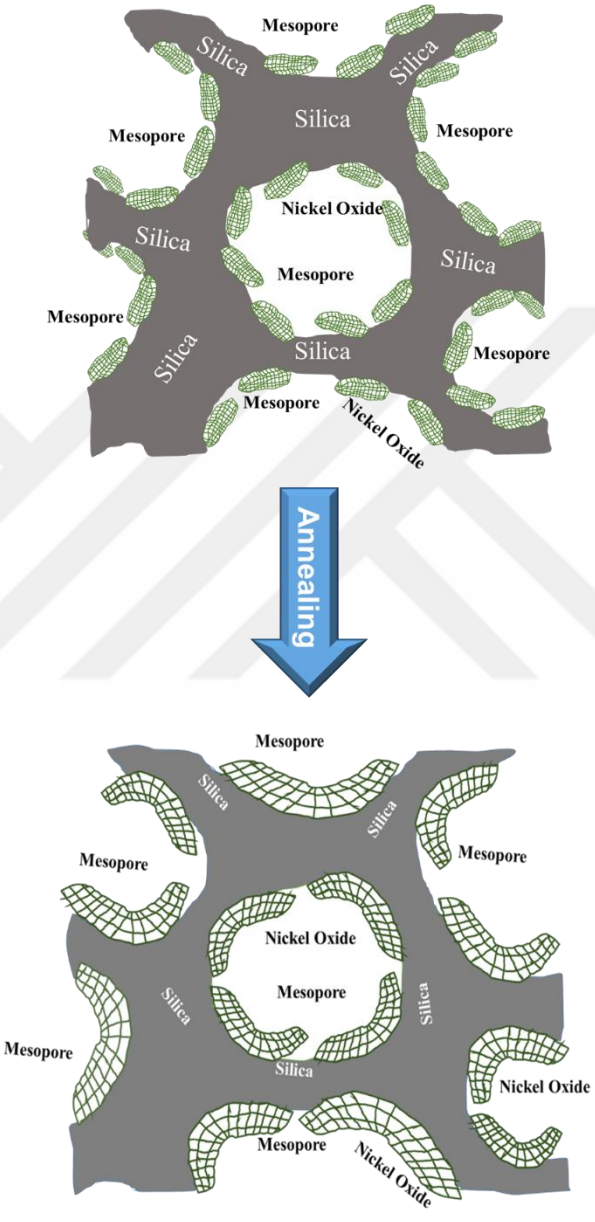

Figure 3.36. Schematic representation of NiO pore walls growth over silica pore-walls in m-NiO/SiO_2 films.

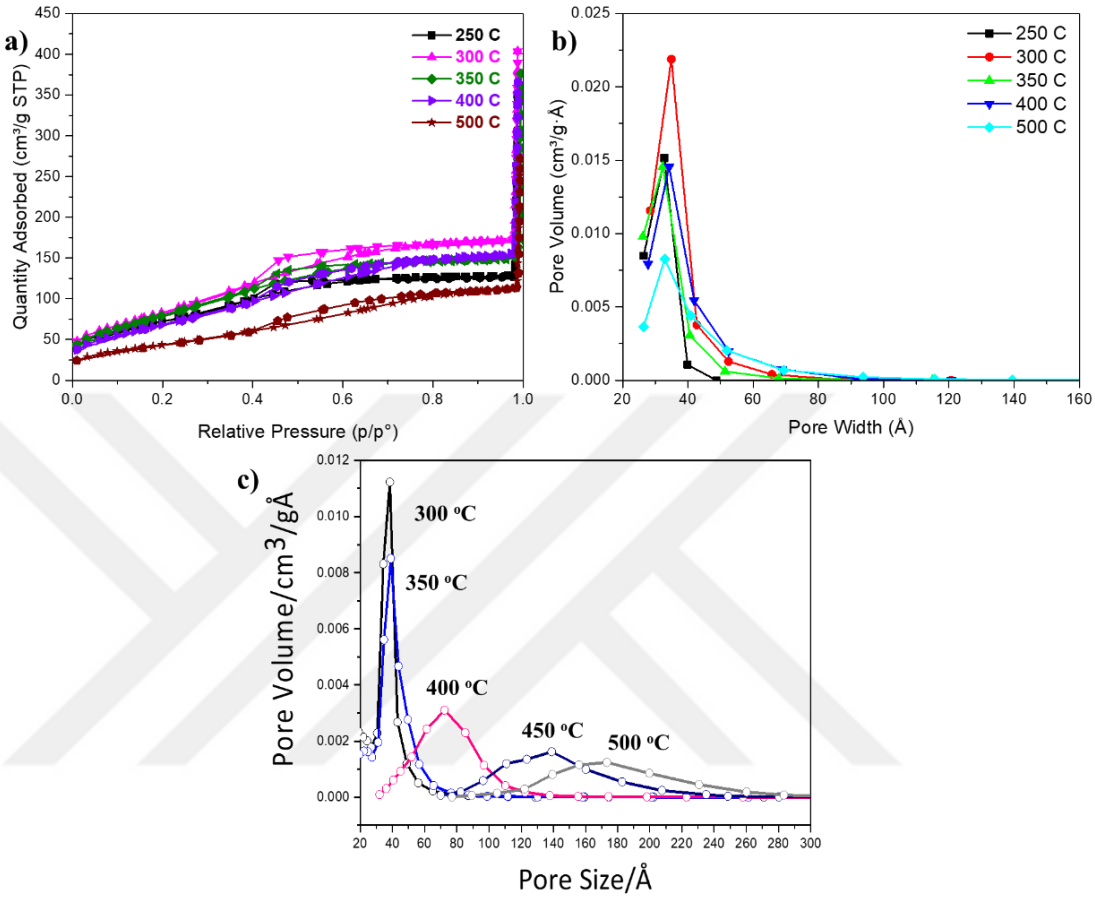

Figure 3.37. a) N_2 adsorption-desorption isotherms of the m-NiO/SiO_2 at different calcination temperatures, b) the pore-size distribution plots of the m-NiO/SiO_2 at different calcination temperatures, and c) the pore-distribution plots of the m-NiO at different temperatures.

Figure 3.38 shows the SEM images of the m-NiO/SiO_2 films, calcined at different temperatures and it shows that all the samples display a film morphology at all temperatures. The film morphology is retained even at high temperatures.

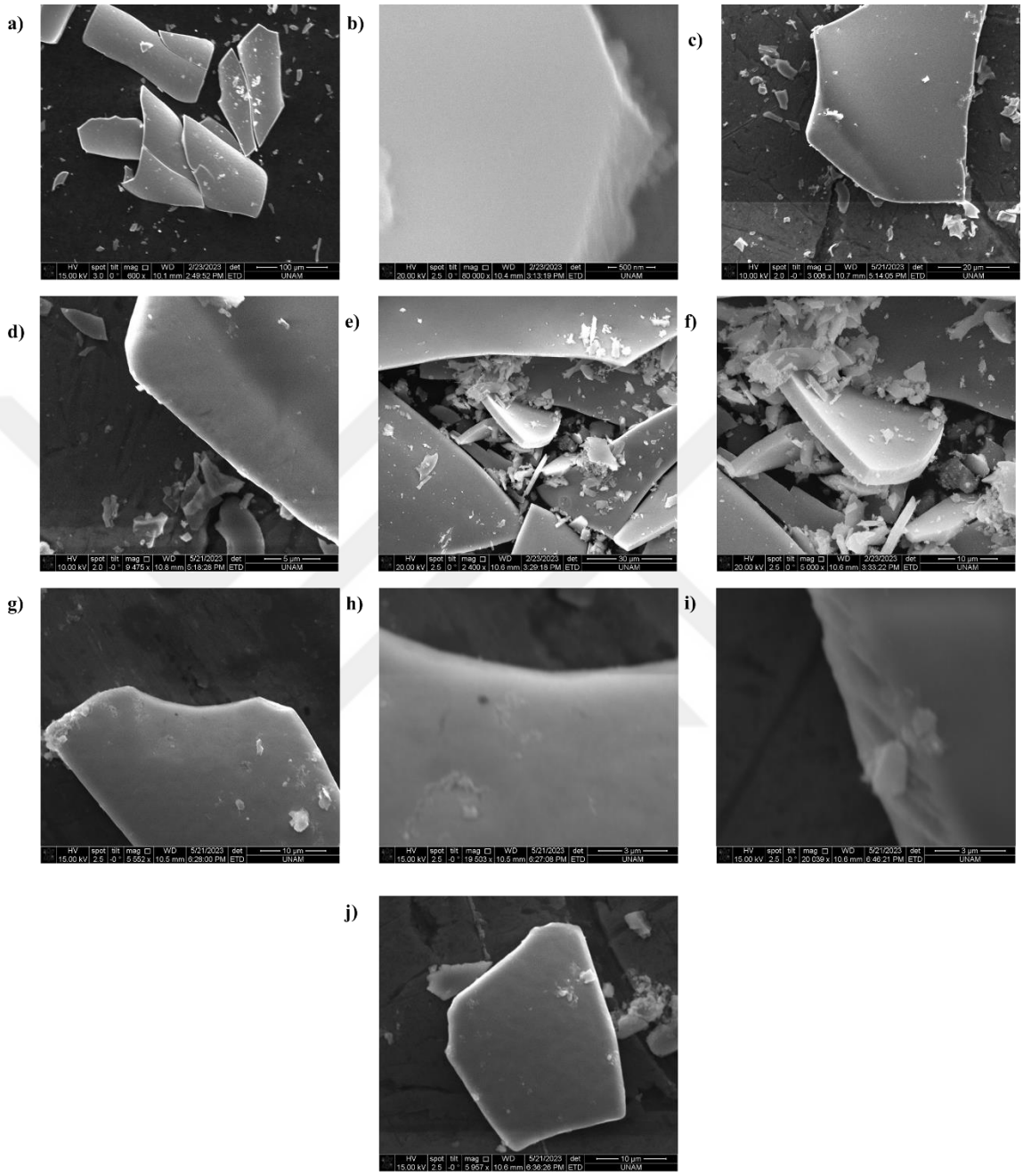

Figure 3.38. The SEM images of the a) m-NiO/SiO_2-300 (scale bar is 100µm), b) m-NiO/SiO_2-300 (scale bar is 500nm), c) m-NiO/SiO_2-350 (scale bar is 20µm), d) m-NiO/SiO_2-350 (scale bar is 5µm), e) m-NiO/SiO_2-350 (scale bar is 30µm), f) m-NiO/SiO_2-400 (scale bar is 10µm), g) m-NiO/SiO_2-400 (scale bar is 10µm), h) m-NiO/SiO_2-450 (scale bar is 3µm) , i) m-NiO/SiO_2-500 (scale bar is 3µm), and j) m-NiO/SiO_2-500 (scale bar is 10µm).

Chapter 4

4.1. Electrochemical characterization of the mesoporous NiO thin films

In order to further investigate the properties of m-NiO/SiO_2, electrochemical properties and performance of m-NiO/SiO_2 thin films as electrocatalyst for oxygen evolution reaction (OER) were studied. For these experiments, the clear solution of the Ni-10-Si-3 composition is spin coated on 1×2 cm FTO glass electrodes (half of the FTO 1×1 cm was coated) at 2000 rpm spin rate and calcined at different temperatures (250 to 500 ^{o}C) to produce the electrodes (denoted as m-NiO/SiO_2-10-XXX, XXX stands for the calcination temperature).

First, the cyclic voltammogram (CV) is recorded using a three-electrode cell (Pt wire as a counter electrode, Ag/AgCl as a reference electrode, our FTO coated electrode as the working electrode in 1 M KOH aqueous solution) in a -0.4 to 1.4 V potential window at a 50 mV/s scan rate. For each m-NiO/SiO_2-10-XXX electrode, 600 CVs were recorded under the same conditions except for the m-NiO/SiO_2-250, as only 250 CVs were recorded for this electrode.

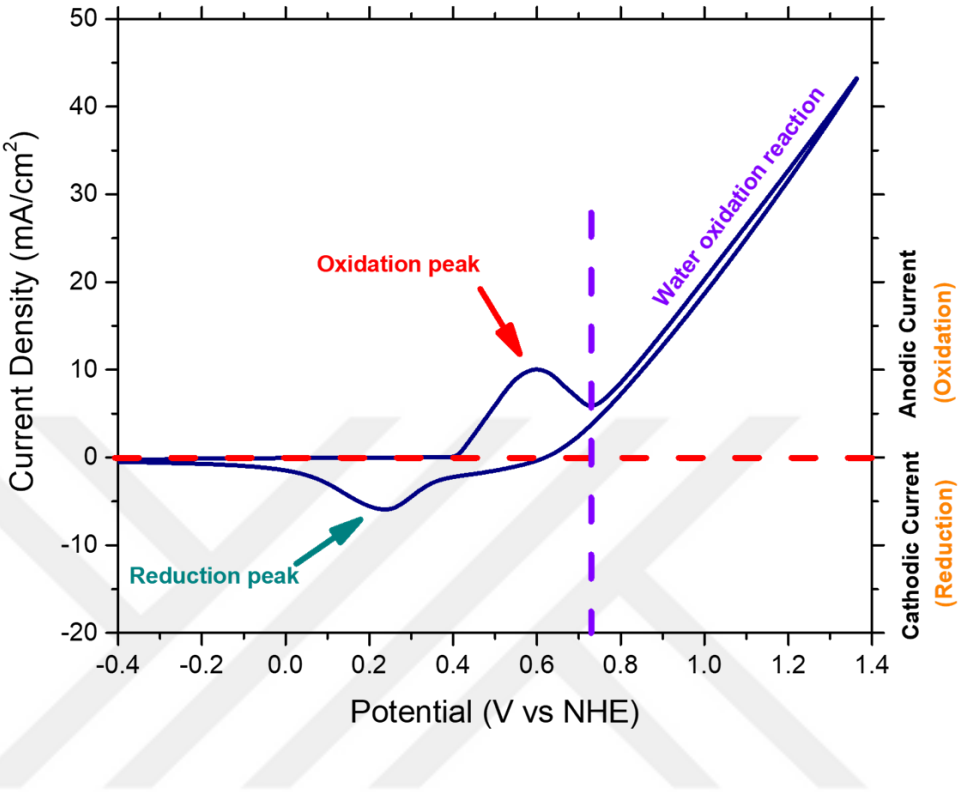

Figure 4.1. A typical cyclic voltammogram of m-NiO/SiO$_2$.

Figure 4.1 shows a general cyclic voltammogram of a m-NiO/SiO$_2$-XXX thin film. As per the IUPAC convention, the cyclic voltammogram is recorded as the potential sweeps from negative to positive voltage. The forward cycle gives the information about anodic current (oxidation) and it is positive while the reverse cycle gives the information about cathodic current (reduction) which is negative. The oxidation peak in the cyclic voltammogram represents the oxidation of Ni^{2+} to Ni^{3+} specie. While the reduction peak represents the reduction of Ni^{3+} to Ni^{2+} species. Moreover, it can be seen in the figure that at more positive potentials (over 0.7 V vs NHE), the current density increases sharply which indicates the onset of oxygen evolution reaction.

Figure 4.2 shows the 2nd and 600th CVs of the m-NiO/SiO$_2$ electrodes prepared at 300, 350, 400 and 500 ^{o}C. It can be observed in Figure 4.2 (a) that with the increase in annealing temperature the peak current is decreasing and a very small peak current is observed in case of the m-NiO/SiO$_2$-500 electrode. It shows that annealing temperature affects the

peak current. The m-NiO/SiO_2-300 electrode has a peak current of 3.5 mA/cm^2, while the m-NiO/SiO_2-500 electrode has a peak current of 0.5 mA/cm^2. This change in current density correlates with the change in surface area with the annealing temperature and increase in crystallinity. High surface area at lower temperature provides more active sides, therefore its current density is also high and it decreases with the decrease in surface area.

However, the current density also increases with cycling. Figure 4.3 shows the number of cycles vs peak current density of all the electrodes. The plot shows that the surface of the electrode changes with the increase in number of cycles since more m-NiO/SiO_2 surface is converted into $Ni(OH)_2$ (electrochemically more active than NiO) and it cannot be reduced back to NiO unless the electrodes reannealed.

Also, with the increase in crystallinity at higher temperatures, the stability of the electrodes also increases. The m-NiO/SiO_2-300 electrode is unstable as this temperature even though the m-NiO/SiO_2 forms but it does not adhere to the FTO glass surface. It can be seen from Figure 4.3 that the current density decreases after certain number of cycles and then drops to zero. The m-NiO/SiO_2-300 electrode displays a 12 mA/cm^2 current density in first 40 cycles and on further cycling the current density almost reaches to zero which shows that the electrode is unstable over the FTO surface. This happens due to the presence of silica template which etches out in the presence of KOH. However, the m-NiO/SiO_2-500 electrode shows an increase in the current density up to 7 mA/cm^2 in 350 cycles and decreases to 6 mA/cm^2 in 600^{th} cycle. The initially low current density of this electrode is due to the low BET surface area at 500 ^oC and larger pore walls. The CVs of all the electrodes up to 600 cycles are also shown in Figure 4.4.

Additionally, no oxidation peak from NiO was observed at around 0 V, which shows that NiO is covered with silica during calcination process.

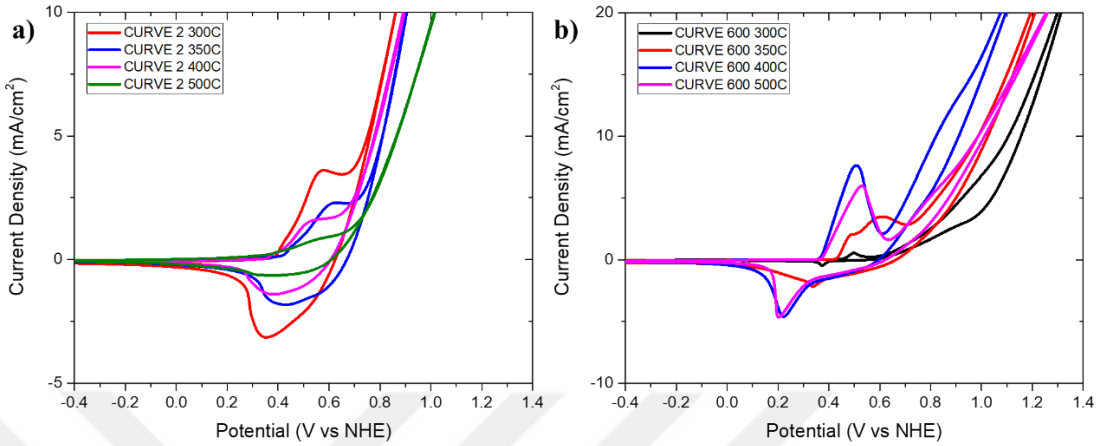

Figure 4 2. a) The 2nd cycle of m-NiO-SiO2-300, m-NiO-SiO2-350, m-NiO-SiO2-400, and m-NiO-SiO2-500 and b) 600th cycle of m-NiO-SiO2-300, m-NiO-SiO2-350, m-NiO-SiO2-400, and m-NiO-SiO2-500.

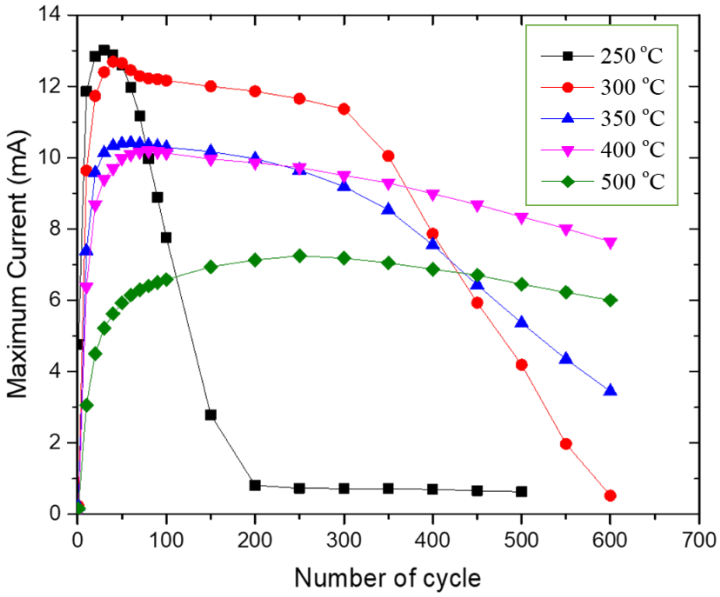

Figure 4.3. Number of cycles vs maximum current density (mA/cm2) plot of the m-NiO-SiO2-250, m-NiO-SiO2-300, m-NiO-SiO2-350, m-NiO-SiO2-400, and m-NiO-SiO2-500 electrodes.

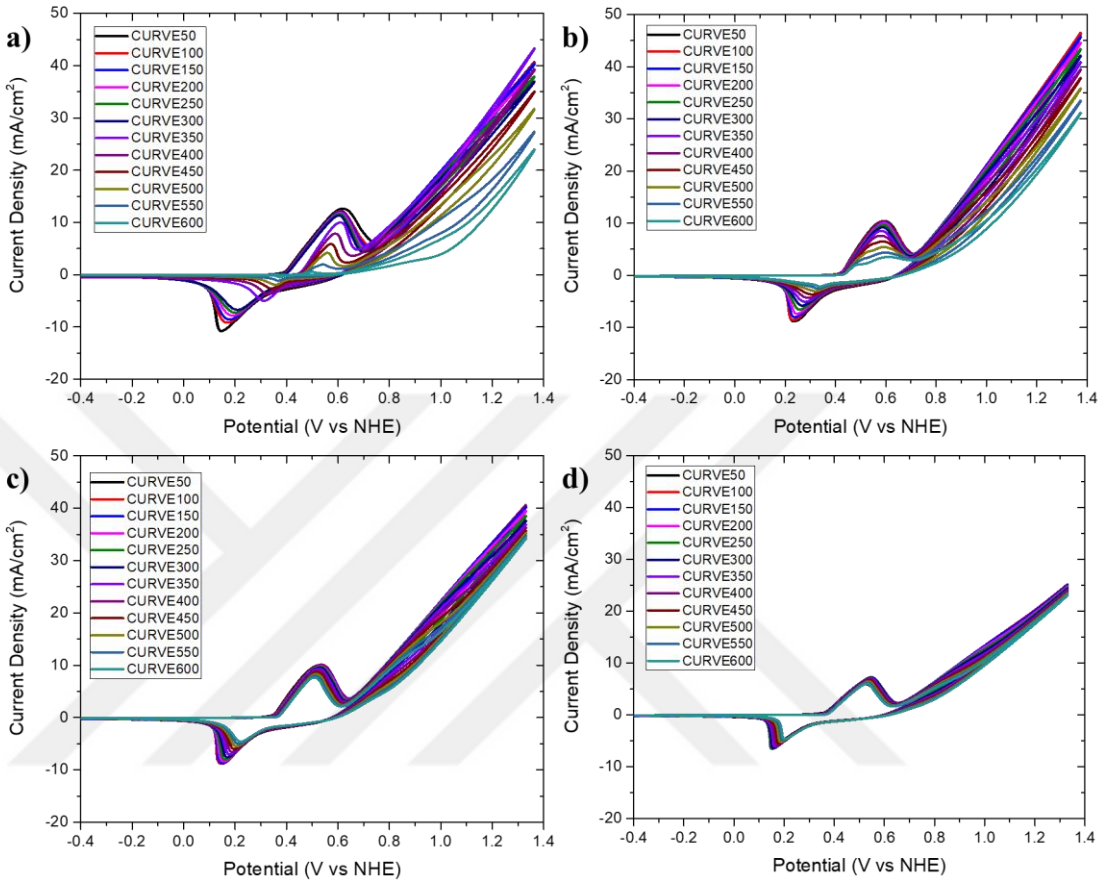

Figure 4.4. 600 CVs of the a) m-NiO-SiO_2-300 b) m-NiO-SiO_2-350 c) m-NiO-SiO_2-400 and d) m-NiO-SiO_2-500 electrodes.

Figure 4.5(a) shows the 500 CVs of the m-NiO/SiO_2-250 electrode and change in peak current density with the increase in number of cycles. Figure 4.5(b) shows that this electrode shows the initial peak current density of almost 5 mA/cm^2 (higher than all the other electrodes) the maximum peak current density of 13 mA/cm^2 in first 30 cycles is observed and then it decreases sharply to almost 0 mA/cm^2 in the 200th cycle. This is also due to the stability of the electrode and less crystalline sample (as shown in the XRD pattern of the material at this temperature in the previous section). Maximum current density should also correlate with the BET surface area analysis but surface area analysis shows that the surface at 250 ^oC is less even than 300 ^oC. This increase in initial peak current density and the maximum current density shows that all the material is not m-

NiO/SiO_2, some amount of $Ni(OH)_2$ is also present (electrochemically more active material) and with cycling the m-NiO/SiO_2 is also partially converted into $Ni(OH)_2$.

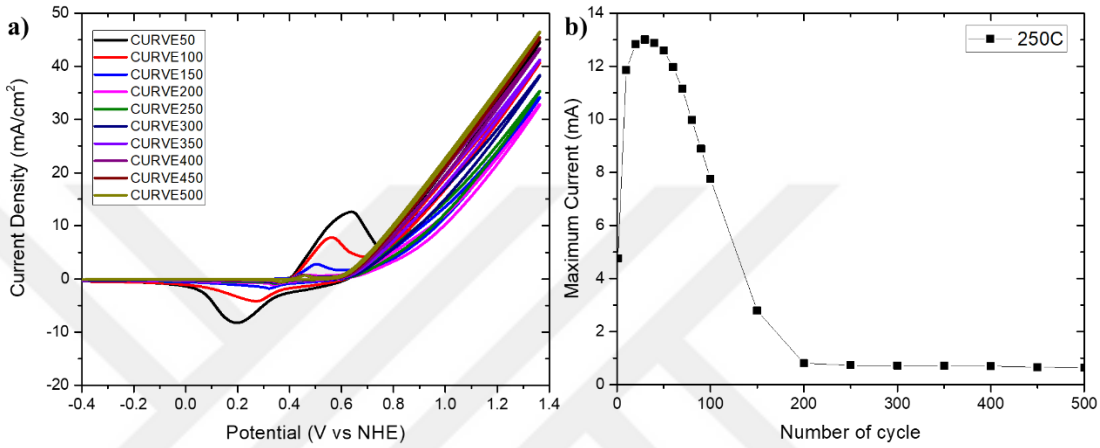

Figure 4.5. a) CVs and b) the plot of number of cycle vs maximum current density (mA/cm^2) from each CV in panel (a) of the m-NiO-SiO_2-250 electrode.

Overpotentials values were also determined for the Ni-10-Si-3-XXX electrodes by conducting chronopotentiometry experiments. Figures 4.6(a) & (b) show the overpotentials of values at 1 mA and 10 mA current densities, respectively. At 1 mA current density, all the electrodes are showing better performance with the time and their over potential values decrease. All the values lie in the range of 266 to 326 mV. The Ni-10-Si-3-300 electrode shows the least over potential value of 266 mV. However, at 10 mA/cm^2 current density, all the electrodes are stable and display good performance except the Ni-10-Si-3-500 electrode, which is likely due to silica resistance at higher temperature. At 10 mA/cm^2 current density, the Ni-10-Si-3-400 electrodes show the best performance with the least over potential value of 455 mV.

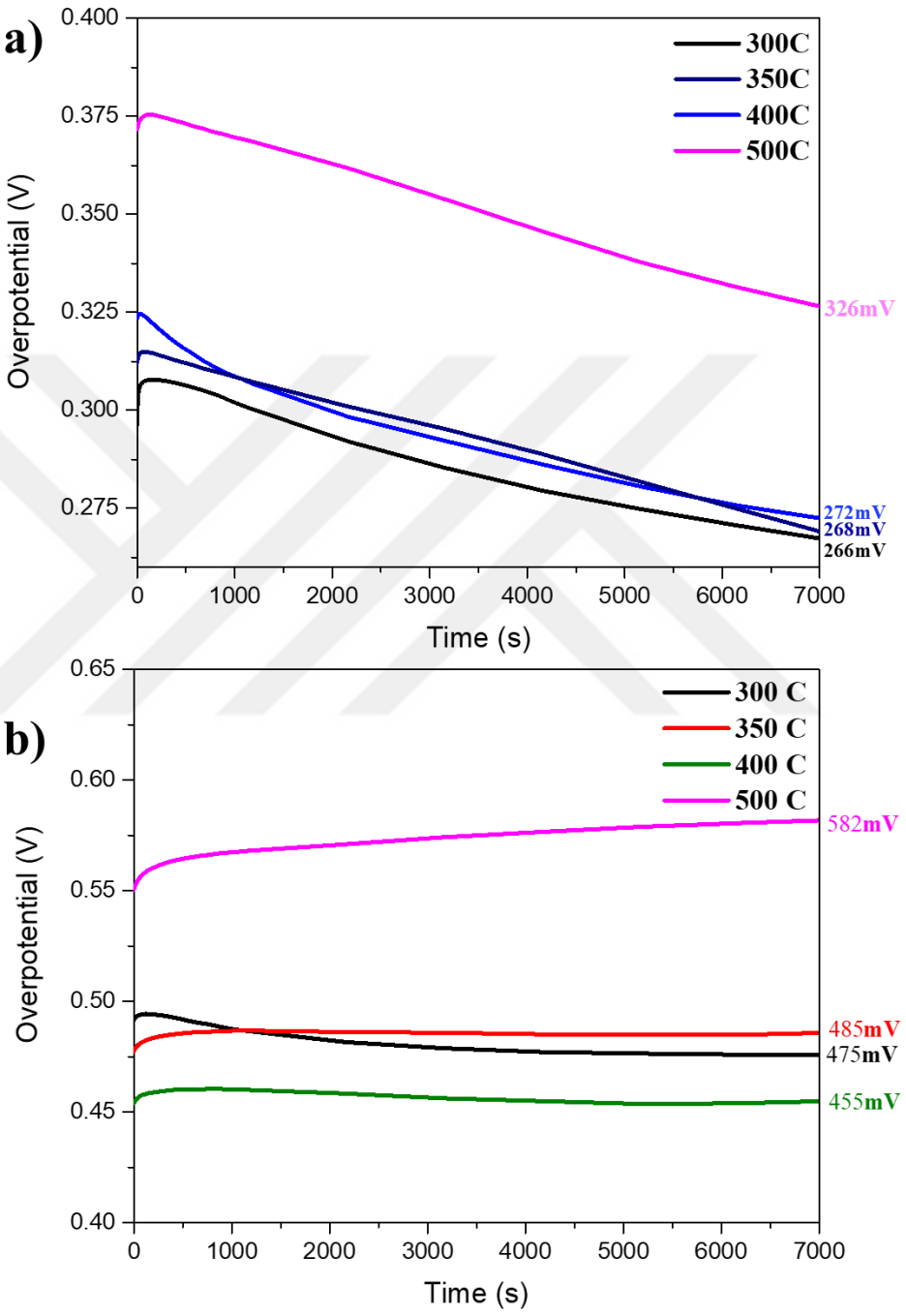

Figure 4. 6. Chronopotentiometry results of the Ni-10-Si-3-XXX electrodes at (a) 1 mA/cm^2 current density and (b) 10 mA/cm^2 current density.

4.2. Thickness dependent measurements

Figure 4.7 shows the thickness dependent CVs of the m-NiO/SiO_2-300 electrodes, initially coated at 2000, 3000, 4000 and 5000 rpms. It can be seen from the number of cycles vs maximum current density plot (Figure 4.6. (b)) that all the electrodes are stable up to 50 cycles. However, the decrease in current density in the 50^{th} cycle corresponds to a decrease in amount of sample with the increase in spin rate. It shows that only top surface of the material is involved in the electrochemical process and the material underneath the top surface doesn't take part in the process. Moreover, the electrodes prepared at 4000 and 5000 rpm are behaving similarly as the change in current density with the cycling is similar. Therefore, it shows that the electrodes are stable in the first 50 cycles irrespective of the thickness of the material.

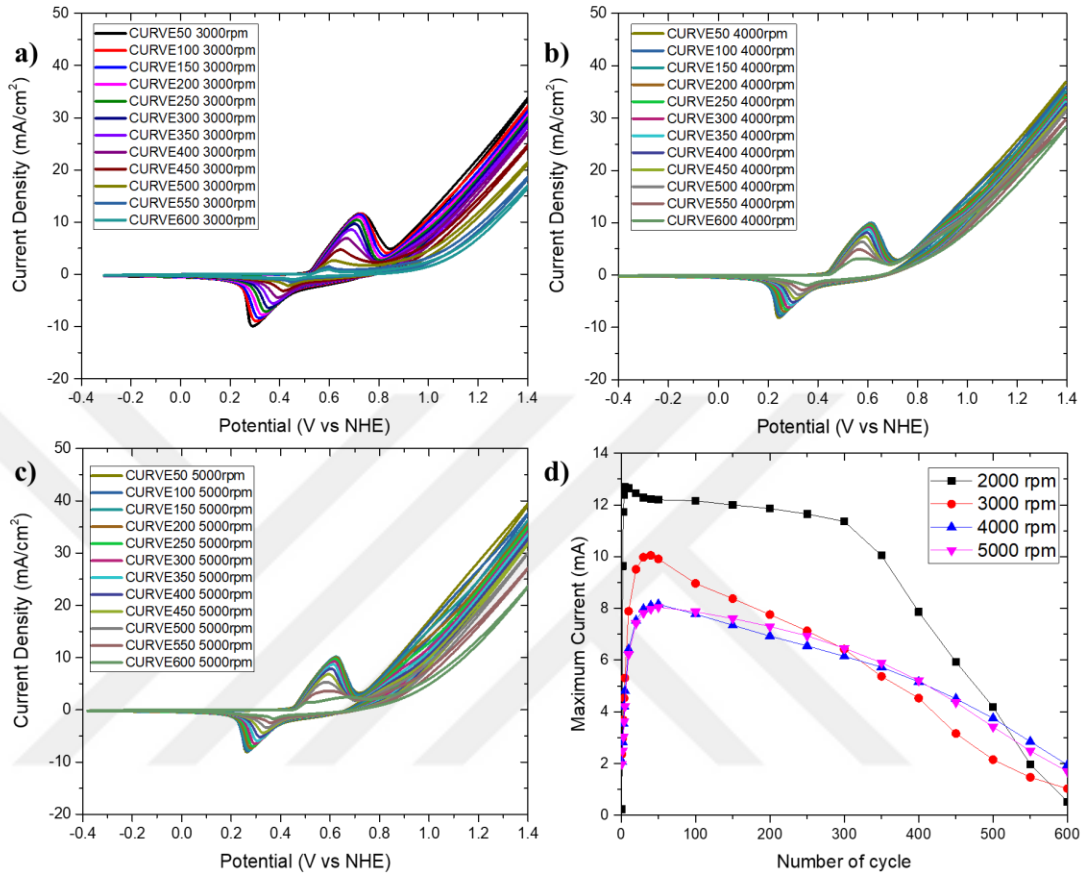

Figure 4.7. 600 CVs of the m-NiO-SiO_2-300 electrodes, prepared at a) 3000 rpm b) 4000 rpm, and c) 5000 rpm. (d) Plot of cycle number vs maximum current density.

Chapter 5

5.1. Conclusion

This thesis explores the synthesis of mesoporous nickel oxide thin films through the combined utilization of soft (MASA) and hard (silica) template methods. The formation of a homogeneous solution containing transition metal salt, surfactant, and TMOS (tetramethyl orthosilicate) is dependent on the presence of nitric acid, which stabilizes the solution. In the absence of nitric acid, the transition metal salts acts as a catalyst, initiating the hydrolysis and condensation of TMOS, resulting in the formation of silica. Once the silica is separated from the salt solution, the supernatant can be reused multiple times for the synthesis of additional batches of silica by simply adding surfactants and TMOS. The silica precipitates exhibit wide-angle diffraction, indicating the presence of amorphous silica. Additionally, the surface area of the silica is influenced by the choice of transition metal. Upon calcination at 450°C for two hours, the highest surface area observed is 1395 m2/g when cobalt(II) salt is employed. Energy-dispersive X-ray spectroscopy (EDX) analysis verifies the absence of any precipitated metal within this material. This method offers a convenient approach to silica synthesis, as it obviates the need for high temperatures to remove the surfactants.

The stable homogeneous solution comprising of salt, surfactants, nitric acid, and TMOS (tetramethyl orthosilicate) can be applied onto a glass substrate through drop casting for subsequent characterization. Solutions containing lower TMOS concentrations exhibit

stability for several days, whereas the stability decreases as the TMOS concentration in the solution increases. The solution with the highest TMOS concentration remains stable for approximately 6 hours. Upon freshly coating the samples onto the glass surface, low-angle diffraction patterns are observed, indicating the presence of mesophases. These mesophases, characterized by high silica concentrations, gradually form over time and initially appear dark when observed between crossed polarizers using polarized optical microscopy (POM). At this stage, no diffraction at low angles is observed. Subsequently, these mesophases transform into a hexagonal phase, displaying a fan-like texture when viewed between crossed polarizers, along with low-angle diffraction. During heating in a heating stage, TMOS undergoes polymerization to form silica within these mesophases, while still retaining the fan-like texture. In the presence of high TMOS concentrations, the salt leaches out at room temperature. Therefore, it is imperative to promptly calcine these samples after mesophase formation to generate mesoporous metal oxides.

Upon calcination of the mesophases at elevated temperatures, mesoporous nickel oxide is synthesized, initially exhibiting a high surface area at 300°C and a uniform distribution of pore sizes. As the material undergoes annealing at higher temperatures, the pore walls grow, resulting in a reduction of the material's surface area. However, due to the presence of a silica template, the pore size remains unchanged, indicating that the growth of pore walls occurs in a two-dimensional space rather than three-dimensional, thus maintaining the pore size constant. This lateral expansion of the pores ensures the synthesis of a crystalline material with a high surface area. Remarkably, the surface area achieved through this method is approximately eight times greater compared to the material synthesized solely using the soft templating method. This approach guarantees the production of materials with controlled pore sizes and crystalline pore walls at elevated temperatures, rendering them suitable for a variety of applications. During cyclic voltammetry, the pore walls of the nickel oxide undergo conversion to NiOOH during oxidation and to $Ni(OH)_2$ during reduction. It is noteworthy that the material does not revert back to nickel oxide, leading to the transformation of some layers of the material into $Ni(OH)_2$.

References:

[1] L. B. McCusker, F. Liebau, and G. Engelhardt, “Nomenclature of structural and compositional characteristics of ordered microporous and mesoporous materials with inorganic hosts: (IUPAC recommendations 2001),” *Pure Appl. Chem.*, vol. 73, no. 2, pp. 381–394, 2001, doi: 10.1351/pac200173020381.

[2] P. A. Jacobs, E. S. P. B. V, and M. Kojima, “Zeolites: Facts, Figures, Future,” in *Zeolites: Facts, Figures, Future*, no. 1, B. P.A. Jacobs - K.U. Leuven, Leuven and T. N. R.A. van Santen - T.U. Eindhoven, Eindhoven, Eds. 1989, pp. 1223–1231.

[3] P. Demontis and G. B. Suffritti, “Structure and dynamics of zeolites investigated by molecular dynamics,” *Chem. Rev.*, vol. 97, no. 8, pp. 2845–2878, 1997, doi: 10.1021/cr950253o.

[4] T. Armbruster and M. E. Gunter, “Crystal structures of natural zeolites,” *Rev. Miner. Geochem.*, vol. 45, pp. 1–67, 2001, doi: 10.2138/rmg.2001.45.1.

[5] V. I. Isaeva, K. E. Papathanasiou, and L. M. Kustov, “Zeolite-Like Boron Imidazolate Frameworks (BIFs): Synthesis and Application,” vol. volume 10, no. issue 7, 2020, doi: 10.3390/cryst10070617.

[6] A. Corma, V. Fornes, S. B. Pergher, T. L. M. Maesen, and J. G. Buglass, “Delaminated zeolite precursors as selective acidic catalysts,” *Nature*, vol. 396, no. 6709, pp. 353–356, 1998, doi: 10.1038/24592.

[7] T. T. Moore and W. J. Koros, “Non-ideal effects in organic-inorganic materials for gas separation membranes,” *J. Mol. Struct.*, vol. 739, no. 1–3, pp. 87–98, 2005, doi: 10.1016/j.molstruc.2004.05.043.

[8] K. Egeblad, C. H. Christensen, M. Kustova, and C. H. Christensen, “Templating mesoporous zeolites,” *Chem. Mater.*, vol. 20, no. 3, pp. 946–960, 2008, doi: 10.1021/cm702224p.

[9] M. E. Davis, “Ordered porous materials for emerging applications,” *Nature*, vol. 417, no. 6891, pp. 813–821, 2002, doi: 10.1038/nature00785.

[10] D. H. Everett and L. Butterworths, “MANUAL OF SYMBOLS AND TERMINOLOGY FOR PHYSICOCHEMICAL QUANTITIES AND UNITS APPENDIX,” *Pure Appl. Chem.*, vol. 31, no. July, pp. 579–638, 1972, [Online]. Available: https://doi.org/10.1351/pac197231040577.

[11] C. T. Kresge, M. E. Leonowicz, W. J. Roth, J. C. Vartuli, and J. S. Beck, “Ordered mesoporous molecular sieves synthesized by a liquid-crystal template mechanism,” *Nature*, vol. 359, pp. 710–712, 1992.

[12] A. Sayari and P. Liu, “Non-silica periodic mesostructured materials: Recent progress,” *Micropor. Mater.*, vol. 12, no. 4–6, pp. 149–177, 1997, doi: 10.1016/S0927-6513(97)00059-X.

[13] J. S. Beck, J. C. Vartuli, W. J. Roth, M. E. Leonowicz, C. T. Kresge, K. D. Schmitt, C. T-W. Chu, D. H. Olson, E. W. Sheppard, S. B. McCullen, J. B. Higgins and J. L. Schlenker, “A New Family of Mesoporous Molecular Sieves Prepared with Liquid Crystal Templates,” *J. Am. Chem. Soc.*, vol. 114, no. 27, pp. 10834–10843, 1992, doi: 10.1021/ja00053a020.

[14] S. A. Bagshaw, E. Prouzet, and T. J. Pinnavaia, “Templating of mesoporous molecular sieves by nonionic polyethylene oxide surfactants,” *Science (80-.).*, vol. 269, no. 5228, pp. 1242–1244, 1995, doi: 10.1126/science.269.5228.1242.

[15] G. S. Attard, J. C. Glyde, and C. G. Göltner, “Liquid-crystalline phases as templates for the synthesis of mesoporous silica,” *Nature*, vol. 378, pp. 366–368, 1995, doi: 10.1038/378366a0.

[16] W. Yue and W. Zhou, “Crystalline mesoporous metal oxide,” *Prog. Nat. Sci.*, pp. 1329–1338, 2008, doi: 10.1016/j.pnsc.2008.05.010.

[17] A. Taguchi and F. Schüth, “Ordered mesoporous materials in catalysis,” *Micro. Meso. Mater.*, vol. 77, no. 1, pp. 1–45, 2005, doi: 10.1016/j.micromeso.2004.06.030.

[18] D. Gu and F. Schüth, “Synthesis of non-siliceous mesoporous oxides,” *Chem. Soc. Rev.*, vol. 43, no. 1, pp. 313–344, 2014, doi: 10.1039/c3cs60155b.

[19] Y. Ren, Z. Ma, and P. G. Bruce, “Ordered mesoporous metal oxides: Synthesis and applications,” *Chem. Soc. Rev.*, vol. 41, no. 14, pp. 4909–4927, 2012, doi: 10.1039/c2cs35086f.

[20] P. Yang, D. Zhao, D. I. Margolese, B. F. Chmelka, and G. D. Stucky, “Generalized syntheses of large-pore mesoporous metal oxides with semicrystalline frameworks,” *Nature*, vol. 396, pp. 152–155, 1998, doi: 10.1038/24132.

[21] P. Yang, D. Zhao, D. I. Margolese, B. F. Chmelka, and G. D. Stucky, “Block copolymer templating syntheses of mesoporous metal oxides with large ordering lengths and semicrystalline framework,” *Chem. Mater.*, vol. 11, no. 10, pp. 2813–2826, 1999, doi: 10.1021/cm990185c.

[22] L. Guo, H. Arafune, and N. Teramae, “Synthesis of mesoporous metal oxide by the thermal decomposition of oxalate precursor,” *Langmuir*, vol. 29, no. 13, pp. 4404–4412, 2013, doi: 10.1021/la400323f.

[23] B. F. Monnier, A. Schüth, F. Huo, Q. Kumar, D. Margolese, D. Maxwell, R. S. Stucky, G. D. Krishnamurty, M. Petroff, P. Firouzi, A. Janicke, M. Chmelka, “Cooperative formation of inorganic-organic interfaces in the synthesis of silicate mesostructures,” *Sci.*, vol. 261, no. 5126, pp. 1299–1303, 1993, doi: 10.1126/science.261.5126.1299.

[24] D. Deng, Yonghui Yu, Ting Wan, Ying Shi, Yifeng Meng, Yan Gu, Dong Zhang, Lijuan Huang, Yan Liu, Chong Wu, Xiaojing Zhao, “Ordered mesoporous silicas and carbons with large accessible pores templated from amphiphilic diblock

copolymer poly(ethylene oxide)-b-polystyrene," *J. Am. Chem. Soc.*, vol. 129, no. 6, pp. 1690–1697, 2007, doi: 10.1021/ja067379v.

[25] M. S. Wong, D. M. Antonelli, and J. Y. Ying, "Synthesis and characterization of phosphated mesoporous zirconium oxide," *Nanostructured Mater.*, vol. 9, no. 1–8, pp. 165–168, 1997, doi: 10.1016/S0965-9773(97)00044-5.

[26] D. M. Antonelli, "Synthesis of macro-mesoporous niobium oxide molecular sieves by a ligand-assisted vesicle templating strategy," *Microporous Mesoporous Mater.*, vol. 33, no. 1–3, pp. 209–214, 1999, doi: 10.1016/S1387-1811(99)00139-0.

[27] C. J. Brinker, Y. Lu, A. Sellinger, and H. Fan, "Evaporation-induced self-assembly: Nanostructures made easy," *Adv. Mater.*, vol. 11, no. 7, pp. 579–585, 1999, doi: 10.1002/(SICI)1521-4095(199905)11:7<579::AID-ADMA579>3.0.CO;2-R.

[28] L. Mahoney and R. T. Koodali, "Versatility of Evaporation-Induced Self-Assembly (EISA) method for preparation of mesoporous TiO2 for energy and environmental applications," *Materials (Basel).*, vol. 7, no. 4, pp. 2697–2746, 2014, doi: 10.3390/ma7042697.

[29] N. A. Melosh, P. Davidson, and B. F. Chmelka, "Monolithic mesophase silica with large ordering domains," *J. Am. Chem. Soc.*, vol. 122, no. 5, pp. 823–829, 2000, doi: 10.1021/ja992801b.

[30] P. Melosh, N. A. Lipic, F. S. Bates, F. Wudl, G. D. Stucky, G. H. Fredrickson, and B. F. Chmelka, "Molecular and mesoscopic structures of transparent block copolymer-silica monoliths," *Macromolecules*, vol. 32, no. 13, pp. 4332–4342, 1999, doi: 10.1021/ma9817323.

[31] M. Mamak, N. Coombs, and G. Ozin, "Self-assembling solid oxide fuel cell materials: Mesoporous yttria-zirconia and metal-yttria-zirconia solid solutions," *J. Am. Chem. Soc.*, vol. 122, no. 37, pp. 8932–8939, 2000, doi: 10.1021/ja0013677.

[32] B. Sun, J. Horvat, H. S. Kim, W. S. Kim, J. Ahn, and G. Wang, "Synthesis of mesoporous α-Fe_2O_3 nanostructures for highly sensitive gas sensors and high capacity anode materials in lithium ion batteries," *J. Phys. Chem. C*, vol. 114, no. 44, pp. 18753–18761, 2010, doi: 10.1021/jp102286e.

[33] H. Yang and D. Zhao, "Synthesis of replica mesostructures by the nanocasting strategy," *J. Mater Chem*. pp. 1217–1231, 2005, doi: 10.1039/b414402c.

[34] A. H. Lu and F. Schüth, "Nanocasting: A versatile strategy for creating nanostructured porous materials," *Adv. Mater.*, vol. 18, no. 14, pp. 1793–1805, 2006, doi: 10.1002/adma.200600148.

[35] R. Ryoo, S. H. Joo, and S. Jun, "Synthesis of Highly Ordered Carbon Molecular Sieves via Template-Mediated Structural Transformation," *J. Phys. Chem. B*, vol. 103, no. 37, pp. 7743–7746, 1999, doi: 10.1021/jp991673a.

[36] A. H. Lu and F. Schüth, "Nanocasting pathways to create ordered mesoporous solids," *Comptes Rendus Chim.*, vol. 8, no. 3–4, pp. 609–620, 2005, doi: 10.1016/j.crci.2004.10.020.

[37] X. Deng, K. Chen, and H. Tüysüz, "Protocol for the Nanocasting Method: Preparation of Ordered Mesoporous Metal Oxides," *Chem. Mater.*, vol. 29, no. 1, pp. 40–52, 2017, doi: 10.1021/acs.chemmater.6b02645.

[38] W. C. Yoo and J. K. Lee, "Field-dependent growth patterns of metals electroplated in nanoporous alumina membranes," *Adv. Mater.*, vol. 16, no. 13, pp. 1097–1101, 2004, doi: 10.1002/adma.200306595.

[39] S. H. Joo, S. Jun, and R. Ryoo, "Synthesis of ordered mesoporous carbon molecular sieves CMK-1," *Microporous Mesoporous Mater.*, vol. 44–45, pp. 153–158, 2001, doi: 10.1016/S1387-1811(01)00179-2.

[40] Y. Ren, Z. Ma, and P. G. Bruce, "Ordered mesoporous metal oxides: Synthesis and

applications," *Chem. Soc. Rev.* pp. 4909–4927, 2012, doi: 10.1039/c2cs35086f.

[41] K. Che, Shunai Lund, T. Tatsumi, S. H. Iijima, Sumio Joo, and O. Ryoo, Ryong Terasaki, "Direct observation of 3D mesoporous structure by scanning electron microscopy (SEM): SBA-15 silica and CMK-5 carbon," *Angew. Chemie - Int. Ed.*, vol. 42, no. 19, pp. 2182–2185, 2003, doi: 10.1002/anie.200250726.

[42] W. C. Li, A. H. Lu, C. Weidenthaler, and F. Schüth, "Hard-templating pathway to create mesoporous magnesium oxide," *Chem. Mater.*, vol. 16, no. 26, pp. 5676–5681, 2004, doi: 10.1021/cm048759n.

[43] K. Zhu, B. Yue, W. Zhou, and H. He, "Preparation of three-dimensional chromium oxide porous single crystals templated by SBA-15," *Chem. Commun.*, vol. 8, no. 1, pp. 98–99, 2003, doi: 10.1039/b210065g.

[44] B. Yue and H. Tang, Huili Kong, Zuping Zhu, Kake Dickinson, Calum Zhou, Wuzong He, "Preparation and characterization of three-dimensional mesoporous crystals of tungsten oxide," *Chem. Phys. Lett.*, vol. 407, no. 1, pp. 83–86, 2005, doi: 10.1016/j.cplett.2005.03.066.

[45] F. Hao, Z. Zhang, and L. Yin, "Co_3O_4/carbon aerogel hybrids as anode materials for lithium-ion batteries with enhanced electrochemical properties," *ACS Appl. Mater. Interfaces*, vol. 5, no. 17, pp. 8337–8344, 2013, doi: 10.1021/am400952j.

[46] Y. X. Li, Gao Ren Feng, Zhan Ping Ou, Yan Nan Wu, Dingcai Fu, Ruowen Tong, "Mesoporous MnO2/Carbon aerogel composites as promising electrode materials for high-performance supercapacitors," *Lang.*, vol. 26, no. 4, pp. 2209–2213, 2010, doi: 10.1021/la903947c.

[47] H. Kim and J. Cho, "Hard templating synthesis of mesoporous and nanowire SnO2 lithium battery anode materials," *J. Mater. Chem.*, vol. 18, pp. 771–775, 2008, doi: 10.1039/b714904b.

[48] A. Rumplecker, F. Kleitz, E. L. Salabas, and F. Schüth, “Hard templating pathways for the synthesis of nanostructured porous Co_3O_4,” *Chem. Mater.*, vol. 19, no. 3, pp. 485–496, 2007, doi: 10.1021/cm0610635.

[49] K. E. Shopsowitz, A. Stahl, W. Y. Hamad, and M. J. MacLachlan, “Hard templating of nanocrystalline titanium dioxide with chiral nematic ordering,” *Angew. Chemie - Int. Ed.*, vol. 51, no. 28, pp. 6886–6890, 2012, doi: 10.1002/anie.201201113.

[50] Y. Yamauchi and K. Kuroda, “Rational design of mesoporous metals and related nanomaterials by a soft-template approach,” *Chem. - An Asian J.*, vol. 3, no. 4, pp. 664–676, 2008, doi: 10.1002/asia.200700350.

[51] F. C. Frank, “I. Liquid crystals. On the theory of liquid crystals,” *discuss. Far. Soc.*, no. I, pp. 19–28, 1958, doi: 10.1039/DF9582500019.

[52] Ingo Dierking, *Textures of Liquid Crystals*, 2004th ed. Wiley-VCH Verlag, 2003.

[53] S. Chandrasekhar and G. S. Ranganath, “Discotic liquid crystals,” *Reports Prog. Phys.*, vol. 53, no. 1, pp. 57–84, 1990, doi: 10.1088/0034-4885/53/1/002.

[54] Q. Liang, P. Liu, C. Liu, X. Jian, D. Hong, and Y. Li, “Synthesis and properties of lyotropic liquid crystalline copolyamides containing phthalazinone moiety and ether linkages,” *Poly.*, vol. 46, no. 16, pp. 6258–6265, 2005, doi: 10.1016/j.polymer.2005.05.059.

[55] C. Seguin, J. Eastoe, R. Clapperton, R. K. Heenan, and I. Grillo, “Alternative non-aqueous water-miscible solvents for surfactants,” *Coll. Surf. A Physicochem. Engi. Asp.*, vol. 282–283, pp. 134–142, 2006, doi: 10.1016/j.colsurfa.2005.11.028.

[56] N. R. B. Coleman and G. S. Attard, “Ordered mesoporous silicas prepared from both micellar solutions and liquid crystal phases,” *Micro. Meso. Mater.*, vol. 44–45, pp. 73–80, 2001, doi: 10.1016/S1387-1811(01)00170-6.

[57] G. Zhou, Y. Chen, J. Yang, and S. Yang, “From cylindrical-channel mesoporous

silica to vesicle-like silica with well-defined multilamella shells and large inter-shell mesopores," *J. Mater. Chem.*, vol. 17, no. 27, pp. 2839–2844, 2007, doi: 10.1039/b703055j.

[58] X. Wang, J. Feng, Y. Bai, Q. Zhang, and Y. Yin, "Synthesis, Properties, and Applications of Hollow Micro-/Nanostructures," *Chem. Rev.*, vol. 116, no. 18, pp. 10983–11060, 2016, doi: 10.1021/acs.chemrev.5b00731.

[59] B. Sun, G. Zhou, and H. Zhang, "Synthesis, functionalization, and applications of morphology-controllable silica-based nanostructures: A review," *Prog. Solid State Chem.*, vol. 44, no. 1, pp. 1–19, 2016, doi: 10.1016/j.progsolidstchem.2016.01.001.

[60] G. S. Attard, * Christine G. Goltner, * Judith M. Corker, S. Henke, and R. H. Temple, "Liquid-Crystal Templates for Nanostructured Metals," *Angew. Chemie - Int. Ed.*, vol. 109, 1997, doi: doi.org/10.1002/anie.199713151.

[61] G. S. Attard, P. N. Bartlett, N. R. B. Coleman, J. M. Elliott, J. R. Owen, and J. H. Wang, "Mesoporous platinum films from lyotropic liquid crystalline phases," *Sci.*, vol. 278, no. 5339, pp. 838–840, 1997, doi: 10.1126/science.278.5339.838.

[62] A. H. Whitehead, J. M. Elliott, J. R. Owen, and G. S. Attard, "Electrodeposition of mesoporous tin films," *Chem. Commun.*, pp. 331–332, 1999, doi: 10.1039/a808775j.

[63] P. V. Braun, P. Osenar, and S. I. Stupp, "Semiconducting superlattices templated by molecular assemblies," *Nature*, vol. 380, pp. 325–328, 1996, doi: 10.1038/380325a0.

[64] P. V. Braun, P. Osenar, V. Tohver, S. B. Kennedy, and S. I. Stupp, "Nanostructure templating in inorganic solids with organic lyotropic liquid crystals," *J. Am. Chem. Soc.*, vol. 121, no. 32, pp. 7302–7309, 1999, doi: 10.1021/ja9833725.

[65] Ö. Çelik and O. Dag, "A New Lyotropic Liquid Crystalline System: Oligo(ethylene

oxide) Surfactants with [M(H_2 O)$_2$n]X_2m Transition Metal Complexes," *Angew. Chem. Int. Ed.*, vol. 40, no. 20, pp. 3799–3803, 2001.

[66] A. Faik Demirörs, B. E. Eser, and Ö. Dag, "Liquid crystalline mesophases of pluronics (L64, P65, and P123) and transition metal nitrate salts ([M(H_2O)$_6$](NO $_3$)$_2$)," *Langmuir*, vol. 21, no. 9, pp. 4156–4162, 2005, doi: 10.1021/la047136l.

[67] Ö. Dag, S. Alayoğlu, and I. Uysal, "Effects of ions on the liquid crystalline mesophase of transition-metal salt: Surfactant (C_nEO_m)," *J. Phys. Chem. B*, vol. 108, no. 24, pp. 8439–8446, 2004, doi: 10.1021/jp049716x.

[68] Ö. Dag, O. Samarskaya, C. Tura, A. Günay, and Ö. Çelik, "Spectroscopic Investigation of Nitrate−Metal and Metal−Surfactant Interactions in the Solid $AgNO_3C_{12}EO_{10}$ and Liquid-Crystalline [M(H_2O)n](NO_3)$_2$/$C_{12}EO_{10}$ Systems," *Langmuir*, vol. 19, no. 9, pp. 3671–3676, 2003, doi: 10.1021/la020740g.

[69] Y. Türker and Ö. Dag, "Synthesis of mesostructured metal sulfide films using [M(H_2O)n](NO_3)$_2$:P85 (M= Cd(II) and Zn(II)) liquid crystalline mesophases," *J. Mater. Chem.*, vol. 18, no. 29, pp. 3467–3473, 2008, doi: 10.1039/b804344b.

[70] Ö. mer D. Cemal Albayrak, Aslı M. Soylu and Laboratory, "Lyotropic Liquid-Crystalline Mesophases of [Zn(H_2O)$_6$](NO_3)$_2$)-$C_{12}EO_{10}$-CTAB-H_2O and [Zn(H_2O)$_6$](NO_3)$_2$-$C_{12}EO_{10}$-SDS-H," *Langmuir*, vol. 110, no. 18, pp. 9039–9047, 2004.

[71] C. Albayrak, A. M. Soylu, and Ö. Dag, "The role of charged surfactants in the thermal and structural properties of lyotropic liquid crystalline mesophases of [Zn(H_2O)$_6$](NO_3)$_2$-C_nEO_m-H_2O," *J. Colloid Interface Sci.*, vol. 341, no. 1, pp. 109–116, 2010, doi: 10.1016/j.jcis.2009.09.038.

[72] C. Karakaya, Y. Türker, C. Albayrak, and Ö. Dag, "Assembly of molten transition metal salt-surfactant in a confined space for the synthesis of mesoporous metal oxide-rich metal oxide-silica thin films," *Chem. Mater.*, vol. 23, no. 12, pp. 3062–

3071, 2011, doi: 10.1021/cm200932k.

[73] C. Albayrak, N. Özkan, and Ö. Dag, “Origin of lyotropic liquid crystalline mesophase formation and liquid crystalline to mesostructured solid transformation in the metal nitrate salt-surfactant systems,” *Lang.*, vol. 27, no. 3, pp. 870–873, 2011, doi: 10.1021/la1035932.

[74] C. Karakaya, Y. Türker, and Ö. Dag, “Molten-salt-assisted self-assembly (MASA)-synthesis of mesoporous metal titanate-titania, metal sulfide-titania, and metal selenide-titania thin films,” *Adv. Funct. Mater.*, vol. 23, no. 32, pp. 4002–4010, 2013, doi: 10.1002/adfm.201202716.

[75] C. Karakaya, Y. Türker, and Ö. Dag, “Molten-Salt-Assisted Self-Assembly (MASA)-Synthesis of Mesoporous Metal Titanate-Titania, Metal Sulfi de-Titania, and Metal Selenide-Titania Thin Films,” *Adv. Funct. Mater.*, 2013, doi: 10.1002/adfm.201202716.

[76] Ö. Dağ, C.Avci , A.Aydin, Z.Tuna, Z.Yavuz, Y.Yamauchi, N.Suzuki, “Molten salt assisted self assembly (MASA): Synthesis of mesoporous metal titanate ($CoTiO_3$, $MnTiO_3$, and $Li_4Ti_5O_{12}$) thin films and monoliths,” *Chem. Mater.*, vol. 26, no. 20, pp. 6050–6057, 2014, doi: 10.1021/cm503020y.

[77] G. Saat, F. M. Balci, E. P. Alsaç, F. Karadas, and Ö. Dag, “Molten Salt Assisted Self-Assembly: Synthesis of Mesoporous $LiCoO_2$ and $LiMn_2O_4$ Thin Films and Investigation of Electrocatalytic Water Oxidation Performance of Lithium Cobaltate,” *Small*, vol. 14, no. 1, pp. 1701913-1701913–11, 2018, doi: 10.1002/smll.201701913.

[78] A. Amirzhanova, Irmak Karakaya, Can Berk Uzundal, Gözde Karaoğlu, Ömer Dag, Burak Ülgüt, Ferdi Karadas, “Synthesis and water oxidation electrocatalytic and electrochromic behaviours of mesoporous nickel oxide thin film electrodes,” *J. Mater. Chem. A*, vol. 7, no. 38, pp. 22012–22020, 2019, doi: 10.1039/c9ta07693j.

[79] F. Mert Balci, Irmak Karakaya, Elif Pınar Alsaç, Muammer Yusuf Yaman, Gülbahar Saat, Ferdi Karadas, Burak Ülgüt, Ömer Dag, "Synthesis of mesoporous $LiMn_2O_4$ and $LiMn_2$-xCo_xO_4 thin films using the MASA approach as efficient water oxidation electrocatalysts," *J. Mater. Chem. A*, vol. 6, no. 28, pp. 13925–13933, 2018, doi: 10.1039/c8ta04138e.

[80] A. Amirzhanova, N. Akmanşen, I. Karakaya, and Ö. Dag, "Mesoporous $MnCo_2O_4$, $NiCo_2O_4$, and $ZnCo_2O_4$Thin-Film Electrodes as Electrocatalysts for the Oxygen Evolution Reaction in Alkaline Solutions," *ACS Appl. Energy Mater.*, vol. 4, no. 3, pp. 2769–2785, 2021, doi: 10.1021/acsaem.1c00064.

[81] Q. Zhang, E. Uchaker, S. L. Candelaria, and G. Cao, "Nanomaterials for energy conversion and storage," *Chem. Soc. Rev.*, vol. 42, pp. 3127–3171, 2013, doi: 10.1039/c3cs00009e.

[82] D. Ganguly, D. Pahari, N. S. Das, and K. K. Howli, P. Das, B. Banerjee, D. Chattopadhyay, "All-amorphous CNT-MnO_2 nanoflaky hybrid for improved supercapacitor applications," *J. Electroanal. Chem.*, vol. 778, pp. 12–22, 2016, doi: 10.1016/j.jelechem.2016.08.006.

[83] Y. Wang, J. Zhu, X. Yang, L. Lu, and X. Wang, "Preparation of NiO nanoparticles and their catalytic activity in the thermal decomposition of ammonium perchlorate," *Thermochim. Acta*, vol. 437, no. 1–2, pp. 106–109, 2005, doi: 10.1016/j.tca.2005.06.027.

[84] F. F. Ferreira and E. Avendaño, "Reversible electronic charge transfer between Au nanoparticles and electrochromic NiO matrices upon electrochemical cycling," *J. Phys. Chem. C*, vol. 111, no. 44, pp. 16608–16612, 2007, doi: 10.1021/jp0758162.

[85] M. Jlassi, I. Sta, M. Hajji, and H. Ezzaouia, "Synthesis and characterization of nickel oxide thin films deposited on glass substrates using spray pyrolysis," *Appl. Surf. Sci.*, vol. 308, pp. 199–205, 2014, doi: 10.1016/j.apsusc.2014.04.134.

[86] P. Jeevanandam and V. R. R. Pulimi, “Synthesis of nanocrystalline NiO by sol-gel and homogeneous precipitation methods,” *Indian J. Chem. - Sect. A Inorganic, Phys. Theor. Anal. Chem.*, vol. 51A, pp. 586–590, 2012.

[87] A. Rahdar, M. Aliahmad, and Y. Azizi, “Synthesis of Cu Doped NiO Nanoparticles by Chemical Method,” *J. Nanostructures*, vol. 4, pp. 145–152, 2014, doi: 10.7508/jns.2014.02.003.

[88] C. Li and S. Liu, “Preparation and characterization of $Ni(OH)_2$ and nio mesoporous nanosheets,” *J. Nanomater.*, vol. 2012, pp. 1–6, 2012, doi: 10.1155/2012/648012.

[89] L. Wang, Y. Hao, Y. Zhao, Q. Lai, and X. Xu, “Hydrothermal synthesis and electrochemical performance of NiO microspheres with different nanoscale building blocks,” *J. Solid State Chem.*, vol. 183, no. 11, pp. 2576–2581, 2010, doi: 10.1016/j.jssc.2010.09.006.

[90] K. Byrappa and T. Adschiri, “Hydrothermal technology for nanotechnology,” *Progress in Crystal Growth and Characterization of Materials*. 2007, doi: 10.1016/j.pcrysgrow.2007.04.001.

[91] S. K. Meher, P. Justin, and G. R. Rao, “Microwave-mediated synthesis for improved morphology and pseudocapacitance performance of nickel oxide,” *ACS Appl. Mater. Interfaces*, vol. 3, no. 6, pp. 2063–2073, 2011, doi: 10.1021/am200294k.

[92] A. Venter and J. R. Botha, “Optical and electrical properties of NiO for possible dielectric applicatons,” *S. Afr. J. Sci.*, vol. 107, no. 1–2, pp. 1–6, 2011, doi: 10.4102/sajs.v107i1/2.268.

[93] H. Yang, Q. Tao, X. Zhang, A. Tang, and J. Ouyang, “Solid-state synthesis and electrochemical property of SnO_2/NiO nanomaterials,” *J. Alloys Compd.*, vol. 459, no. 1–2, pp. 98–102, 2008, doi: 10.1016/j.jallcom.2007.04.258.

[94] R. Eder, “Electronic structure of NiO: Antiferromagnetic transition and photoelectron spectra in the ordered phase,” *Phys. Rev. B - Condens. Matter Mater. Phys.*, vol. 91, no. 24, pp. 1–20, 2015, doi: 10.1103/PhysRevB.91.245146.

[95] S. A. Mahmoud, A. Shereen, and M. A. Tarawnh, “Structural and Optical Dispersion Characterisation of Sprayed Nickel Oxide Thin Films,” *J. Mod. Phys.*, vol. 2, pp. 1178–1186, 2011, doi: 10.4236/jmp.2011.210147.

[96] J. Wang, B. Zou, and M. A. El-Sayed, “Comparison between the polarized fourier-transform infrared spectra of aged porous silicon and amorphous silicon dioxide films on Si (100) surface,” *J. Mol. Struct.*, vol. 508, no. 1–3, pp. 87–96, 1999, doi: 10.1016/S0022-2860(99)00003-4.

[97] S. Rovani, J. J. Santos, P. Corio, and D. A. Fungaro, “An alternative and simple method for the preparation of bare silica nanoparticles using sugarcane waste ash, an abundant and despised residue in the Brazilian industry,” *J. Braz. Chem. Soc.*, vol. 30, no. 7, pp. 1524–1533, 2019, doi: 10.21577/0103-5053.20190049.

[98] K. Kinashi, Y. Kambe, M. Misaki, Y. Koshiba, K. Ishida, and Y. Ueda, “Synthesis, characterization, photo-induced alignment, and surface orientation of poly(9,9-dioctylfluorene-alt-azobenzene)s,” *J. Polym. Sci. Part A Polym. Chem.*, vol. 50, no. 24, pp. 5107–5114, 2012, doi: 10.1002/pola.26338.

[99] L. Greenspan, “Humidity Fixed Points of Binary Saturated Aqueous Solutions.,” *J. Res. Natl .Bur. Stand. Sect. A. Phys. Chem.*, vol. 81 A, no. 1, pp. 89–96, 1977, doi: 10.6028/jres.081A.011.